UNIVERSITY OF CALIFORNIA SAN DIEGO

Development of Multifunctional Nanocomposite Sensing Systems for Structural and Human Health Monitoring

A dissertation submitted in partial satisfaction of the

requirements for the degree of Doctor of Philosophy

in

Structural Engineering

by

Long Wang

Committee in charge:

Professor Kenneth J. Loh, Chair
Professor Francesco Lanza di Scalea
Professor Darren J. Lipomi
Professor Yu Qiao
Professor Michael D. Todd

2019

The Dissertation of Long Wang is approved, and it is acceptable in quality and form for publication on microfilm and electronically:

_____

_____

_____

_____

_____

Chair

University of California San Diego

2019

DEDICATION

To Mom and Dad

TABLE OF CONTENTS

LIST OF ABBREVIATIONS AND ACRONYMS

1D	One-Dimensional
2D	Two-Dimensional
3D	Three-Dimensional
ACI	American Concrete Institute
AE	Acoustic Emission
ASCE	American Society of Civil Engineers
BR	Blur Radius
CEM	Complete Electrode Model
CM	Condition Monitoring
CNT	Carbon Nanotube
CS	Compressed Sensing
CVD	Chemical Vapor Deposition
CWT	Continuous Wavelet Transform
DAQ	Data Acquisition
DC	Direct Current
DI	Deionized
DMM	Digital Multi-Meter
EC	Ethyl Cellulose
ECG	Electrocardiogram
EIT	Electrical Impedance Tomography
FE	Finite Element

GF	Gage Factor
GO	Graphene Oxide
GNS	Graphene Nanosheets
GSR	Galvanic Skin Response
IST	Iterative Shrinkage Thresholding
LbL	Layer-by-Layer
LED	Light-Emitting Diodes
LIS	Locked in Syndrome
L-J	Leonard-Jones
LPE	Liquid-Phase Exfoliation
LPEGNS	Liquid-Phase Exfoliation Graphene Nanosheet
MCS	Minimally Conscious State
MWCNT	Multi-Walled Carbon Nanotube
MEMS	Micro-Electro-Mechanical System
NDE	Nondestructive Evaluation
NW	Nanowire
PGS	Printed Graphene Sensor
PPG	Photoplethysmograph
RCSW	Reinforced Concrete Shear Wall
RGO	Reduced Graphene Oxide
RMS	Root Mean Square
SEM	Scanning Electron Microscopy
SHM	Structural Health Monitoring

SI	Stiffness Index
SPC	Statistical Process Control
TEM	Transmission Electron Microscopy
TwIST	Two-step Iterative Shrinkage Thresholding
WALPE	Water-Assisted Liquid-Phase Exfoliation
WSN	Wireless Sensor Network

GLOSSARY

CO-890	Polyoxyethylene (40) nonylphenyl ether
H_2O	Water
H_2O_2	Hydrogen Peroxide
H_2SO_4	Sulfuric Acid
$KMnO_4$	Potassium Permanganate
MnO_2	Manganese(IV) Oxide
NMP	N-methyl-2-pyrrolindinone
PDMS	Poly(dimethyl siloxane)
PET	Poly(ethylene terephthalate)
PSS	Poly(sodium 4-styrenesulfonate)
ZnO	Zinc Oxide

LIST OF FIGURES

ACKNOWLEDGEMENTS

At this important moment of my life, I hope to express my sincere gratitude to many people for their support and profound impacts on my life and professional career. First, I owe my foremost appreciation to my parents (Bingyun Luo and Yongsheng Wang) for their continuous love and support that empowered me to overcome all the obstacles to date. Their diligent work ethic has inspired and motivated me since I was a child. They have laid the very foundation for my current self as well as my future life. I feel truly fortunate that I have them as my family.

I would also like to sincerely thank my Ph.D. advisor and mentor, Professor Ken Loh, for his guidance and support. I was highly inspired by his intellectual research ideas and motivated by his passion for research and teaching. He has dedicated countless hours and effort on assisting me to develop my professional skillset, which have fundamentally shaped my aspirations for future career as a researcher.

In addition, I had the privilege to work with many renowned researchers, brilliant students, and supportive collaborators. First, I appreciate the help from all my Ph.D. committee members, including Professor Francesco Lanza di Scalea, Professor Darren Lipomi, Professor Yu Qiao, and Professor Michael Todd. Their constructive comments and suggestions have inspired me to improve my research from innovative perspectives. Furthermore, I hope to express my gratitude to Professor Wei-Hung Chiang and Dr. Kausik Manna from the National Taiwan University of Science and Technology for synthesizing the graphene nanosheets that I used for fabricating the graphene-based nanocomposites. I would also like to thank Professor Tara Hutchinson and Gloria Faraone for the productive collaborations on spatial sensing tests on the reinforced concrete shear

wall specimen that they designed and constructed. Furthermore, my industrial collaborators, LIM Innovations and Mr. Tristan Wyatt, have offered me a unique opportunity to work closely with prostheses and amputated patients for developing the smart socket prostheses. I have also worked with Gianmarco Vella and Ramin Mousacohen on topological design of nanocomposites and micro-patterning graphene sensors, respectively. Their contributions have significantly supported the projects.

Last but not least, I appreciate the support from the National Science Foundation (NSF) under grant numbers CMMI CAREER-1253564 and CMMI-120052, Office of Naval Research (ONR) under grant numbers N00014-17-1-2668 and N00018-1-2483 (program manager: Dr. Liming Salvino). Additional support was provided by the Jacobs School of Engineering, University of California San Diego.

Chapter 2, in part, is a reprint of the material as it appears in Spray-coated Carbon Nanotube-Latex Strain Sensors, L. Wang and K. J. Loh, 2015; Micro-Patterned Graphene Sensing Skins for Human Physiological Monitoring, L. Wang, K. J. Loh, W.-H. Chiang, and K. Manna, 2018; and Printed Strain Sensors Using Graphene Nanosheets Prepared by Water-Assisted Liquid Phase Exfoliation, K. Manna, L. Wang, K. J. Loh, and W.-H. Chiang, 2019. The dissertation author was the primary investigator and author of these papers.

Chapter 3, in part, is a reprint of the material as it appears in Topological Design of Carbon Nanotube-based Nanocomposites for Strain Sensing, L. Wang, G. Vella, and K. J. Loh, 2019; Topological Design and Characterization of Piezoresistive Nanocomposites, L. Wang, G. Vella, W.-H. Chiang, and K. J. Loh, 2019; and in part is currently being prepared for submission for publication of the material, Topological Design-Encoded Strain Sensing Performance of Graphene

Nanocomposites, L. Wang and K. J. Loh, 2019. The dissertation author was the primary investigator and author of these papers.

Chapter 4, in part, is a reprint of the material as it appears in Micro-Patterned Graphene Sensing Skins for Human Physiological Monitoring, L. Wang, K. J. Loh, W.-H. Chiang, and K. Manna, 2018; and Wearable Carbon Nanotube-Based Fabric Sensors for Monitoring Human Physiological Performance, L. Wang and K. J. Loh, 2017. The dissertation author was the primary investigator and author of these papers.

Chapter 6, in part, is a reprint of the material as it appears in Nanocomposite Fabric Sensors for Socket Prostheses, L. Wang and K. J. Loh, 2018. The dissertation author was the primary investigator and author of these papers.

VITA

2019	Doctor of Philosophy, Structural Engineering, University of California San Diego
2016	Master of Science, Mechanical & Aerospace Engineering, University of California Davis
2015	Master of Science, Civil Engineering, University of California Davis
2014	Bachelor of Science, Port, Waterway, and Coastal Engineering, Dalian University of Technology

ABSTRACT OF THE DISSERTATION

Development of Multifunctional Nanocomposite Sensing Systems for Structural and Human Health Monitoring

by

Long Wang

Doctor of Philosophy in Structural Engineering

University of California San Diego, 2019

Professor Kenneth J. Loh, Chair

Our built environment is replete with engineered structural systems (*e.g.*, civil infrastructure, automobiles, marine and aerospace structures, among others), and the socioeconomic well-being of our society is strongly dependent on their safe and reliable operations. However, structural safety degrades with age, and they can sustain damage due to various natural hazards and extreme events (*e.g.*, earthquakes, hurricanes, and landslides, to name a few). In addition, because of increasingly closer human and engineered structure interactions, human error and/or fatigue can also threaten the safe operations of various structural systems. Therefore, structural health monitoring (SHM) techniques have attracted extensive attention,

mainly for their potential of timely detecting structural damage while minimizing service downtime and economic loss. A similar monitoring paradigm can also be employed to assess human operators' performance for avoiding human-induced structural failures and accidents.

The SHM paradigm typically relies on sensing systems to provide rich datasets regarding structural performance. While various off-the-shelf sensing transducers have been employed, the complex damage modes, drastically different materials, intricate geometries, and diverse operational environments make it challenging for conventional sensors to effectively quantify structural health and human performance. Multifunctional materials, on the other hand, can be designed using a bottom-up approach for realizing novel sensing mechanisms that could be better suited for extracting relevant damage features while tailoring their designs for specific engineering applications.

The primary objective of this dissertation was to develop, characterize, and implement multifunctional material-based sensing systems for both structural health and human performance monitoring. This work aimed to leverage the extraordinary mechanical and electrical properties of nanostructured materials (including carbon nanotubes and graphene) to achieve robust and high-performance sensing systems. Although previous endeavors have been dedicated to developing nanomaterial-based sensing systems, their practical applications could be hindered by complex material fabrication processes and poor scalability. Therefore, this study employed simple, scalable, and low-cost manufacturing techniques to fabricate multifunctional nanocomposites of optimized mechanical properties and strain sensing characteristics. In addition, a topological design methodology was proposed to strategically engineer the strain sensing properties of nanocomposite thin films for different target applications.

To overcome the discrete sensing limitations of current transducers, this work coupled the nanocomposite sensors with electrical impedance tomography and compressed sensing algorithms for achieving spatial sensing capability. Extensive laboratory tests were performed to characterize their spatial sensing performance. In the last phase of this work, the spatial sensing systems were implemented to monitoring seismic loading-induced structural damage on a full-scale reinforced concrete shear wall. At the same time, fabric-based sensors were fabricated and integrated with socket prosthesis surrogates to demonstrate their applicability for human monitoring applications (*e.g.*, assistive rehabilitation and pressure ulcers prevention). Overall, this dissertation advanced multifunctional material-based sensing systems for monitoring engineered structures and human health.

Chapter 1. Introduction

1.1. Grand Challenges for Built Environment Resilience

The current built environment depends heavily on the safe and reliable operations of ubiquitous complex engineered structural systems. These structural systems broadly include civil infrastructure (*e.g.*, buildings, bridges, pipelines, railways, dams, and wind turbines), automobiles, marine vessels (*e.g.*, ships), and aerospace structures (*e.g.*, airplanes), among many others. Most of these structures are designed to bear loads and operate safely under anticipated loading scenarios over their expected lifespans [1-4]. However, the initially designed structural performance can often be compromised by structural damage and deterioration, hence threatening the resilience of the built environment [1, 3, 5]. For instance, structural aging (*i.e.*, structural performance degradation) is inevitable when these systems have been in service over long periods of time. Specifically, in the context of civil infrastructure systems, highly-developed urban regions, such as those in the United States (U.S.) and Europe, contain an excessively large inventory of aged infrastructure that operate close to the end of, if not already past, their designed service life [4-6]. The degraded structural performance could potentially lead to structural failure and cause grave casualties as well as enormous adverse socio-economic impacts.

As an example, in the U.S., gas leaks from aging pipelines have frequently led to destructive explosions. Since 2004, such accidents have killed 135 people, injured 600 people, and costed ~ $2 billion in damages [7, 8]. In addition, the nearly 50-year-old Oroville Dam (California, U.S.) suffered damage in its main and emergency spillways in February 2017, causing the evacuation of more than 180,000 people who were living downstream, which pushed dam safety to the epicenter of national concerns [9, 10]. Similarly, public concerns about infrastructure aging in Europe were brought front and center in August 2018 when the over 50-year-old Morandi Bridge (Genoa, Italy) collapsed, possibly due to corrosion of its cables, and caused 43 deaths and left over 600 homeless [11, 12].

Besides long-term structural aging, extreme load events (*i.e.*, load combinations that significantly exceed designed structural load capacity) are also major causes of structural damage. Many extreme load events for civil infrastructure are associated with natural disasters. For example, the Northridge earthquake (Los Angeles, U.S.) in January 1994 killed 57 people and injured 8,700, causing an estimated $13 to $44 billion in damage [13]. The earthquake even damaged hospitals and school buildings (which are built according to some of the most strongest building code requirements). This unfortunate natural catastrophe significantly stimulated development of earthquake-resilient structures, especially for critical infrastructure, and launched the nationwide effort to advance performance-based earthquake engineering design principles. While damage due to earthquakes and other natural disasters make headlines, the U.S. also suffers from increasingly costly weather- and climate-related damage to its infrastructure systems, and their performance and safety become further jeopardized in light of these extreme events [5, 14, 15].

Furthermore, due to the rapid global urbanization, the United Nations has predicted that about 70% of the world's population will be living in urban areas by 2050 [16]. Accompanied with the ever-increasing population in the built environment, the interactions between humans and engineered structural systems have never been closer and more sensitive. In particular, the safety and reliability of human-operated land, air, and marine vessels and structural systems can be significantly compromised by human operator behavior. As a matter of fact, human error or fatigue was shown to be the predominant threat to the safe operations of various structural systems [17-21]. For instance, one investigation from Boeing reported that 80% of flight accidents were caused by human error, which was equivalent to the share of machine-related failures in 1903 [22]. More recently, the Virgin Galactic SpaceShipTwo spacecraft crashed in California due to the co-pilot's error during flying (October 31, 2014) [23]. As for land transportation, it was reported that 90% of car accidents were human error-related [24], and the National Highway Traffic Safety Administration argued that numerous road catastrophes were caused by drivers' medical conditions during driving [25].

It is clear from the aforementioned examples that the safety of structural systems is vulnerable to aging, extreme events, and multi-hazards (including both natural and manmade disasters). In addition, failures of critical structures can significantly jeopardize public safety and the socio-economic well-being of society in general. Therefore, from a structural damage detection perspective, it is imperative to assess and even predict structural performance and damage states so as to prevent similar types of accidents from occurring in the future (or at least minimizing their negative impacts) [2, 4, 26]. In the context of human-induced structural failures, similar performance assessment strategies could also be implemented to evaluate the human operators' conditions for minimizing or preventing structural damage due to human misconducts [18, 19, 21].

Therefore, the grand challenge is how to economically and efficiently enhance the resilience of our built environment while improving quality of life.

1.2. Current State-of-the-Art of Monitoring Technologies

1.2.1. Structural health monitoring

Since structural damage and deterioration can compromise the load capacity of structural systems and can leave structures to be more vulnerable to failures, early detection of structural damage is direly needed for ensuring structural safety and minimizing their life cycle costs [2, 4, 26-28]. Conventional wisdom dictates that visual inspection should be used to identify damage on structural surfaces or inspectable locations. The recent and rapid advancements in robotic systems and computer vision technologies have fundamentally transformed traditional visual inspection approach to that of an automatic process, whereby unmanned robotic systems could navigate and inspect areas where they were once too difficult to access by technicians. The next-generation autonomous visual inspection techniques are promising to overcome some of the major limitations of manual inspection, including inspection cost and subjectivity of human inspectors [2, 27, 28]. However, the fact that not all types of structural damage are visible on the surface (*i.e.*, because they occur subsurface) and that many critical structural components are inaccessible, comprehensive safety evaluation of structures remains challenging when using visual inspection and robotic-assisted inspection methods. Furthermore, visual inspection is highly subjective, and inspection outcomes can differ tremendously depending on the training and experiences of different technicians.

Motivated by the limitations of visual inspections, more quantitative damage detection technologies have been developed in several closely related disciplines, including nondestructive

evaluation (NDE), structural health monitoring (SHM), condition monitoring (CM), and statistical process control (SPC), among others [4, 26, 28]. NDE mainly focuses on offline characterization of the location and severity of damage in the system. Some common NDE techniques include X-ray penetration, thermography, acoustic emissions, and Lamb wave propagation (or active sensing), among many others [30-32]. Typically, these NDE techniques need to be operated manually by a trained technician and when the structure is taken out of service. In contrast to NDE, the SHM strategy is that instrumented sensing systems deployed on structures will monitor and record system response to different loads without having to take the structure offline. By extracting or inferring features that suggest damage or degradation has taken place, an automated signal can be generated to alert the relevant stakeholders. Thus, SHM is promising and broadly applicable to a vast category of civil infrastructure, machinery, aerospace, and marine structural systems. Similar to SHM, the purpose of CM is to detect damage in rotating machinery [26, 29].

Among these strategies, SHM has recently received extensive attention due to its potential for minimizing structural service downtime and economic loss [4, 26, 27]. In general, SHM intends to acquire relevant data that inform structural performance, based on which to provide actionable information and to inform asset management decisions [2, 26, 28]. In other words, comprehensive SHM systems would include both damage detection and damage prognosis. As the first stage of SHM, effective sensing technologies are needed for acquiring rich datasets that contain information about structural damage and their properties. Their robustness, accuracy, and cost directly define the capability and practical applicability of these SHM systems for the corresponding target structures [4, 26]. Given the importance of sensing systems in the entire SHM process, this dissertation mainly focuses on developing innovative sensing systems for advancing the SHM paradigm.

In fact, various sensing systems have been designed and implemented for SHM applications. For example, foil strain gages possess advantages such as being low-cost, lightweight, are easy to install, and have high strain sensitivity (~ 2 at room temperature). However, their application is limited to individual locations, and a dense network of strain gages is often needed for monitoring large-scale structures [33]. The same is true for accelerometers, which has been deployed on countless structures for monitoring their dynamic characteristics when these structures are subjected to ambient and forced excitations. On the other hand, distributed fiber sensing techniques are capable of measuring strains over the entire length of continuous optical fibers [34-38]. Fiber optic sensors offer advantages by being lightweight, immune to electromagnetic interference and corrosion, and can achieve distributed sensing, among others [35, 38, 39]. While the fiber optic sensing systems have been used in practical SHM implementations, since these systems offer optical fiber cables and optical analyzers, it can be expensive and complicated to install these tethered systems on large-scale structures [34, 35].

As an alternative, wireless sensor networks (WSNs) can realize relatively simpler and cheaper implementation by eliminating most of the cables required for the aforementioned tethered systems [40-44]. A typical WSN node includes microcontrollers, sensors, and radios, whose power consumption management can be challenging for long-term monitoring tasks (especially since individual wireless sensing nodes are powered by portable power supplies such as batteries) [34, 41, 43]. In addition, current WSNs have been combined with micro-electro-mechanical system (MEMS) to not only reduce the cost of the overall cost of the sensing system, but they also enhance sensing data quality and communication capabilities. This is because MEMS integrates micro-scale functional electronic components in a single silicone chip, which can significantly miniaturize sensor form factor, reduce power consumption, and improve sensing performance [34,

44-46]. However, these wireless sensors mostly rely on conventional materials (*e.g.*, metals and silicone), and they are discrete devices that can only measure the structural response at limited locations.

1.2.2. Human performance monitoring

On the other hand, as previously mentioned, human operators' performance can also directly affect structural performance and even lead to catastrophic structural failures. In order to reduce the number of human-induced structural incidents, one should ensure that the operator maintains their optimal physiological and psychological conditions. In that regard, wearable sensing systems offer great promise for measuring a human operator's vital signals (*e.g.*, respiration rate and body temperature), which can be used for evaluating their state-of-mind and physical wear.

In general, wearable sensors are transducers that can be externally applied onto individuals and provide signals related to human physiological or biophysical parameters [47]. They have received extensive attention mainly due to their potential for improving the well-being of diverse groups. For example, people working in dangerous or harsh environments (*e.g.*, warfighters, firefighters, law enforcement personnel, and astronauts) are constantly faced with a variety of potentially life-threatening situations. Wearable sensors can enable real-time monitoring of their physiological performance for ensuring their optimal performance and safety. In addition, in the context of senior care, wearable sensors have enabled health monitoring systems of senior citizens and patients so that they can receive diagnosis or treatment without physically visiting a hospital. Instead, they can receive care in a more hospitable environment, such as their own home, which is the goal of the telemedicine movement [47, 48]. When it comes

to enhancing athletes' performance, wearable sensors offer tremendous opportunities for better quantifying and analyzing their motions, which, at the same time, can help protect them from injuries [49]. Given the broad impacts of wearable sensors, it is imperative to further develop higher performance transducers that can monitor different aspects of human performance, such as physical motions and human vitals, among others.

A popular approach of designing wearable sensors is to integrate commercial-off-the-shelf electronic devices, including strain gages, accelerometers, and pulse-oximeters, among others, to form a miniature hardware package. Some examples of early-generation wearable sensors were designed as rings, glasses, bracelets, and watches. For instance, a ring sensor equipped with light-emitting diodes (LED) and photo-detectors was developed by Rhee *et al.* [50] for wirelessly monitoring patients' blood oxygen saturation. Anliker *et al.* [51] designed a portable telemedical monitoring and alerting system that could be worn on the wrist of patients whom suffer from cardiac/respiratory diseases. The sensing system can monitor multiple vital signals, including heart rate, blood pressure, electrocardiogram (ECG), and skin temperature. Further developments sought to incorporate these sensors in clothes and garments for minimizing the inconvenience of having to wear additional peripheral devices on one's body. Gopalsamy *et al.* [52] presented a smart shirt integrated with a "wearable motherboard" that can be easily worn by soldiers for monitoring multiple vital parameters. Pandian *et al.* [49] designed a smart vest, which was equipped with temperature sensors, electrodes for ECG, photoplethysmograph (PPG), and galvanic skin response (GSR) measurements. Lee *et al.* [48] used a smart shirt coupled with a wireless sensor network to accurately extract ECG signals from a test subject's physical movements. One of the considerable advantages of these conventional wearable sensing systems is that a single sensor can be used to measure multiple physiological

parameters with favorable accuracy. Besides, many of these sensors are relatively low-cost. However, these devices usually include bulky and rigid components. Their form factors and intrinsic rigidity and can be incompatible with complex and high-strains typical of human motions, which not only compromises sensing accuracy but can also cause user discomfort.

1.3. Emerging Materials-Enabled Sensing System Design

1.3.1. Applications in monitoring structural performance

To overcome the aforementioned limitations of discrete electronic sensors, nanostructured material-based sensors have undergone rapid development over the last few decades. As an emerging sensing technique, so far, nanomaterial-based sensors are still mainly employed in controlled scenarios, but have already exhibited remarkable potentials to transform the current sensing devices [53-57]. Some target application examples include electrochemical biosensors [58-60], moisture sensors [61], optical sensors [62], temperature sensors [63], and heavy-metal detectors [64], and many of which are based on nanomaterials in conjunction with conductive polymers. The growing interests in nanostructured materials stem from the fact that these materials possess superior and unique thermal, electrical, mechanical, optoelectronic, and chemical properties as compared to their bulk counterparts [65]. In addition, inherent to nanomaterials is their large surface area-to-volume ratio, and these surfaces can be tailored and functionalized with different molecular species so as to tune their material properties and to enhance their macro-scale sensing performance [66-68].

In the context of SHM applications, nanomaterial-based sensors offer tremendous advantages over conventional mechanical- or electrical-based transducers that are inherently discrete devices and can be bulky in size. Nanomaterial-based sensors can be applied onto entire,

large, and complex structural surfaces for continuous spatial structural sensing, as opposed to being only instrumented at certain discrete locations. For example, Loh *et al.* [69] fabricated freestanding piezoresistive zinc oxide (ZnO) nanocomposite thin films by mold-casting, which could be directly adhered onto cantilever beams for monitoring their strain changes under dynamic excitations. Gullapalli *et al.* [70] incorporated ZnO with paper (*i.e.*, cellulose fibers) via a dipping and drying process and obtained flexible paper sensors that could be readily installed onto structural surfaces. Being highly flexible and lightweight, those nanocomposite thin film sensors provide numerous opportunities for monitoring strains on curved structural surfaces without affecting structural performance, which would otherwise be challenging for conventional strain sensors.

1.3.2. Applications in monitoring human physiological performance

When it comes to human performance monitoring, as the demands for flexible wearable sensors have increased in recent years, a plethora of nanomaterials have been identified as promising candidates to design sensors that could replace those aforementioned bulky, rigid transducers [71]. By leveraging their extraordinary mechanical, electrical, and chemical properties, highly flexible and sensitive wearable sensors have been developed for monitoring various bio-signals [72, 73]. For example, Yamada *et al.* [74] grew carbon nanotube (CNT) forests onto poly(dimethyl siloxane) (PDMS), which functioned as the flexible substrate. The assembled device could be attached to different human body parts, and the strains generated at those regions can change the configuration of the CNT forest to cause corresponding detectable electrical resistance variations. Wang *et al.* [75] transferred graphene grown by chemical vapor deposition (CVD) to PDMS and medical tape. The resulting device showed high strain sensitivity potentially suitable for monitoring small human motions. Besides graphene and CNTs, nanowires (NW), such as silver NWs [76] and gold NWs [77], were also employed for

fabricating devices for monitoring human physical movements. On the other hand, human skin-inspired e-skins were also investigated [72, 73]. Pang *et al.* [78] developed a laminated patch-like sensor, in which nanofibers were mechanically interlocked. External forces could change the configuration of the nanofibers, and, hence, the electrical resistance would be altered accordingly. When attached to the waist, the sensor was sensitive enough to detect heartbeat. Kwak *et al.* [79] designed a skin patch with nanostructured micro-hairs, which allowed for dry attachment onto the human chest for ECG monitoring. Other nanomaterial-based wearable sensors also exhibited additional advantages, such as transparency [80, 81], self-powered [81, 82], and self-healing [83]. Despite these tremendous advancements, they generally required complicated fabrication procedures and are limited in scalability and cost efficiency.

1.4. Research Objectives and Dissertation Outline

Previous discussions have demonstrated that new sensing materials possess the potential to transform the data acquisition capabilities of structural and human performance monitoring systems. However, it remains challenging to employ these emerging material-based sensing systems for real-life monitoring tasks (*i.e.*, both in structural and human health monitoring contexts). One of the limiting factors is that they frequently required sophisticated designs and manufacturing procedures for integrating these functional materials, which may not be scalable, especially for large-scale infrastructure health monitoring. Thus, the primary objective of this dissertation is to develop high-performance multifunctional material-based sensing systems by leveraging the extraordinary electrical and mechanical properties of the nanostructured materials. The application targets include engineered structural systems as well as the human body. To overcome challenge of ultimately deploying these sensing systems practical monitoring applications, this dissertation aims to not only employ low-cost, efficient, and scalable

manufacturing techniques to fabricate the sensing materials but also to develop a systematic methodology for designing and optimizing the materials' properties for their specific applications.

Chapter 2 introduces three different bottom-up fabrication techniques to manufacture strain sensing nanocomposites, including spray fabrication, screen printing, and micro-patterning. In addition, the effectiveness of the manufacturing techniques has been evaluated based on a series of characterization experiments performed on the resulting nanocomposites' microstructures, electrical properties, and electromechanical performance. Here, CNTs and graphene are employed as sensing components, and the fabrication techniques are optimized for different material systems so as to obtain nanocomposite thin film sensors with consistent and optimal mechanical and electromechanical properties.

Based on the fabricated nanocomposites in Chapter 2, Chapter 3 proposes a topological design-based approach to strategically control the strain sensing performance of nanocomposites, which can potentially transform the current methodology of designing functional materials using a relatively empirical approach. In particular, Chapter 3 introduces different topologies to manipulate the uniaxial-tension-induced stress field distribution in nanocomposite thin films. The goal is to leverage stress-concentrating topologies to enhance strain sensing response while utilizing stress-releasing structures to decouple deformation effects for multifunctional sensing applications. The experimental findings are compared with numerical simulation results to demonstrate the effects of topological design of nanocomposite strain sensing performance.

In Chapter 4, the nanocomposite thin films are employed for monitoring human physiological performance (*i.e.*, as wearable sensors). Specifically, two different sensing systems are designed, namely, CNT fabric sensors and printed GNS sensors, which serve as building blocks

for smart garments and smart skins, respectively. They are designed to monitor human motions as well as vital signals, including respiration and pulsation.

However, to overcome the discrete sensing limitation of current electronic devices, Chapter 5 discusses a nanocomposite-based spatial sensing system that is capable of identifying, characterizing, and locating potential anomalies. To be specific, the strain sensing nanocomposites are coupled with tomographic imaging and signal processing algorithms to interrogate the electrical properties of sensing materials, which can be correlated to the mechanical performance of the corresponding structures to which they are attached. Chapter 5 introduces the mathematical formulations of electrical impedance tomography and compressed sensing algorithms while demonstrating the spatial sensing performance of the coupled system through spatially distributed pressure and damage detection experiments.

By building upon the results presented in Chapter 5, Chapter 6 demonstrates how these spatially distributed nanocomposite sensors can be applied for large-scale applications. Two applications are discussed, namely, monitoring seismic loading-induced structural damage in a full-scale reinforced concrete shear wall and smart socket prostheses for pressure ulcers prevention. This dissertation concludes with Chapter 7 summarizing the major findings in this study and a brief discussion of future research directions.

Chapter 2. Fabrication and Characterization of Piezoresistive Nanocomposites

2.1. Introduction

The primary objective of this chapter is to design, manufacture, and characterize multifunctional nanocomposites that are mechanically robust and possess electrical properties responsive to externally applied deformations (*i.e.*, they are strain sensitive or piezoresistive). By understanding their electromechanical properties, the goal is then to design and optimize the piezoresistive properties of nanocomposites and to ensure that they are compatible with low-cost and scalable manufacturing procedures. The expected outcome is that this study will pave way for future applications of these nanocomposites for strain sensing and structural health monitoring.

The approach to design these multifunctional nanocomposites is by incorporating CNTs and graphene as nanofillers in polymer matrices. CNTs and graphene are employed, because they possess extraordinary mechanical and electrical properties, such as high aspect ratios, low density, mechanical robustness [84-86], and intrinsic piezoresistivity [87-89], among others, which can be potentially translated to larger length scales and can enhance the properties of these

nanocomposites. It should be noted that, although extensive studies have been conducted on employing individual CNTs or graphene nanosheets (GNS) as sensing elements, it is nearly impossible to implement these nano-scale elements onto large-scale civil, aerospace, and marine structural systems for SHM. Therefore, this chapter mainly investigates nanocomposites with CNTs and GNS embedded in polymeric matrices as a more practical and effective approach to leverage the intrinsic nano-scale material properties of CNTs and GNS.

However, due to strong Van der Waals' and electrostatic forces that exist between many nanomaterials, CNTs and GNS tend to aggregate into bundles, which renders manufacturing high-performance nanocomposites challenging. These agglomerated nanofillers become localized inhomogeneous inclusions when embedded in a polymer matrix and can significantly compromise the mechanical and electrical performance of the resulting nanocomposites. Therefore, to disperse CNTs and GNS, many approaches have been used, including chemically functionalizing the nanostructures (*e.g.*, graphene oxide) or by means of mechanical excitation (*e.g.*, ultrasonication and shear mixing) [90].

Upon obtaining the dispersed nanofiller-polymer solutions, various techniques have been developed so far for fabricating nanocomposites. Some of the most commonly employed techniques include, for instance, spin coating [91], solution casting [92, 93], vacuum filtration [94], layer-by-layer (LbL) deposition [57], electrospinning [95, 96], screen printing [97, 98], and inkjet printing [99-102], to name a few. Upon investigating the material components involved in the aforementioned literature, one can find that different fabrication techniques may be more suitable for certain scenarios, depending on, for example, solution viscosity, particle dimensions, patterning requirements, temperature restrictions, and target applications, among others.

Therefore, it is important to optimize the manufacturing processes to effectively fabricate the nanocomposites so that desired performance and functionalities could be attained.

In this chapter, three different bottom-up fabrication techniques are introduced, including spray fabrication (Section 2.3), screen printing (Section 2.5), and micro-patterning (Section 2.6). Particularly, Section 2.3 focuses on using CNTs as nanofillers, while Sections 2.5 and 2.6 employs high-quality GNS, whose synthesis and characterization is discussed in Section 2.4. In addition, the detailed procedures of the manufacturing techniques are described in corresponding sections, where their effectiveness has also been evaluated based on a series of characterization experiments performed on the resulting nanocomposites' microstructures, electrical properties, and electromechanical performances.

2.2. Spray Fabrication of Carbon Nanotube Nanocomposites

2.2.1. Materials

All raw materials were used as is and without further purification. CNTs used in this study were multi-walled CNTs (MWCNTs) acquired from SouthWest NanoTechnologies (outer diameter: 6 to 9 nm; length: 5 μm; and purity: >95%). Poly(sodium 4-styrenesulfonate) (PSS) (molecular weight of ~ 1 Mg mol^{-1}) and N-methyl-2-pyrrolindinone (NMP) were from Sigma–Aldrich. The latex solution was from Kynar Aquatec. Other reagents, solvents, chemicals, and disposable laboratory supplies were purchased from Fisher Scientific.

2.2.2. Thin film fabrication procedure

The nanocomposite thin films were fabricated by spray-coating MWCNT-latex inks onto substrates using an airbrush. The spray fabrication technique was based on previous works by

Loyola *et al.* [103, 104] and Mortensen *et al.* [105]. In short, the first step involved preparing MWCNT-latex ink solutions. MWCNTs were initially mixed with a 2 wt% PSS aqueous solution with dilute amounts of NMP. Here, three MWCNT concentrations were used for fabricating sets of films with 1, 2, and 3 wt% MWCNTs. Then, the mixture was subjected to 60 min of high-energy probe sonication (3 mm tip, 150 W, 22 kHz) for dispersing MWCNTs. It should be mentioned that high-molecular weight PSS could wrap or align themselves along MWCNT surfaces during sonication, thereby enhancing steric stabilization and preventing MWCNTs from agglomerating. On the other hand, NMP was used to enhance MWCNT suspension and the dissolution of PSS and latex in solution. Once a well dispersed MWCNT/PSS-NMP solution was obtained, the Aquatec latex solution and 18 MΩ·cm deionized (DI) water were added in appropriate quantities to obtain the final sprayable ink. Here, latex was used, because an objective of this work was to create sprayable nanocomposite coatings that emulated the characteristics of common latex paints. In addition, the incorporation of latex increased the viscosity of the MWCNT-latex ink, which prevented the ink from flowing on the substrate after it was sprayed. Thus, films could be sprayed and patterned onto flat, curved, and vertical substrates.

For all the specimens fabricated in this study, a Paasche airbrush was utilized, and spraying was conducted immediately after ink preparation to avoid the ink becoming too viscous to be sprayed. Spraying was conducted in a fume hood and was performed manually by holding the airbrush ~ 30 cm perpendicular to the substrates and by moving the airbrush at a constant speed. After spraying, the thin films were air-dried inside the fume hood (for at least 3 h). It should be mentioned that manual airbrushing does not guarantee uniform films. However, the thin film specimens were prepared meticulously so as to guarantee the best possible quality and uniformity. Furthermore, MWCNT-latex thin films were deposited onto different substrates, namely, 25 × 75

mm^2 glass microscope slides and flexible 215 × 280 mm^2 poly(ethylene terephthalate) (PET) sheets, which were for characterizing the films' physical properties and sensing performance, respectively.

In addition, post-fabrication thermal annealing was also conducted on certain sample sets. The procedure involved transferring the dried nanocomposite films to a StableTemp Model 282A vacuum oven and annealing them at a temperature of 80 ˚C for 12 h, followed by 150 ˚C for 3 h, and in vacuum. It should be noted that this annealing process was optimized and determined mainly based on MWCNT-latex strain sensors' sensing performance. It was found that such annealing conditions could eliminate resistance drifts that would otherwise occur in the non-annealed specimens [106].

2.2.3. Electromechanical characterization

The MWCNT-latex thin films were subjected to electromechanical tests for characterizing their strain sensing properties. The test setup shown in Figure 2.1a depicts an MWCNT-latex film mounted in a Test Resources 150R load frame. In addition, an Agilent 34401A digital multimeter (DMM) was employed for measuring the thin film's electrical resistance (sampling rate: 2 Hz), while the film was subjected to various load patterns. Figure 2.1b shows a close-up view of an MWCNT-latex specimen mounted in the load frame. The applied load, crosshead displacement, electrical resistance, and time were recorded simultaneously and time-synchronized using a customized *LabVIEW* program.

Electromechanical tests were conducted by commanding the load frame to first apply a static pretension force of 0.03 N to ensure that the film was taut and vertically aligned with the axis of loading. In addition, each specimen was also checked to see if slippage between the

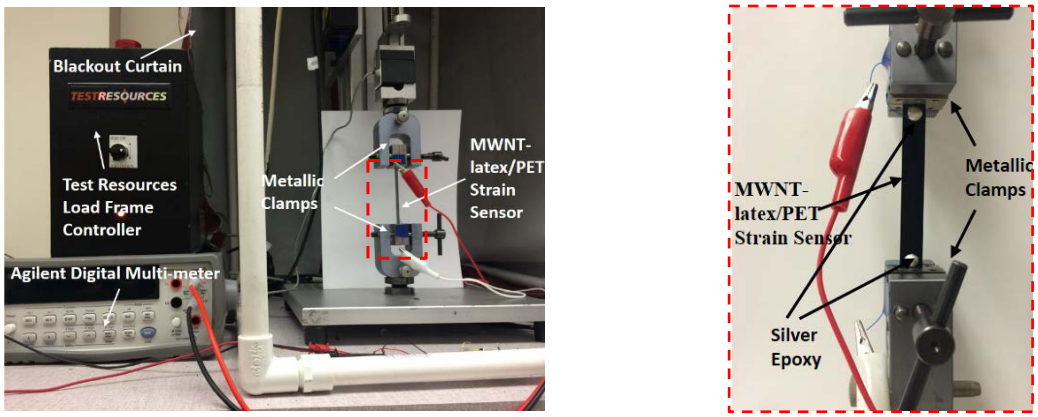

(a) (b)

Figure 2.1 (a) MWCNT-latex thin films were mounted in a Test Resources 150R load frame. A DMM was employed for measuring the specimen's electrical properties. (b) A close-up view of the highlighted film mounted in the load frame.

specimen and crosshead grips occurred. It should be mentioned that the load frame was equipped with serrated grips that were able to secure the specimens in place, and film slippage was rarely an issue. Then, each specimen was subjected to 5-, 10-, and 15-cycle tensile cyclic load patterns to a maximum applied strain of 0.5%. Multiple sets of these tests were conducted on the same specimen, and the load rate was varied to be 1, 2, and 3% min^{-1}.

For the annealed films in which their electrical resistances stabilized after some initial exponential decay, one could compare their baseline resistances as a function of different MWCNT concentrations, as is shown in Figure 2.2. It can be seen that films of higher MWCNT concentrations tended to have lower nominal resistance. This result agrees with the percolation-based numerical modeling results obtained by Lee and Loh [33] and can be explained by the fact that greater CNT concentrations provide more electrical conductive pathways for current to flow through the material, thereby decreasing resistance. Figure 2.2 also shows each sample set's

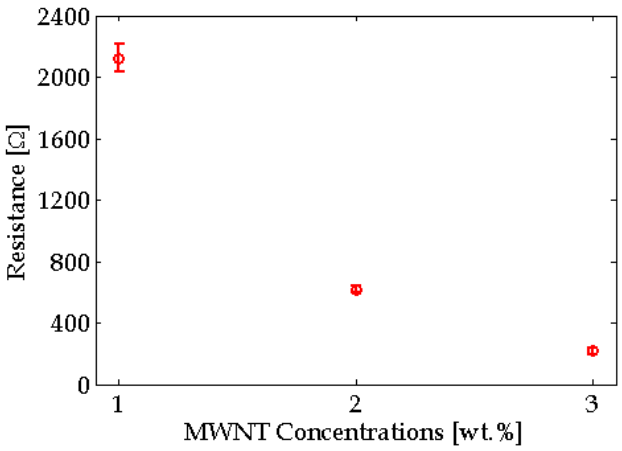

Figure 2.2 The average nominal electrical resistance and standard deviations (as error bars) of annealed MWNT-latex thin films.

standard deviation as the error bar, and it is clear that the nominal resistance differences are statistically significant. It also appears that the rate of resistance decrease became slower with higher MWCNT concentrations; however, only three concentration sets were investigated in this study, and more data is needed to verify this observation, which is the focus of future investigations.

Representative resistance time histories of annealed 1 wt% MWCNT-latex thin films were overlaid with the corresponding 5-cycle (load rate: 1% min^{-1}) applied strain patterns, as shown in Figures 2.3a. It was found that, regardless of MWCNT concentration, load rate, and the number of load cycles, the films' electrical resistance increased in tandem with increasingly applied strains, and the opposite was true during unloading. In addition, Figure 2.3b plots the corresponding normalized change in resistance (ΔR_n) with respect to the applied strains. Here, ΔR_n is calculated as the difference between the film's resistance at any instant (R_i) and its nominal resistance (R_0), then normalized by R_0 as follows:

$$\Delta R_n = \frac{R_i - R_0}{R_0} \tag{2.1}$$

The films' strain-sensitive electromechanical properties could be a result of two effects. The first is that the applied strains could induce rigid-body motions of MWCNTs within the polymer matrix. In this case, tension would decrease the number of nanotube-to-nanotube junctions, thereby decreasing the number of electrical conductive pathways to cause an increase in the measured electrical resistance of the bulk film. On the other hand, MWCNTs embedded in the polymer matrix could also deform due to stress and strain transferred from the externally applied loads [107], which would decrease the conductance of each MWCNT with increasingly applied tensile strains to cause the bulk film to also exhibit higher electrical resistances [88, 108]. It should be noted that Lee and Loh [33] also numerically modeled this latter effect. If larger strains were to be applied to these films, it is also possible that nanotubes may be pulled out of the matrix or be fractured [109, 110]. However, this would likely induce damage to the films and cause its nominal resistance to increase, which was not the case observed in these tests.

Using the resistance time histories and applied strain patterns, the strain sensitivities of MWCNT-latex thin films were also evaluated for films of different MWCNT concentrations and tested with different load rates and number of load cycles. The strain sensitivity or gage factor (*GF*) of each film was determined using the following equation:

$$GF = \frac{\Delta R_n}{\Delta \varepsilon} \tag{2.2}$$

where $\Delta\varepsilon$ is the change in applied strain corresponding to the change in normalized resistance measured. In fact, strain sensitivity is equivalent to the slope of the linear least-squares regression line fitted to the ΔR_n versus ε data, as shown in Figure 2.3b.

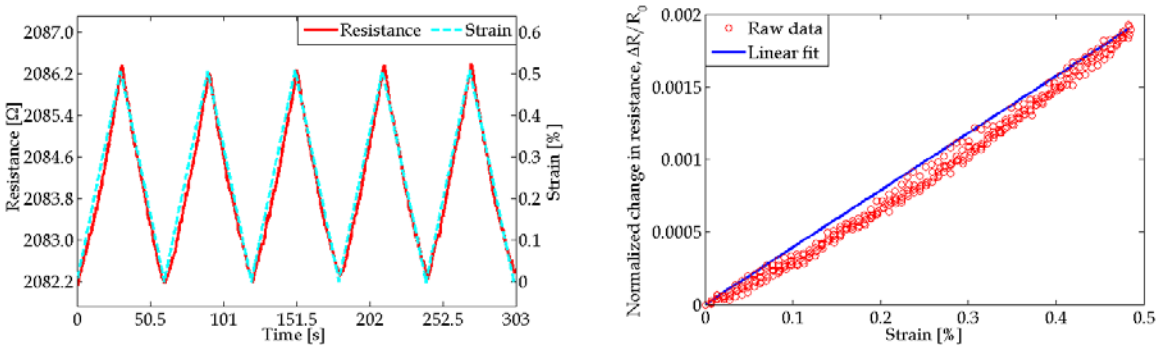

(a) (b)

Figure 2.3 Representative electromechanical response of an annealed 1 wt% MWCNT-latex thin film: (a) resistance time history overlaid with the applied 5-tensile-cyclic load pattern to 0.5% (load rate: 1% min^{-1}) and (b) corresponding normalized change in resistance (for all 5 cycles) plotted as a function of applied strains (R^2=0.9699).

The average strain sensitivities and corresponding standard deviations for all the various sample sets were calculated and shown in Figure 2.4. From Figure 2.4, two distinct trends can be observed. First, MWCNT-latex thin films of higher MWCNT concentrations were characterized by higher strain sensitivities. In fact, this observation was consistent with other types of CNT-based strain sensors [57, 111]. It is clear from the results shown in Figure 2.4 that strain sensitivity differences due to changes in MWCNT concentrations were statistically significant, especially given the small standard deviations (error bars). This trend of increasing strain sensitivities can be explained by the fact that nominal bulk film resistance decreases with increasing MWCNT concentrations. Since R_0 is the reference value in which changes in resistances are based on (see Equations 2.1 and 2.2), any reductions in the denominator translates to higher strain sensitivities. In other words, assuming that all else being equal, the relative resistance change appears to be larger since nominal resistance is lower for films of higher MWCNT concentrations. It should also be mentioned that the MWCNT-latex thin films investigated in this study exhibited slightly lower strain sensitivities as compared to some other types of CNT-based strain sensors [111]. Sensitivity

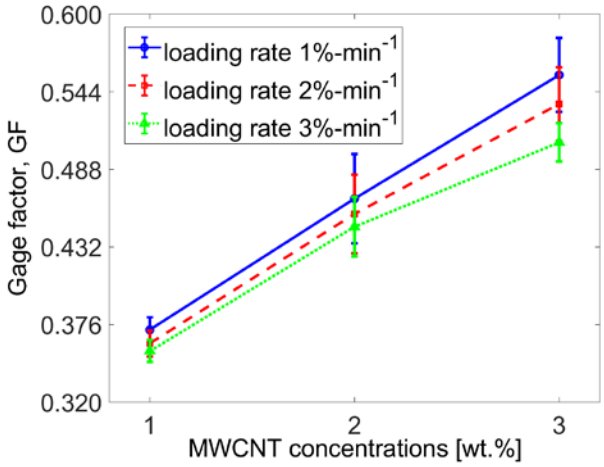

Figure 2.4 Average strain sensitivities (and standard deviations as the error bars) of films of different MWCNT concentrations tested using different load rates.

variations between different types of thin films could be a result of different interfacial properties between the CNTs and its polymer matrix [112]. Future research will employ both experimental and numerical techniques for clarifying this relationship and for testing this hypothesis.

2.3. High-Performance Graphene Nanosheets

2.3.1. Water-assisted liquid phase exfoliation

The scalable production of high-quality GNS is a critical milestone for various potential applications, including strain sensing [113], nanoelectronics [114], nanocomposites [115], energy conversion and storage [116], catalysis [117], and biomedical applications [118]. Among those applications, GNS provides tremendous opportunities for improving the properties of next-generation strain sensors [113, 119], in particular, by leveraging their nanostructured two-dimensional (2D) morphology and extraordinary mechanical and electrical properties [115, 120, 121]. Over the last decade, various methods have been introduced for the synthesis of GNS, including micromechanical exfoliation [122], CVD [123], the reduction of GO [124], and liquid-

phase exfoliation (LPE) of bulk graphite in various solvents [125]. Although the bulk production of GNS by reduction of GO is a popular method [124, 126], the drastic conditions (*i.e.*, the use of strong reducing agents or high temperature) involved in the reduction process often introduce impurities or defects in RGO, which affect the intrinsic properties of GNS. In addition, the synthesis of RGO chemically or thermally is time-consuming, laborious, and hazardous for the environment. While CVD is capable of producing almost defect-free GNS, the yield is low in terms of bulk production. In contrast, LPE of bulk graphite via sonication in various solvents [127, 128] to prepare GNS has attracted considerable attention due to its simple operations, low defects in the produced nanosheets, and minimal environmental impact [129]. Recently, mixtures of solvents have been demonstrated as successful liquid phases to improve the yield and quality of GNS, as well as other 2D layered materials in LPE [130].

Here, low-defect few-layer GNS were synthesized from graphite microcrystalline powders (-325 mesh, 99.995 % pure, Alfa Aesar) using a surfactant-free, efficient, and economical LPE process [128] by using a water-NMP (99% extra pure, Acors Organics) mixed solvent. Figure 2.5 summarizes the entire experimental method employed for exfoliation of each material. The same 14 mL centrifuge tubes were used throughout the experiments to avoid material loss due to transfer. Here, 50 mg of each material were measured and placed in 14 mL centrifuge tubes with an initial

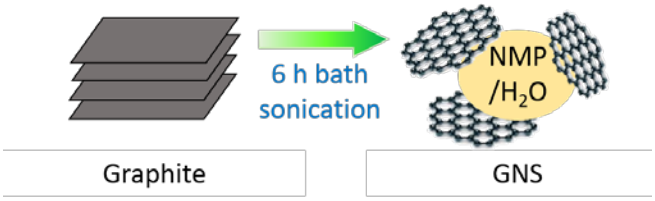

Figure 2.5 Schematics of GNS exfoliated from bulk graphite using an 8:2 NMP/H_2O solvent.

concentration of 5 mg mL^{-1} for exfoliation. The materials were to bath sonicated for 6 h (Elma sonic P60H) at a fixed nominal power and frequency of 100 W and 37 kHz, respectively. The positions of each sample tube were interchanged every 30 min to subject the mixtures to uniform power distribution. The water of the bath sonicator was replaced with normal cold water every 30 min to minimize temperature increase during sonication, and the temperature was maintained between 27 to 37 ˚C. Sample dispersions were left overnight after sonication, followed by centrifugation at 3000 rpm for 30 min using a Hettich EBA20. The top 75% of the colloidal supernatant was first collected. Then, the supernatant was kept undisturbed for 24 h for further precipitation, if any, and the upper 67% portion of the colloidal supernatant was used for characterization. Every experiment was repeated for five times to obtain statistically representative results and to account for experimental error.

Ex situ characterization of the as-produced LPEGNS was performed by transmission electron microscopy (TEM) and micro-Raman spectroscopy. Cold-field emission Cs-corrected TEM (JEOL ARM-200F) with 200 kV accelerating voltage was used. Carbon-coated copper grids (400 mesh) were used for TEM sample preparation. Figure 2.6 shows the TEM images of the as-synthesized GNS at different magnifications. The red arrows in Figure 2.6c indicate the distinct layers of GNS, showing that they had few layers as well as relatively intact nanostructures.

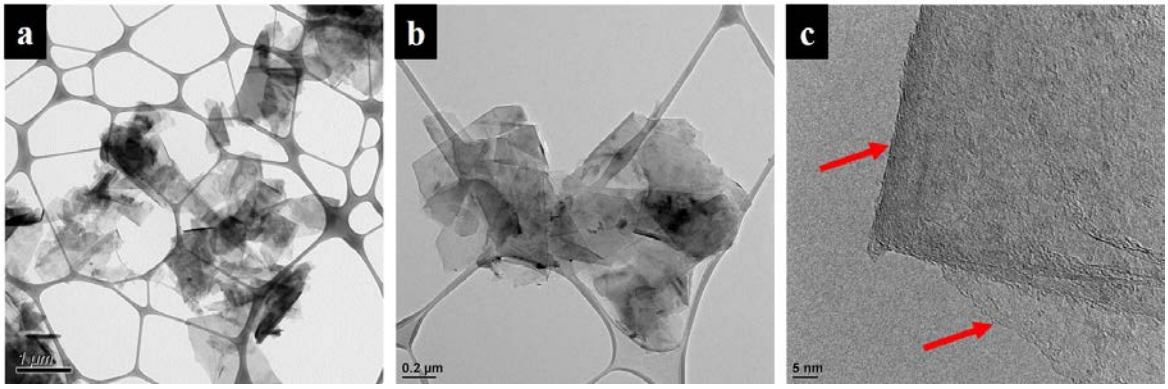

Figure 2.6 (a – c) TEM images of different magnifications for the GNS synthesized by the WALPE method. The red arrows in (c) indicate the distinct edges of the few-layer GNS.

In addition, Raman scattering was performed at room temperature with a JASCO 5100 spectrometer (λ = 533 nm). The thin films for Raman analysis were prepared on silicon wafers and dried in a hot air oven at 60 ˚C. The Raman spectrum of the LPEGNS is shown in Figure 2.7. The impurities or defects in the graphene basal plane were quantified from the intensity ratio of D to G band (I_D/I_G). The low value of I_D/I_G (~ 0.60) and high 2D peak intensity of GNS indicated that the water-NMP co-solvent approach resulted in fewer defects in GNS during synthesis [128, 131, 132]. The water-assisted LPE (WALPE) method was capable of obtaining high-quality GNS due to the interactions between GNS and the co-solvent. In particular, the bulky $(NMP{\cdot}2H_2O)_n$ aggregates, formed due to water-NMP hetero-association, can generate inter-sheet repulsive forces and separate individual GNS with non-overlapping Leonard-Jones (L-J) potentials [128, 133]. Therefore, the WALPE method can preserve the unique properties of graphene and is potentially more suitable for scale-up and enhancing bulk sensor performance.

2.3.2. Bulk performance comparison with reduced graphene oxide

To validate that the superior material properties of the LPEGNS could translate to the bulk-scale, the LPEGNS- and RGO-based flexible graphene paper specimens were fabricated and their electrical properties and strain sensing properties were compared. First, RGO was synthesized following typical procedures. To be specific, 0.1 g of natural graphite was suspended in 100 mL of H_2SO_4, followed by stirred, using a magnetic stirrer, at 300 rpm for 2 h until a visually homogeneous black solution formed. Then, $KMnO_4$ of different quantities was slowly added to the solution and further stirred for another 2 h at room temperature. After that, the temperature was gradually raised to different temperatures and then maintained for 2 h in a water bath (IKA-HS7 digital). When the reaction completed, the product was removed from the heat source, allowed to cool to room temperature, and was then poured into 350 g of ice containing 5 mL of 35% H_2O_2 (*i.e.*, to prevent precipitation of insoluble MnO_2). The mixtures were then centrifuged (at 24,500 rpm and for 30 min) to obtain crude solid (Beckman, Avanti J-25). The solid was removed and then bath-sonicated in 60 mL of DI water for 30 min (IKA-HS7 digital). The material was bath-

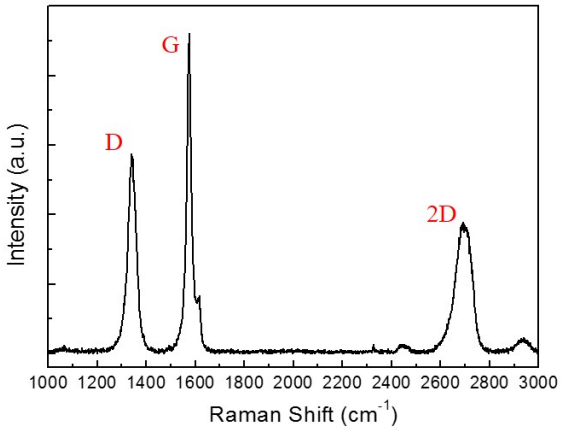

Figure 2.7 A representative Raman spectrum of the as-synthesized LPEGNS.

sonicated again by adding 30 mL of HCl, and the dispersion was centrifuged (24,500 rpm and 30 min). Furthermore, the collected solid was removed and then bath-sonicated in 60 mL ether for 30 min. The purified GO was then obtained by collecting the centrifuged (24,500 rpm and 30 min) solid. Finally, exfoliation of GO was conducted by heating it (~ 10 ˚C min^{-1}) to 1,000 ˚C in an inert Ar atmosphere. After thermal reduction, RGO were obtained.

To fabricate graphene paper specimens, 0.5 mg mL^{-1} GNS (RGO and LPEGNS) were first added to 0.5 wt% polyoxyethylene (40) nonylphenyl ether (IGEPAL® CO890, average M_n ~ 1982, branched) aqueous solution (Figure 2.8a). Here, a water-based solution was preferred over organic solvents (*e.g.*, NMP) so as to avoid damaging the cellulose structure of paper fibers or compromising the mechanical properties of the paper substrates. The mixture was then subjected to 2 h of high-energy probe sonication (3 mm tip, 150 W, 22 kHz) for dispersing GNS (Figure 2.8b). Second, using disposable pipettes, 6 mL of GNS-CO890 solution was deposited to cover a 12 × 2.5 cm^2 rectangular area on paper, as is shown in Figure 2.8c. The surface tension of the solution was found sufficient for confining the solution within the rectangular area and, hence, ensured that the amount of GNS deposited in each paper specimen was the same. Note that the deposition was conducted on a horizontal platform, on which the GNS-CO890 solution could be uniformly distributed. After being air-dried at room temperature overnight, the GNS paper were cut to form 14 × 1 cm^2 specimens (with 1 cm margins on both the longitudinal ends of the specimen, as is shown in Figure 2.8d. Figure 2.8d also illustrates the technique for establishing electrodes, in which copper tape strips were sandwiched between two layers of conductive silver paste so as to minimize contact resistance. Here, the gage length was 30 mm. On the other hand, to improve the ease of fabricating LPEGNS-based samples, ethanol was added to 0.7 mg mL^{-1} LPEGNS-CO890 dispersed solutions (5:1 sonicated solution-to-ethanol by volume), and the mixture was then

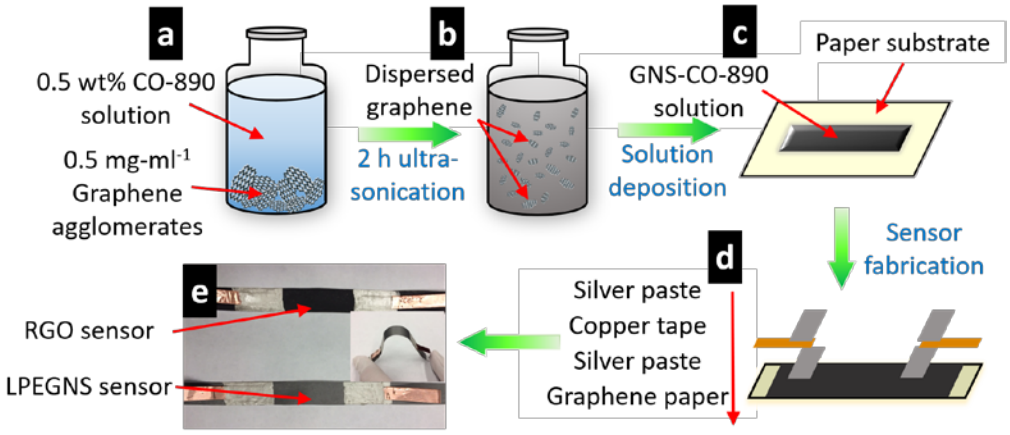

Figure 2.8 The graphene paper strain sensors were fabricated using a multi-step solution-based process. (a) graphene nanosheets were dispersed by subjecting graphene and CO890 solution mixture to (b) 2 h of ultrasonication. (c) Sonicated solution was uniformly deposited on printer paper. (d) Electrodes were established on both ends of completely dried specimens. (e) A photograph of an assembled RGO-CO890 and LPEGNS-CO890 (light grey) paper sensor are shown; the inset shows the graphene paper sensor was highly flexible.

subjected to cold bath sonication for 30 min. The fast evaporation of ethanol could accelerate the integration of GNS with the paper fibers. In addition, a syringe was used to deposit the dispersed LPEGNS-CO890/ethanol solution to form 60 × 2 mm^2 thin rectangular strips on paper. After the samples fully dried, electrodes were attached as shown in Figure 2.8d, and the gage length was 20 mm. Moreover, post-fabrication thermal annealing was conducted by subjecting the dried LPEGNS-based samples to annealing at 180 ˚C for 1 h in vacuum using a vacuum oven (ADP300C, Yamato Scientific America). It should be noted that all electrical measurements were performed after annealed sample sets cooled down to room temperature overnight. One can observe from the photograph of fabricated sensors (Figure 2.8e) that LPEGNS and RGO were uniformly distributed and were well-integrated with paper fibers, and the incorporation of GNS did not compromise the flexibility of the pristine substrate (inset of Figure 2.8e).

Figures 2.9a and 2.9b show the representative nominal resistance time histories of RGO-CO890 and LPEGNS-CO890 paper sensors, respectively; the plots also include their average unstrained resistance values and standard deviations. It was found that samples fabricated with RGO possessed significantly higher resistance than their LPEGNS-based counterparts. The inferior bulk electrical conductivity of RGO-based sensors could be mainly attributed to the structural defects in the nanosheets that were inevitably introduced when removing the oxygen-containing groups. Furthermore, upon closer examination of the resistance time histories over a period of 500 s (insets of Figures 2.9a and 2.9b), RGO-CO890 paper sensors exhibited a higher noise floor. Here, the root-mean-square (RMS) noise (R_{RMS}) of the nominal resistance data were calculated using Equation 2.3,

$$R_{RMS} = \sqrt{\frac{1}{n}\sum_{i=1}^{n}(R_i(t) - R_{ave})^2} \tag{2.3}$$

where R_i represents the measured resistance data as a function of time (t), whose average is denoted by R_{ave}, and n is the total number of measurements included. It should be mentioned that R_{ave} is also regarded as the nanocomposite's unstrained nominal resistance. The calculated RMS noise values for the two sample sets tested are listed in Figures 2.9a and 2.9b, which confirmed that the RGO-CO890 sensors were characterized by significantly higher noise. It is hypothesized that RGO-CO890 graphene paper nanocomposites contained unstable or defective conductive pathways, which could be more susceptible to external stimuli (*e.g.*, changes in ambient

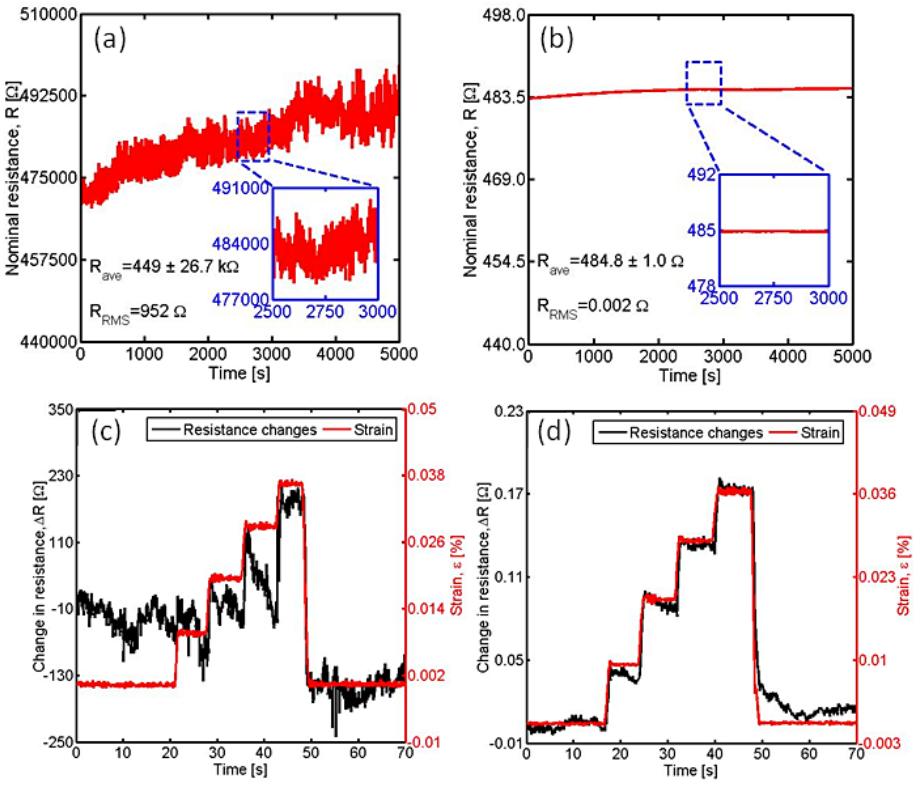

Figure 2.9 Representative unstrained nominal resistance time histories of (a) RGO-CO890 and (b) LPEGNS-CO890 paper sensors are shown. The corresponding insets show closer examinations of resistance fluctuations over a 500-s window for evaluating noise floor. The electromechanical responses of an RGO- (c) and LPEGNS-CO890 paper sensor (d) are overlaid with the applied strain pattern (measured using the foil strain gage).

temperature, humidity, and light), resulting in considerable variations (or noise) in their electrical resistivity.

Furthermore, the strain sensing performances of RGO and LPEGNS were also compared by conducting load tests. Here, a commercial foil strain gage (*GF* of 2.13 ± 1% at room temperature) was installed on the beam and parallel to the graphene paper sensors using epoxy for measuring induced strains (*i.e.*, as benchmark tests). In contrast, double-sided tape and Kapton tape were employed for affixing the GNS paper sensors onto the test beam, since epoxy might affect the intrinsic electrical properties of these specimens. The interface was strong and reliable

enough that no slippage was observed during the tests. Then, quasi-static strain was applied uniformly to both the GNS paper sensor and strain gage by gently placing weights onto the free end of the beam, the test setup is shown in Figure 2.10. Here, two Keysight 34465A DMMs were employed to simultaneously measure the electrical resistance of the GNS paper sensor and strain gage. Both DMMs were controlled by a Keysight *BenchVue* program, which also recorded all the data.

Figures 2.9c and 2.9d show the resistance changes of RGO- and LPEGNS-based samples when subjected to applied strains, respectively. The electromechanical response of RGO-CO890 samples could be barely detected because of the dominant effects of noise during applied strains (Figure 2.9c). On the other hand, one can observe from Figure 2.9d that the resistance of LPEGNS-based sensors increased in tandem with increasingly applied tensile strains and without any phase lag. During the unloading process, the paper sensors' resistance decreased simultaneously and returned to their initial unloaded resistance. The piezoresistivity of graphene paper could be

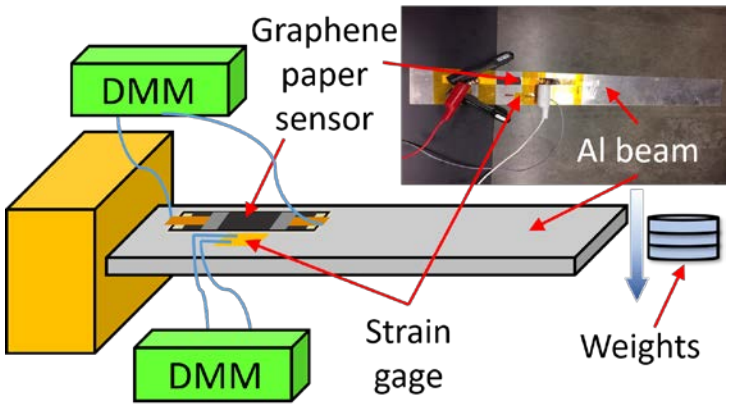

Figure 2.10 A graphene paper sensor and a foil strain gage were both affixed onto an aluminum cantilevered beam, whose electrical resistances were measured using DMMs. The inset is a photograph of the test setup. Quasi-static strain was applied by loading the free-end of the beam using weights.

primarily contributed by the disturbance of electrically conductive pathways in the nanocomposite under applied strains. In particular, portions of deposited GNS could experience strain-induced rigid-body motion (along with the paper fibers) to become physically and electrically disconnected (during applied tensile strains), which would disrupt the originally formed conductive network and impede electrical current flow. As a result, the bulk electrical resistance of the nanocomposite would increase correspondingly. When tensile strains were removed, the paper fibers restored to their previous configurations, enabling LPEGNS to re-establish the initial percolation network and reducing bulk film resistance to its initial value. The assumption of elastic behavior of paper is valid given that only small strains were applied and that no residual strains (or permanent deformation) were observed after the tests. However, for RGO-based specimens, since the conductive network itself was unstable and that RGO was sensitive to ambient effects, the nanocomposite's piezoresistivity was unreliable, if detectable at all. Therefore, the superior quality of LPEGNS versus RGO is crucial for manufacturing paper-based thin films with favorable strain sensing properties.

In situ Raman spectroscopy of LPEGNS-CO890 at variable strains was performed to examine the effect of strain on the hexagonal graphene layers (Figures 2.11a and 2.11b**)**. Figure 2.11a clearly shows there is a shift in the G mode frequency of LPEGNS under applied strain. An LPEGNS film on paper substrate was sufficiently sensitive to respond at weak strain (0.02 %), which also implied the high quality (low-defect) of the LPEGNS. Despite of an irregular trend, G mode showed an overall blue-shift over the entire strained graphene. The irregularity might be due to the nonuniform strain distribution over the LPEGNS layers. The nonuniformity could be attributed to the consequence of van der Waals interaction between paper substrate with graphene nanosheets [134]**.** On the other hand, an overall decreasing trend was observed in I_D/I_G profile with

increasing strain (Figure 2.11b), which implied that the applied strain did not introduce defects or deformations in graphene layers. The effect of strains on LPEGNS was also investigated by SEM measurements (Figures 2.11c to 2.11f). It was noted that no significant deformation due to strain could be observed from SEM images taken at high (Figures 2.11d and 2.11f) and low magnifications (Figures 2.11c and 2.11e).

In summary, the proposed WALPE technique has been demonstrated to be capable of synthesizing GNS of reduced defect densities. To assess the benefits of different GNS and how these material properties translated to larger length-scales, strain sensing validation tests were conducted on solution-cast GNS paper specimens. It was found that the LPEGNS paper strain sensors exhibited higher electrical conductivity, lower noise floor, and more stable electromechanical response as compared to their RGO-based counterparts. Therefore, more intact nanostructures of the as-synthesized LPEGNS could significantly benefit their applications as strain sensing transducers. To effectively leverage the superior electrical properties of high-quality GNS, the following work on the development of graphene nanocomposites was all based on the as-synthesized LPEGNS.

2.4. Screen Printing of Graphene Nanocomposites

2.4.1. Materials

Ethyl cellulose (EC) was purchased from Sigma-Aldrich (viscosity 100 cP, 5% in toluene/ethanol 80:20, 48% ethoxyl). It should be noted that the biocompatibility and flexibility of cellulose is suitable for wearable devices that can potentially make contact with human skin. In addition, cellulose possesses comparable surface energy characteristics, which could facilitate

better separation of individual GNS during ultrasonication. Here, ethanol was used to solubilize cellulose while providing faster drying during film fabrication. Conductive silver paint was purchased from Ted Pella for establishing electrodes on the fabricated nanocomposites.

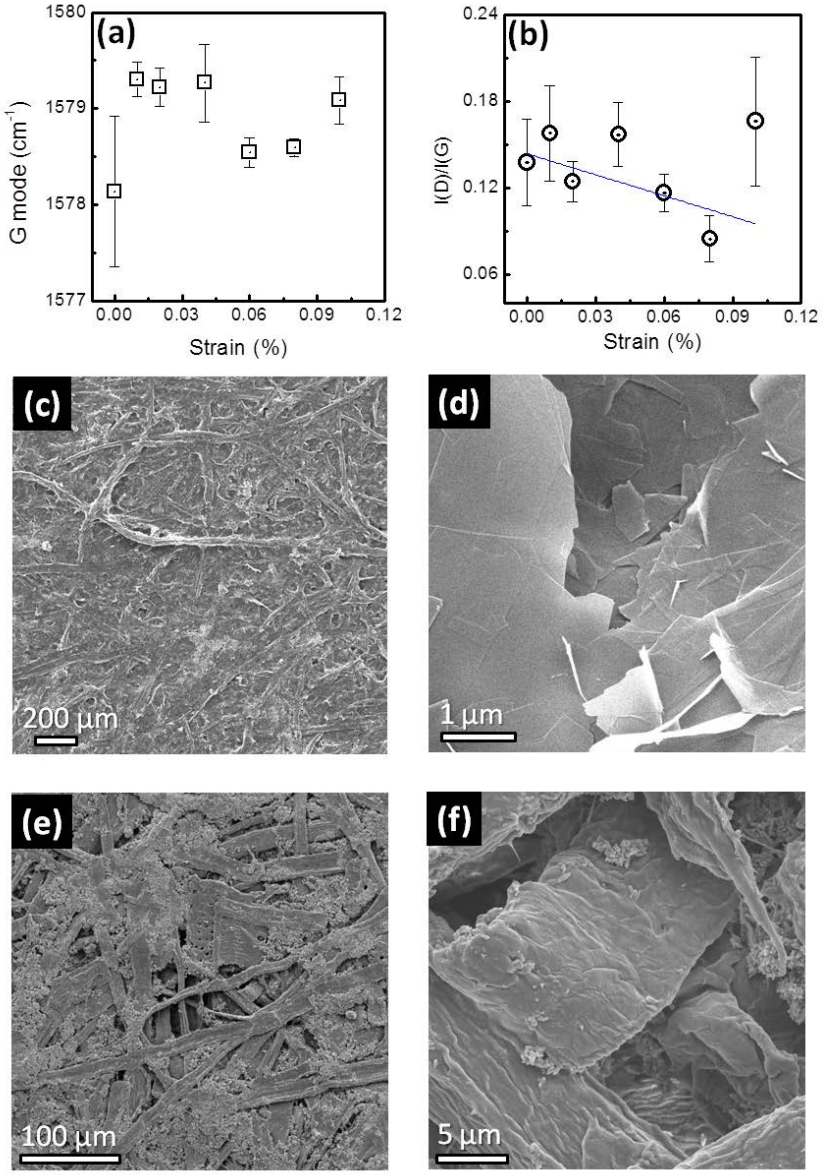

Figure 2.11 Effects of strain on the LPEGNS-CO890 on paper substrates. (a) and (b) Raman spectroscopic analyses, (a) average G mode frequency and (b) average I_D/I_G as functions of applied strains. The error bars are the standard deviations. (c) and (d) SEM images of unstrained LPEGNS-CO890 samples. (e) and (f) and SEM images of LPEGNS-CO890 samples after being subjected to 0.1 % strain.

2.4.2. Thin film fabrication procedures

Figure 2.12 shows the schematics of the fabrication procedures. First, the dispersing agent was prepared by dissolving EC in ethanol through 24 h of stirring at room temperature. Then, 2 mg mL^{-1} GNS were mixed with the EC/ethanol solution and the mixture was subjected to 2 h of ice bath sonication (Figure 2.12a). Here, the ice bath could effectively minimize ethanol evaporation, which would otherwise induce GNS agglomerations. To achieve optimal solution viscosity for screen printing, the dispersed GNS-EC/ethanol solution was heated with a hot plate at 50 ˚C for ~ 10 min (Figure 2.12b). It should be noted that the solution was continuously stirred during heating to guarantee uniform heating and efficient evaporation of ethanol. After obtaining the viscous GNS-based solution, it was coated onto PET substrates through masks, whose patterns could be pre-cut using laser cutter (Figure 2.12c). Finally, the coated GNS-EC patterns were air-dried overnight at room temperature to evaporate the residue ethanol. For the following tests on electrical properties of the GNS-EC nanocomposites, the electrodes could be established on the nanocomposite thin films with colloidal silver paint, as shown in Figure 2.12d.

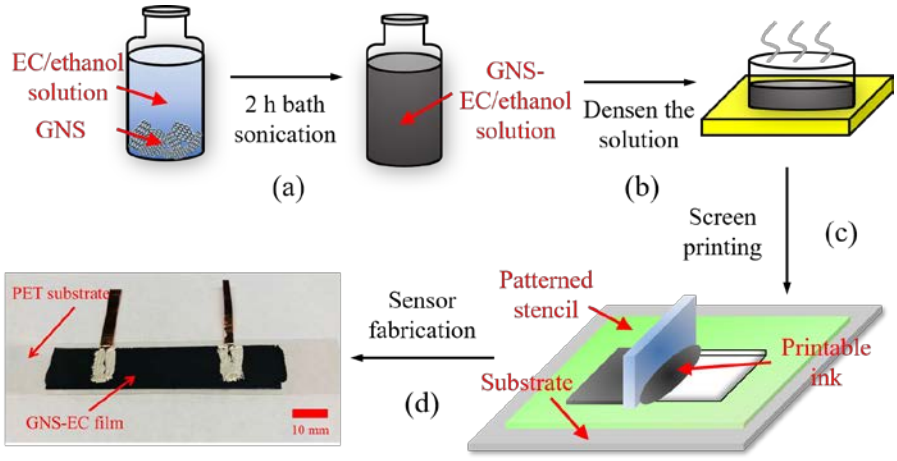

Figure 2.12 Schematics of screen printing fabrication of GNS-EC nanocomposite thin films.

2.4.3. Electromechanical characterization

The strain sensing performance of the GNS-EC nanocomposite thin films were characterized by conducting load tests. Here, a Test Resources 150R load frame was employed to apply tensile cyclic strain patterns (load rate: 10 % min^{-1}; peak strain: 1%) to the thin film specimens, while a Keysight 34465A DMM was used for measuring changes in thin film resistance during applied loading. The electrical resistance time histories of the various patterned specimens were recorded and digitized using Keysight *BenchVue*.

Figure 2.13a shows the representative ΔR_n time history of a GNS-EC specimen, which exhibited good agreement between the thin films' resistance change and applied tensile strain pattern. Thus, the screen-printed GNS-EC thin films possessed piezoresistive properties and could be potentially used as strain sensing elements.

To further characterize the strain sensitivity of the nanocomposites, Figure 2.13b plots the ΔR_n as a function of applied strain. One can observe a slight nonlinear response. In order to

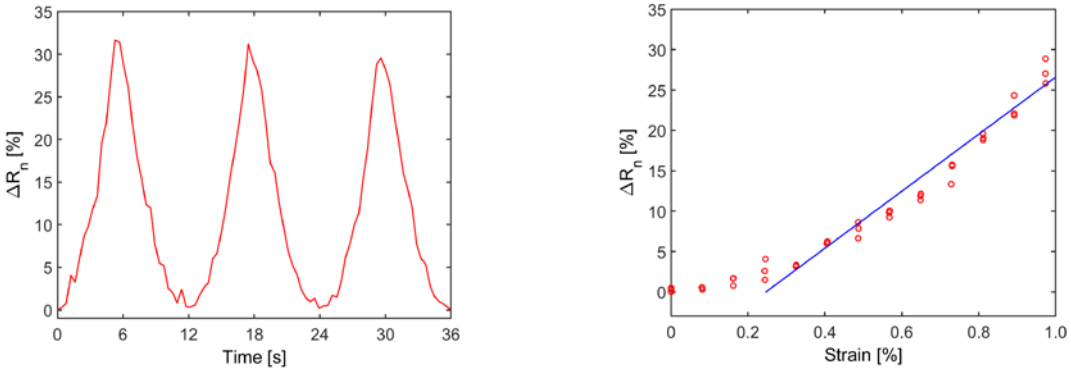

(a) (b)

Figure 2.13 (a) Representative ΔR_n time history of a GNS-EC thin film. (b) Corresponding ΔR_n (for all 3 cycles) plotted as a function of applied strains.

quantify its *GF* using Equation 2.2, the specimen's response to strains ≥ 0.3% was approximated to be linear and was fitted by a least-square regression line, as is shown in Figure 2.13b. The evaluated *GF* was ~ 37, which was about 18 times more sensitive than commercial strain gages.

2.5. Micro-Patterning of Graphene Nanocomposites

2.5.1. Materials

IGEPAL® CO890 was purchased from Sigma–Aldrich. Ultrathin (8 μm) medical tape was provided by Nitoms (XTRATA® Perme-Roll AIRTM). Conductive thread and conductive silver paint were purchased from Adafruit and Ted Pella, respectively. Dragon Skin® FX-Pro was from Smooth-On.

2.5.2. Thin film fabrication procedures

To obtain printable GNS-based ink, 0.5 wt% CO890 was first dissolved in DI water by bath sonication (Fisher® Scientific) for 1.5 h. Second, a mixture of 1 mg mL^{-1} of as-synthesized

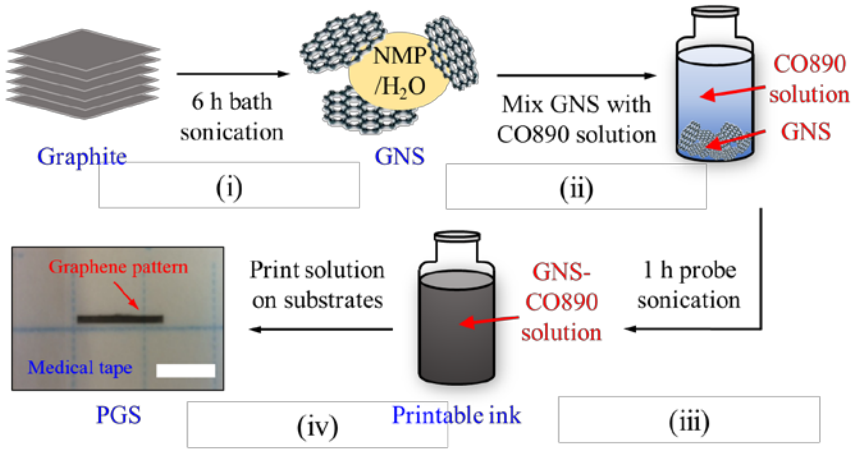

Figure 2.14 Schematic illustration for (i) GNS synthesis, (ii and iii) printable ink preparation, and (iv) micro-patterning the ink on the substrates. Scale bar, 10 mm.

WALPE GNS in 0.5 wt% CO890 aqueous solution was subjected to 1 h of high-energy probe sonication (3 mm tip, 150 W, 22 kHz), as is shown in Figure 2.14 (steps ii and iii). Here, an aqueous solution was used instead of organic solvents to maintain compatibility with the printing substrates. Then, a Microplotter® (SonoPlot) was employed for patterning the dispersed GNS-CO890 solution onto ultrathin medical tape at room temperature, forming pre-designed, 2D geometrical patterns during fabrication (step iii) [135]. The printing resolution was ~ 60 μm. It should be noted that the Microplotter® can fabricate complex geometries, but, in this study, the sensing elements were only rectangular for simplicity sakes. Then, the as-printed patterns were air-dried at room temperature. Unlike traditional patterning techniques (*e.g.*, photolithography, soft lithography, and screen printing), the patterned printed graphene sensor (PGS) was fabricated at a low temperature and without the use of masks and molds. In particular, each GNS-based sensing element was pre-designed as 12 × 1 mm^2-thin rectangles using *AutoCAD* (Autodesk). The designed patterns could be printed multiple times onto the previously deposited layer, where each pass of the Microplotter® formed one monolayer of the multi-layered PGS. Finally, the electrodes were established on the printed patterns by drying conductive silver paint over the sensing element and electrically conductive threads.

2.5.3. Microstructure characterization

The microstructure of the printed graphene patterns was investigated using micro-Raman spectroscopy and SEM. Here, specimens were fabricated by printing 4- and 14-layer GNS sensing elements onto PET substrates. It should be noted that, instead of using medical tape, the rigidity and transparency of the PET substrates made it easier to perform microscopy. In particular, micro-Raman scattering studies were performed at room temperature with a JASCO 5100 spectrometer (λ = 533 nm). The Raman spectra were recorded using 10 random spots on the specimens. The

effect of laser heating was avoided by maintaining the laser beam intensity at 0.1 mW. In addition, a JEOL JSM-6500F SEM was used to qualitatively observe the surface morphologies of the printed graphene patterns. The accelerating voltages were set to be between 10 to 15 kV.

Figure 2.15a shows the representative Raman spectra of the printed graphene sensing element. The result shows three typical peaks, namely, the D, G, and 2D bands at 1340, 1577, and 2692 cm^{-1}, respectively, which are consistent with previously reported Raman spectrum of LPEGNS [136, 137]. The increase in the dominance of GNS' featured peaks indicates that a denser graphene network was established as more ink was printed, which was further characterized using SEM, as is shown in Figures 2.15b (i) and (iii). In addition, Figures 2.15b (ii) and (iv) show the magnified view of the GNS network's 2D film-like surface morphology, which implies that graphene was efficiently dispersed and deposited without aggregation.

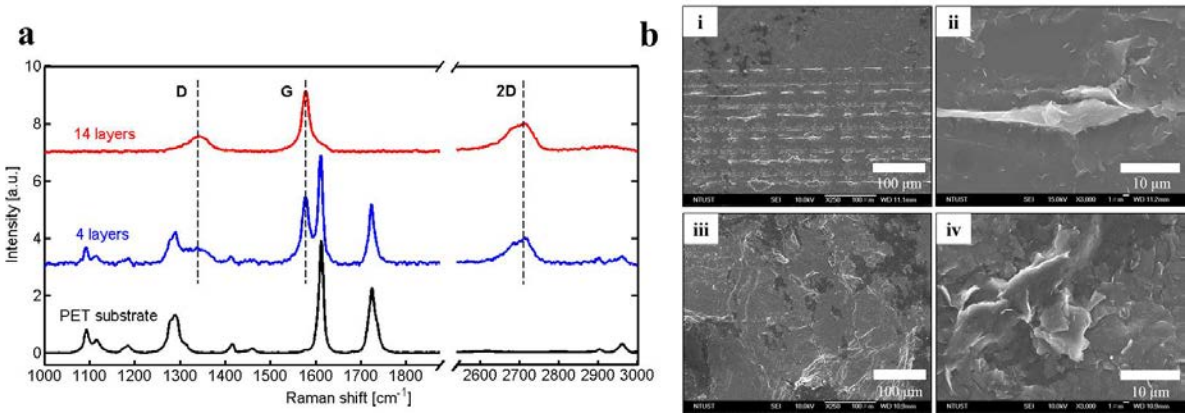

Figure 2.15 (a) Representative Raman spectra of the printed graphene network (i.e., 4- and 14-layer films) and the PET substrate. The intensity is of arbitrary unit for easy comparison. (b) SEM images of the surface morphologies of the (i) 4- and (iii) 14-layer GNS networks. (ii) and (iv) are magnified views of (i) and (iii), respectively.

2.5.4. Electromechanical characterization

The test coupons were prepared by transferring the PGS to the test phantom so as to mimic a simplified PGS-skin structure. The phantom or surrogate skin was fabricated by spin coating (1200 rpm, 30 s, spin coater model WS-650MZ-23NPPB, Laurell Technologies) stretchable and low modulus (~ 190 kPa) Dragon Skin® (a 1:1 mixture of parts A and B). After being air-dried at room temperature, the phantom skin was removed from the glass substrates. The resulting phantom had an average thickness of ~ 90 μm, which was cut to 50 × 28 mm^2 individual specimens. Then, the PGS was attached onto the phantom skin to form the test specimens. Figures 2.16a and 2.16b illustrate an explosion-view of the laminated test coupon structure and a photograph of an assembled specimen. The inset of Figure 2.16b shows an assembled specimen that collapsed under its own self-weight, further indicating the flexibility of the device.

Before conducting load tests, the nominal resistance of the PGS was first characterized. Here, PGS of different numbers of layers (*i.e.*, 4, 8, 12, 18, and 24 layers) were fabricated. The resistance time histories of the specimens were recorded using a DMM when they remained un-

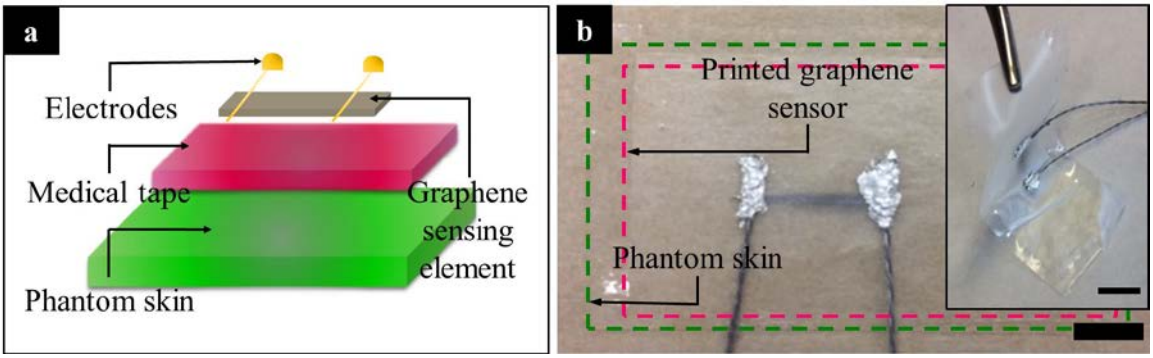

Figure 2.16 (a) An explosion-view of the test coupon structure. (b) An assembled coupon for strain sensing tests. The left inset illustrates a magnified-view of the test coupon structure. The inset illustrates the flexible configuration of the device. All scale bars, 10 mm.

deformed and at room temperature. Then, an electromechanical load frame (TestResources 150R) was employed for applying tensile cyclic loads to the specimens. During the load tests, the resistance time history of the PGS specimen was measured using a Keysight 34465A DMM interfaced to the Keysight *BenchVue* program for data acquisition and storage. Here, multiple tensile cyclic strain patterns to different peak strains (*i.e.*, 0.5%, 1%, 2%, 4%, 8%, 10%, and 20%) were applied at a constant loading frequency of 0.5 Hz. In addition, the long-term strain sensing response was investigated by subjecting the PGS specimen to 2000-cycle loads with a peak strain of 1% at 0.5 Hz loading frequency.

Figure 2.17 shows the average nominal resistance of the PGS fabricated using different numbers of printed layers. To render the GNS-based pattern electrically conductive, at least 4 printed layers were required. In addition, as more layers were deposited (*i.e.*, incorporating more GNS), the printed trace became more conductive.

Figure 2.18a shows the stress-strain curves of the pristine medical tape and the PGS. It can

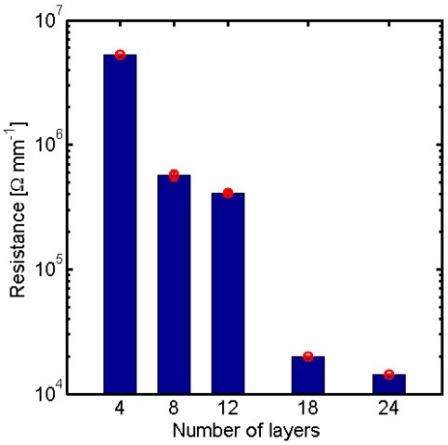

Figure 2.17 The nominal resistance of the PGS fabricated using different numbers of printed layers.

be seen that printing the GNS-based patterns onto medical tape barely affected the mechanical properties of the pristine substrate. Figure 2.18b exhibits the undeformed and deformed configurations of a specimen mounted in the load frame. In general, the printed GNS sensing element deformed conformably with the substrate without any visible delamination. Figure 2.18c illustrates a representative normalized change in resistance (ΔR_n) time history response of a PGS-phantom skin when subjected to different applied strain patterns. The inset of Figure 2.18c shows the specimen's response at low strains. The sensor's resistance increased in tandem with increasingly applied tensile strains, and the opposite was true during unloading, regardless of the magnitudes of peak strain applied. Its piezoresistive response is likely mainly due to deformation-induced changes in the conformation of the electrically conductive GNS network (*i.e.*, contact resistance). Although the piezoresistivity of individual GNS was also reported [138, 139], in this study, GNS was assumed to be too rigid to be deformed by the interactions within the binder-free GNS network. Therefore, strain-induced changes in GNS-to-GNS junctions most likely dominated the piezoresistivity of the sensing element. In particular, it is hypothesized that GNS could undergo rigid-body motions within its compliant matrix as strain was applied to deform the substrate, thereby disrupting graphene-to-graphene junctions and the number of conductive pathways that exists within the film. However, the GNS network was able to restore back to its initial configuration upon strain release, thereby allowing resistance to decrease and return to its nominal resistance when strain was completely removed [140, 141].

In Figure 2.18c, ΔR_n is plotted as a function of ε, and each set of raw data is then fitted with a linear least-squares regression line. The slope of the best-fit line equates to *GF*. The inset of Figure 2.18c shows a detailed view of the PGS' response when it was subjected to low levels of strains. The PGS exhibited ubiquitous linear strain sensing response and an average *GF* of 21 for

applied strains up to ~ 10% (where the coefficient of determination or R^2 was 0.96), which is a preferable attribute. It can also be observed in Figure 2.18d that the PGS was characterized by bilinear strain sensitivity when strained beyond 10%. *GF* was ~ 142 when applied strain was between 10% and 20%. The PGS developed in this study exhibited significantly higher strain sensitivities than previously reported sensing skins, including silicon-based patterns (*GF* was ~5 [142] and ~1.6 [143]) and CVD-grown graphene patterns (*GF* was ~ 2.1 [144]). The observed nonlinearity of strain sensing response could be due to abrupt changes in the GNS network topology. To be specific, the microstructure of the GNS network might change from a "homogeneous network" to an "inhomogeneous network" when applied strain was increased beyond a certain threshold (*i.e.*, ~ 10% in this case) [76, 145]. The nonlinear electromechanical performance was commonly reported for resistive strain sensors of high sensitivity but are relatively limited in stretch-ability [76, 145-147]. Future studies will focus on characterizing and improving the linearity of the sensing performance, especially under large strains. In addition, sensor durability was investigated by applying 1000 cycles of tensile strains, and a representative ΔR_n time history plot is shown in Figure 2.18e. The inset of Figure 2.18e examines a magnified view of the response within a 50-s time window, which clearly shows the sensor's repeatable and stable electromechanical response. In addition, the repeatable response indicates that the PGS was

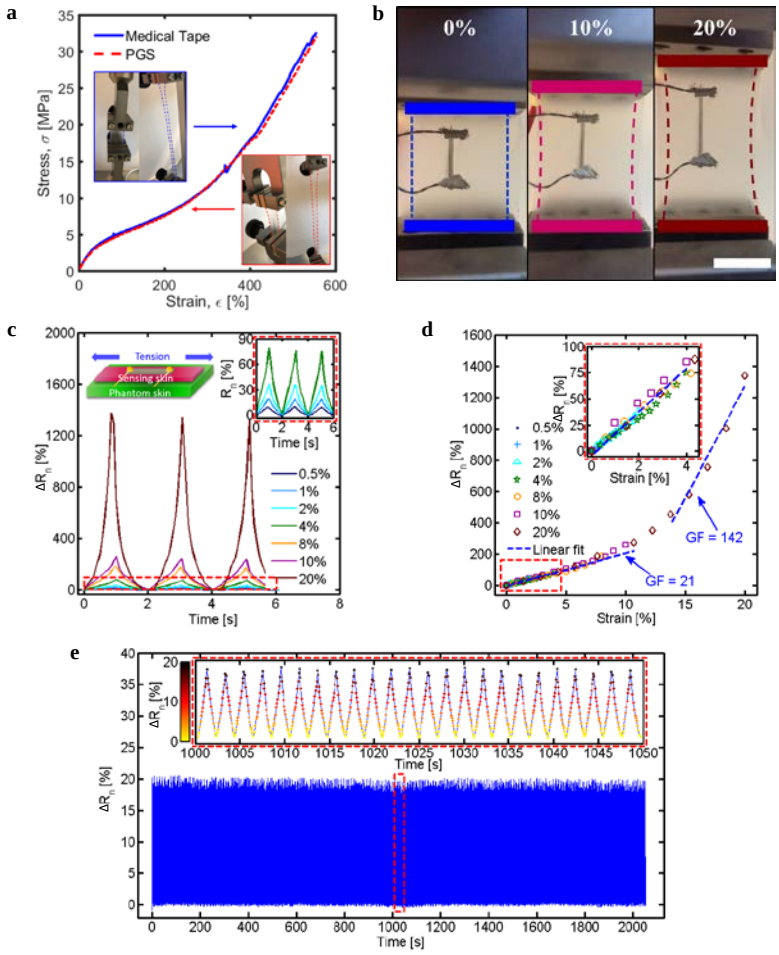

Figure 2.18 (a) The stress-strain curves of the medical tape (highlighted in blue) and the PGS (highlighted in red). (b) Images of a specimen subjected to 0 %, 10 %, and 20 % applied strains in the load frame. The dashed lines depict the edges of the PGS. Scale bar, 10 mm. (c) Representative ΔR_n time histories of a specimen subjected to tensile cyclic strains of different peak magnitudes. The inset confirms the sensor's linear response at low-strains. (d) The ΔR_n data extracted from (c) plotted as a function of applied strains, and fitted by least-squares regression lines. The inset magnifies the region highlighted in the dashed box. (e) The ΔR_n time history corresponding to cyclic load tests to 1 % peak strain at 0.5 Hz loading frequency. The inset shows the ΔR_n data included in the 50 s time window.

mechanically intact throughout all the load tests. Overall, the PGS is characterized by repeatable, reversible, and stable strain sensing performance and without noticeable fatigue degradation.

2.6. Summary and Conclusions

In this chapter, the CNT- and GNS-based nanocomposites have been fabricated with three different bottom-up techniques, depending on manufacturing requirements. To be specific, spray coating is advantageous for large-scale implementation, while screen printing can be used to fabricate relatively large-scale patterns. On the other hand, micro-patterning is desirable for creating high-precision (*i.e.*, microscale), small-scale patterns. The manufacturing procedures have been designed and optimized for specific material components to obtain consistent qualities of resulting nanocomposites. By investigating their microstructures with microscopy imaging and Raman spectrum analyses, it was found that CNTs and GNS could be uniformly dispersed in the polymeric matrices of the nanocomposites, indicating the effectiveness of the proposed manufacturing methods.

Upon fabricating the nanocomposite thin films, their strain sensing properties were characterized by conducting tensile cyclic load tests. Here, the thin films were subjected to different tensile strain patterns, while their electrical resistance changes were measured and recorded simultaneously. It was found that the fabricated nanocomposites were all responsive to the applied strains, and their resistance changed in accordance with the strain patterns, which validated that these nanocomposites were piezoresistive and could be potentially applied as strain sensors. In general, it was hypothesized that the distributed CNTs and GNS could establish electrical pathways in the nanocomposites that were susceptible to deformation-induced disturbances. Increasingly applied tensile strains would reduce the number of electrically conducting pathways, which results in an increase in bulk resistance. On the other hand, the electrical pathways could restore their initial configurations once the strains were released, provided that the thin films were strained in their elastic domain.

As compared to commercial strain gages, the designed nanocomposites exhibited superior mechanical and sensing properties. In particular, since the CNTs and GNS were densely distributed in the nanocomposites, every location on the thin films were piezoresistive and could be potentially utilized as densely distributed strain sensors. This feature and the ability to perform spatial sensing will be discussed in Chapter 5. In addition, the strain sensitivity of nanocomposites could be designed significantly higher than of commercial strain gages (*e.g.*, screen-printed GNS sensors were ~ 37 times more sensitive when $\varepsilon \geq 10\%$, and micro-patterned GNS sensors were ~ 10 times more sensitive when $\varepsilon \leq 10\%$). The highly strain-sensitive nanocomposites are promising to not only enhance the signal-to-noise ratio and data accuracy but could also capture otherwise undetectable structural deformations. In addition, it should be noted that the sensing performances of the nanocomposite thin films were characterized via uniaxial load tests, and future work is needed to characterize the Poisson's effect induced-transverse strain sensitivity [148, 149]. Thus, in the applications demonstrated in the remainder of this dissertation employed sensing films with a biased longitudinal gage length which could effectively reduce transverse strain sensitivity and more accurately measure the uniaxial longitudinal strains [148]. However, for practical applications that generally require measuring complex stress/strain fields with unknown principal stress/strain directions, it is essential to further characterize the transverse sensitivity of the nanocomposite thin films to calibrate measurements and obtain the absolute strain values.

Chapter 2, in part, is a reprint of the material as it appears in Spray-coated Carbon Nanotube-Latex Strain Sensors, L. Wang and K. J. Loh, 2015; Micro-Patterned Graphene Sensing Skins for Human Physiological Monitoring, L. Wang, K. J. Loh, W.-H. Chiang, and K. Manna, 2018; and Printed Strain Sensors Using Graphene Nanosheets Prepared by Water-Assisted Liquid

Phase Exfoliation, K. Manna, L. Wang, K. J. Loh, and W.-H. Chiang, 2019. The dissertation author was the primary investigator and author of these papers.

Chapter 3. Topological Design and Characterization of Piezoresistive Nanocomposites

3.1. Introduction

The previous chapter introduced three different manufacturing techniques for fabricating nanocomposites, and their piezoresistivity was validated through extensive electromechanical characterization tests. The high strain-sensing performance of the designed nanocomposites render them promising to be utilized as strain transducers. In addition, it should be noted that the manufacturing procedures were empirically optimized based on the corresponding material systems for obtaining the optimal fabrication efficiency and piezoresistive properties.

On the other hand, when it comes to other sensing applications, the fact that a transducer would change its output response due to applied strains can be highly undesirable and limit their use. For example, stretchable conductors are promising candidates for flexible displays [150], flexible energy harvesting and storage [151], and artificial skins [145, 152], among others. It remains challenging to develop highly flexible conductive materials whose electrical conductivity maintains constant even during large deformations (*e.g.*, stretching, bending, and twisting). In

addition, for the next-generation of wearable electronics, it is essential to develop flexible sensing materials that provide stable electrical outputs related to multiple parameters (*e.g.*, temperature and pH) without being affected by applied strains and loads [153, 154]. Therefore, there remains a need to effectively design the piezoresistive properties of functional materials for different types of target applications. To be specific, these functional materials may require enhanced piezoresistivity for operation as a strain sensor or, in a different scenario, exhibit suppressed piezoresistivity to prevent the strain- or load-induced effects.

To develop the functional nanocomposites of desirable piezoresistive performance, most of the reported work to date focused on engineering and enhancing the material aspect of the nanocomposites, such as the nanostructures of the nanofillers [153, 155-157], nanofiller loading or concentrations [119], and morphologies of the polymetric matrices [145, 158], to name a few. Although these strategies were successful at adjusting nanocomposite piezoresistivity, the processes were mostly empirical and inefficient, especially considering the complex effects of the resulting material systems on global piezoresistive behavior. More importantly, the potential multifunctionality of the nanocomposites were hardly leveraged given that each material system had to be developed for a specific target application. Thus, it is essential to develop a more universal material engineering methodology that is not only broadly applicable to different nanocomposites but also capable of achieving a wide range of desired piezoresistivity depending on the application needs.

Therefore, this chapter proposes a topological design-based approach to strategically control the strain sensing performance of nanocomposites. By building upon the fabricated CNT- and GNS-based nanocomposite thin films described in Chapter 2, this study aims to manipulate the bulk strain sensitivity of the nanocomposites by controlling the uniaxial-tension-induced stress

field distribution in the thin films. Particularly, to alter and control the stress distribution in the material system, Section 3.2 proposes different topological designs, including hierarchical inhomogeneous structures and Kirigami structures for concentrating and releasing stresses, respectively. To arrive at different material topologies, finite element (FE) analysis was conducted to investigate the effects of different topologies on their corresponding stress field distributions. Based on the numerical simulation results, patterned thin films were reproduced experimentally by screen-printing GNS-EC (Section 3.3.1) and spray-coating CNT-latex nanocomposite (Section 3.3.2) thin films onto laser-patterned PET substrates, respectively. They were then subjected to load tests for characterizing their strain sensitivity and for assessing the effectiveness of topological design on controlling bulk film strain sensitivity. Furthermore, to numerically investigate the topological effects on the nanocomposites' piezoresistivity, Sections 3.4.1 and 3.4.2 employed linear and nonlinear material models to simulate the electromechanical performance of the patterned thin films, respectively.

3.2. Topological Designs

3.2.1. Pattern designs and fabrication

Many thin film strain sensors are based on a continuous, rectangular geometry, which was employed as the Non-Patterned control set in this study. Since the aim of this study was to manipulate thin film strain sensing properties when the material system remains unchanged, different topological designs were proposed. By varying thin film topologies, the tension-induced stress and strain distributions in the patterned material system could be altered and controlled. Here, two main categories of different topologies were designed, namely, stress concentrating and stress releasing topologies, which are presented in Figures 3.1 and 3.2, respectively.

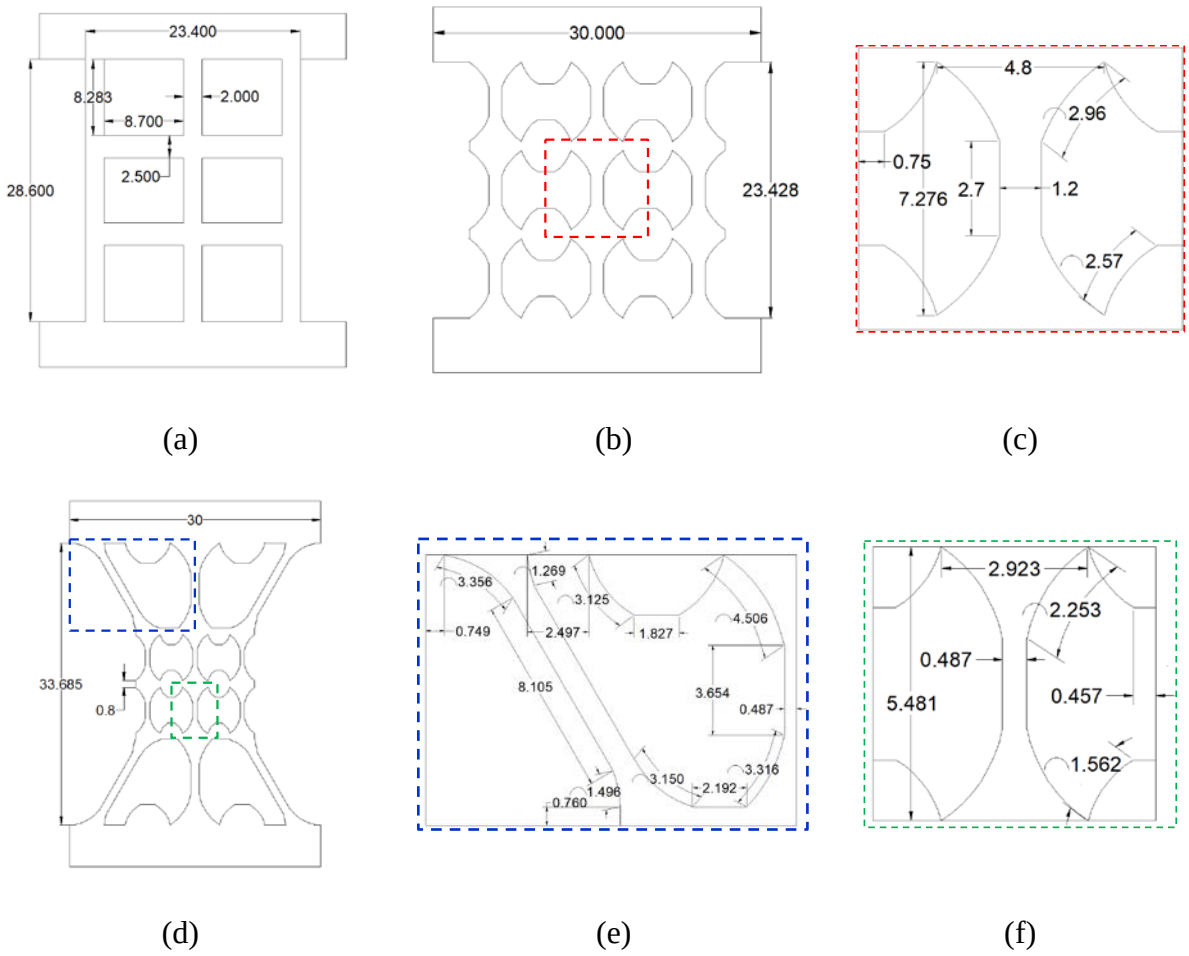

Figure 3.1 The AutoCAD drawings detail the design of the (a) Grid, (b) Dog-Bone Grid (whose detailed dimensions shown in (c)), and (d) Hierarchical Dog-Bone topologies (whose detailed dimensions shown in (e-f)).

First, the stress concentrating designs started with the creation of a grid-like pattern in lieu of a continuous material system (*i.e.*, the Grid as shown in Figure 3.1a). The introduction of stress concentrations was based on the inhomogeneity of stress distribution in the commonly used dog-bone test specimen. It is well-known that a dog-bone shaped structure pulled in tension would result in concentrated stresses and strains in its tapered center region. Thus, the vertical elements of the grid design in Figure 3.1a were substituted with dog-bone elements to purposely introduce inhomogeneity to the structure (*i.e.*, considering that tension is applied along the vertical direction),

as shown in Figure 3.1b (*i.e.*, the Dog-Bone). Figure 3.1c illustrates the detailed dimensions of the dog-bone unit. In addition, the horizontal elements were replaced with an inverse dog-bone shape to combat Poisson's effect. To further enhance stress concentrations, a hierarchical design was employed, where the shape of the entire grid was modeled after a dog-bone structure (Figure 3.1d). This design also entailed the incorporation of smaller dog-bone units as the vertical elements, as is shown in Figure 3.1d; hence, this topology design is referred to as the Hierarchical Dog-Bone. Figures 3.1e and 3.1f detail the dimensions of highlighted components of the hierarchical design.

On the other hand, the stress releasing topology designs were inspired by a Japanese artform called Kirigami, which is a paper cutting technique. The Kirigami-based structure allows for enhanced elastic softening and large deformations of an otherwise rigid or non-stretchable substrate material [159]. Figure 3.2a shows the Kirigami design, which includes a periodic array of horizontal cuts (Figure 3.2b) that releases stresses when the entire structure is subjected to vertically applied tension. In addition, this study also introduced a Modified Kirigami structure (Figure 3.2b), which has additional curved corner cuts on both ends of the horizontal cuts (Figure 3.2d) so as to further release the stress. In this study, consistent fabrication of all topology designs was performed by laser-cutting PET substrates (thickness: ~ 100 μm) using a 40 W CO_2 benchtop laser cutter (Orion MotorTech). Digital AutoCAD drawings were uploaded, and the laser-cutter faithfully reproduced these patterns in the PET.

3.2.2. Numerical analysis of stress field

To validate that the proposed topological designs could effectively concentrate or release tension-induced stresses in the films, FE modeling using the Solid Mechanics Module of

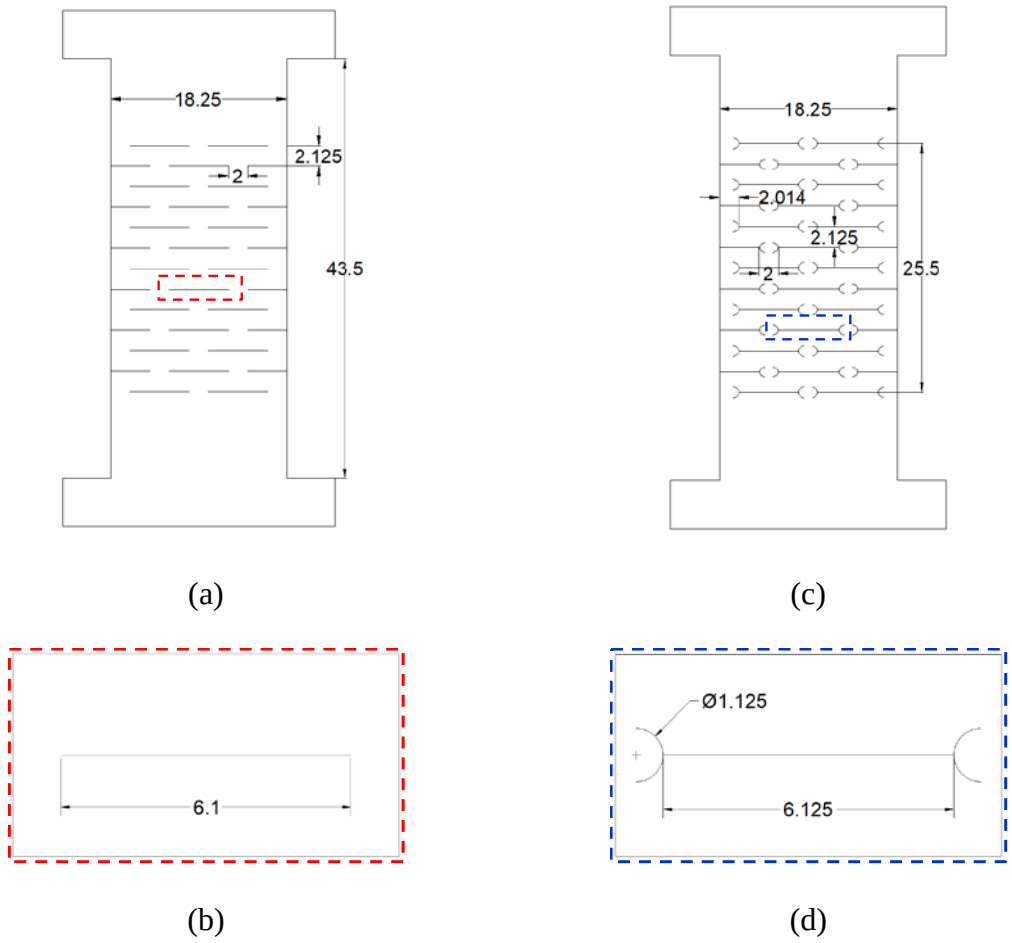

Figure 3.2 (a) The Kirigami and (b) the length of the Kirigami cut is shown. (c) The Modified Kirigami design and (d) the zoomed-in view of the periodic unit highlighted shows the additional stress and strain releasing cuts introduced.

COMSOL Multiphysics was performed. The AutoCAD-based topological designs were imported to COMSOL to build the model geometry; thickness was manually assigned to be 1 mm. The material's mechanical properties were assumed to be dominated by the PET substrate (i.e., Young's modulus: 3.5 GPa; Poisson's ratio: 0.39; density: 1,300 kg m^{-3}). One end of the material model was fixed, while the other end was assigned a 1% tensile strain applied along the y-axis or vertical direction. It should be noted that material performance was assumed to be in the elastic domain.

Figure 3.3 shows the results from FE analysis of the von Mises stress fields in thin films of different topologies when subjected to a 1% tensile strain applied in the vertical direction. Figures 3.3a to 3.3d indicate that stresses were concentrated in the inhomogeneous vertical elements, and the overall magnitude of stress (in the vertical elements of the dog-bone shape patterns) was increased due to inhomogeneity of the pattern. In addition, the Hierarchical Dog-Bone (Figure 3.3d) possessed the most dominant stress concentrations, as well as the highest stress magnitudes in the corresponding inhomogeneous elements. In other words, stress concentrations could be achieved by introducing inhomogeneity in the material structures, and such stress concentrating effect could be enhanced using hierarchical designs.

On the contrary, Kirigami structures were expected to relieve stress concentrations in the material systems. Figures 3.3d and 3.3e show that the stress distributions in the Kirigami and Modified Kirigami designs, respectively. One can see that the stress magnitudes in these structures were significantly lower than the Non-Patterned control set, as well as versus those of the stress-concentrating topologies. In particular, the Modified Kirigami design (Figure 3.3e) was characterized by an even lower stress distribution than the conventional Kirigami structure in Figures 3.3d, which was achieved by purposely introducing additional corner cuts at the ends of the horizontal cuts. Therefore, the FE modeling results indicated that the designed hierarchical inhomogeneous topologies led to enhanced stress concentrations, whereas cuts in the film or Kirigami-based topologies effectively reduced stress distribution and stress concentrations.

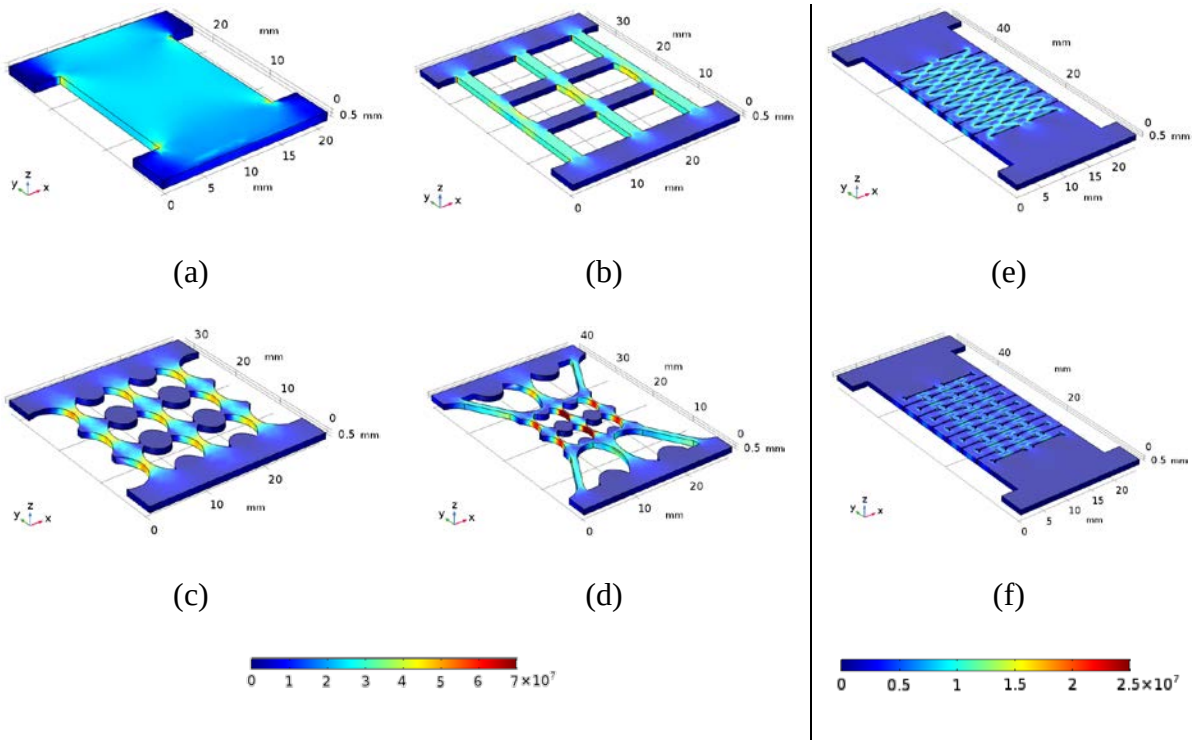

Figure 3.3 FE analyses of the von Mises stress field distributions in the (a) Non-Patterned, (b) Grid, (c) Dog-Bone Grid, (d) Hierarchical Dog-Bone, (e) Kirigami structure, and (f) the Modified Kirigami structure are shown.

3.3. Strain Sensing Characterization of Patterned Nanocomposite Thin Films

3.3.1. Patterned graphene-based nanocomposites

To experimentally investigate the effects of different topological designs on the piezoresistivity of the nanocomposite thin films, two different nanocomposite material systems, including GNS- EC and CNT-latex, were fabricated and tested in this study. First, the GNS-EC nanocomposite thin films were fabricated by screen-printing the vicious GNS-EC ethanol solution onto PET substrates, which were pre-patterned into the aforementioned topologies. The detailed screen-printing procedures were described in Chapter 2. After the coated solution was air-dried, colloidal silver paste and copper tape electrodes were established at the two ends of each film for two-point probe electrical resistance measurements. Then, the strain sensing response of the

patterned nanocomposite thin films was experimentally characterized by conducting load tests using a Test Resources 150R load frame. Here, each specimen was subjected to uniaxial tensile cyclic strains (load rate: 10%/min; peak strain: 1%), while a Keysight 34465A DMM simultaneously measured the bulk film resistance at a sampling rate of 2 Hz. Data was recorded using a Keysight *BenchVue* software.

Figure 3.4 shows the representative ΔR_n (Equation 2.1) time histories of the control set and patterned thin films when they were subjected to tensile cyclic strains. Among the different topologies, it can be seen that the ΔR_n time histories of the Non-Patterned (control set), Grid, Dog-Bone Grid, and Hierarchical Dog-Bone followed closely with the applied tensile cyclic strain pattern in a stable and repeatable manner. In addition, the thin films patterned with stress-concentrating designs exhibited larger normalized changes in resistance (*i.e.*, were more sensitive to strains) than the homogeneous control set.

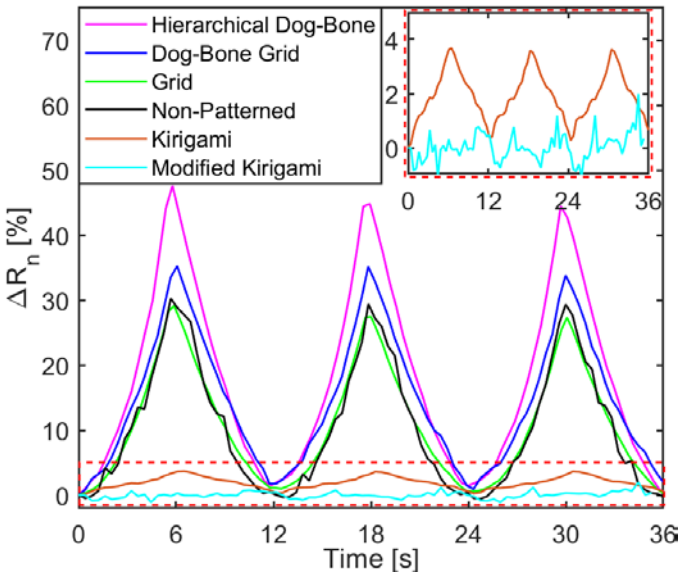

Figure 3.4 Representative ΔR_n time histories of the different patterned GNS-EC specimens subjected to the same tensile cyclic strain pattern are overlaid.

To better compare the strain sensitivities or *GF*s of the nanocomposite thin films of different topologies, Figure 3.5 plots ΔR_n as a function of applied strains ($\Delta\varepsilon$). Although the strain sensing response of the grid structures were polynomial, as is shown in Figure 3.5, linear least-squares best-fit lines were fitted to the data corresponding to ≥ 0.3% applied strains. Then, the slopes of the fitted linear lines were extracted to estimate thin film *GF*s (according to Equation 2.2). It can be seen from Figure 3.5 that the linear approximation was able to sufficiently characterize the changing trends of ΔR_n for the various nanocomposite topologies tested. To be specific, the *GF*s of the Grid, Dog-Bone Grid, and Hierarchical Dog-Bone topologies were calculated to be ~ 38, 41, and 60, respectively. This indicated that the bulk film *GF* of the GNS-EC strain sensors could be effectively increased by leveraging the inhomogeneous topology-induced stress concentrations in the material system. In addition, higher levels of hierarchical inhomogeneity led to more significant enhancements in strain sensitivity. These results imply that

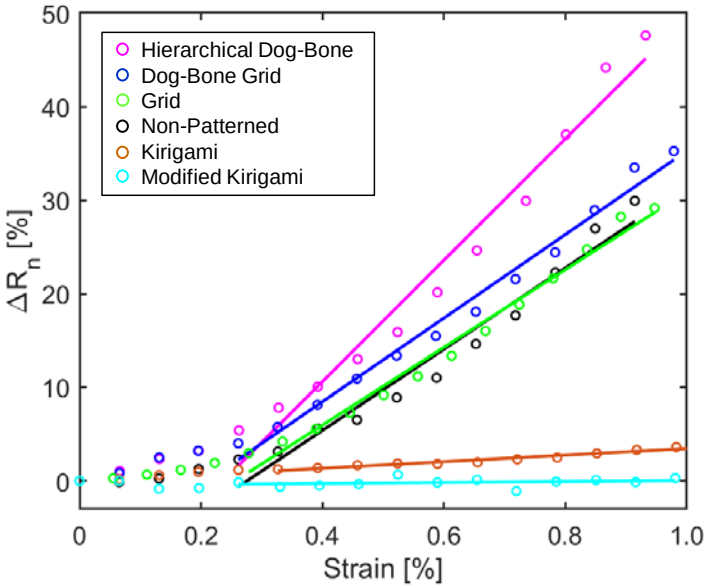

Figure 3.5 The ΔR_n of the GNS-EC specimens are plotted as functions of the increasingly applied strain during one loading cycle. Linear least-squares regression lines are fitted to data where strain ≥ 0.3%.

high-sensitivity sensors could be developed solely based on designing the material's topology. It was hypothesized that the piezoresistivity of GNS-EC thin films mainly stem from deformation- and strain-induced disturbances to the percolated and conductive GNS network of the nanocomposite. In particular, applied tensile strains would induce separations between individual or small bundles of GNS to decrease the total number of GNS-to-GNS contacts, thereby reducing the number of overall electrical current conducting pathways in the nanocomposites and thus leading to higher bulk film resistance. Based on this hypothesis, this study focused on manipulating the stress distribution in nanocomposite thin films and used this as a mechanism for controlling their bulk film strain sensitivity. For instance, when higher strain sensitivity is desired, significant disturbances in the GNS-conducting pathways could be achieved by purposefully incorporating stress and strain concentrations in the nanocomposite.

On the other hand, based on the same hypothesis, the Kirigami-based topologies were designed to release stress/strain concentrations in the nanocomposites so as to reduce disturbances to the percolated GNS networks and to minimize strain sensitivity. From Figures 3.4 and 3.5, one can observe that the Kirigami-based nanocomposite specimens exhibited significantly lower strain sensing response. The suppressed strain sensitivity was especially obvious for the Modified Kirigami topology sample set, whose *GF* was found to be ~ 0.48 (Figure 3.5). These results suggested that the global strain sensing performance of piezoresistive nanocomposite thin films could be efficiently suppressed by releasing stresses in the material system and by preserving their nanostructure during large deformations. In other words, the stress releasing topologies (*i.e.*, Kirigami-based structures in this study) are promising for decoupling sensing signals induced by

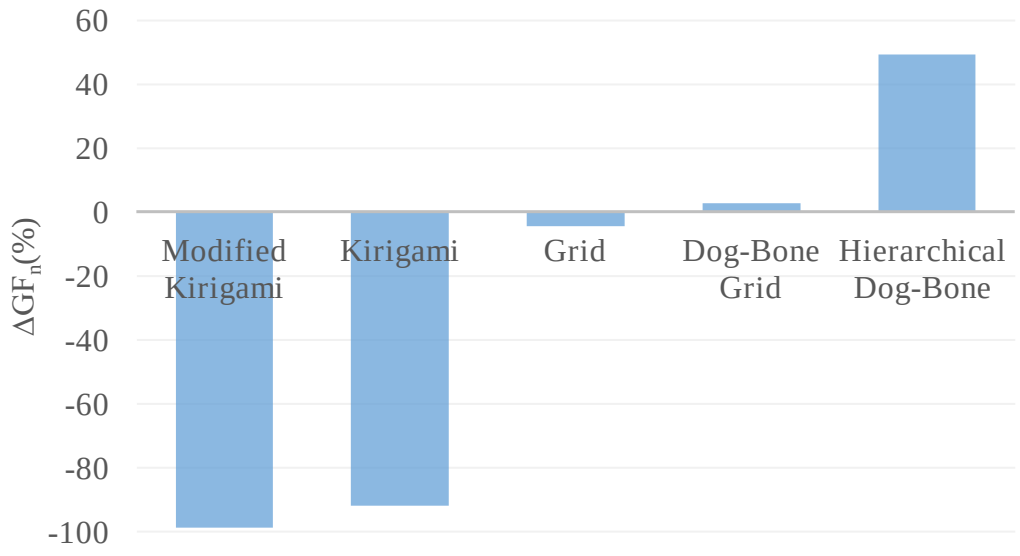

Figure 3.6 The ΔGF_n obtained by different topological designs as compared to the Non-Patterned control set.

strains/deformation from the primary desirable measurand (*e.g.*, temperature-induced resistance changes).

Overall, Figure 3.6 summarizes the normalized difference in *GF*s ($\Delta GF_n = (GF_i - GF_0)/GF_0$) obtained by the proposed topological designs as compared to the Non-Patterned control set. Here, GF_i represents the *GF* values of each pattern, while GF_0 is that of the Non-Patterned sample set (~ 40). It was found that, based on the same GNS-EC material system, a topological design strategy could achieve a remarkably expanded spectrum (− 99% to + 50%) of strain sensing performance. This indicates that the proposed topological design approach could be potentially leveraged to strategically manipulate the bulk material piezoresistive property for target multifunctional performance in a predictable and controllable manner.

3.3.2. Patterned carbon nanotubes-based nanocomposites

To further validate the effectiveness and applicability of this topological design strategy, this study also experimentally characterized the strain sensing performance of CNT-based nanocomposite thin films. In particular, the CNT-latex thin films were patterned by spray-coating the CNT-based ink onto the pre-patterned PET substrates, following the procedures introduced in Chapter 2. Similar to Section 3.3.1, load tests were performed on the fabricated CNT-based specimens to investigate their strain sensing response. Figure 3.7 shows representative ΔR_n time histories of the control and patterned thin films when they were subjected to tensile cyclic strains. In addition, *GF*s of different thin film patterns were evaluated in Figure 3.8. Based on the approximate linear regression best-fit lines in Figure 3.8, the *GF*s of the Modified Kirigami, Kirigami, Grid, Dog-Bone Grid, and Hierarchical Dog-Bone topologies were calculated to be

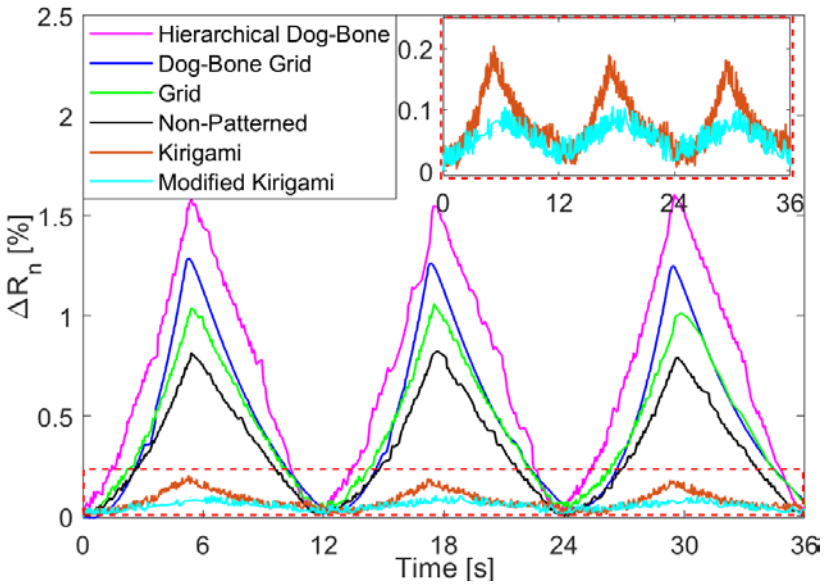

Figure 3.7 Representative ΔR_n time histories of the different patterned CNT-latex specimens subjected to the same tensile cyclic strain pattern are overlaid.

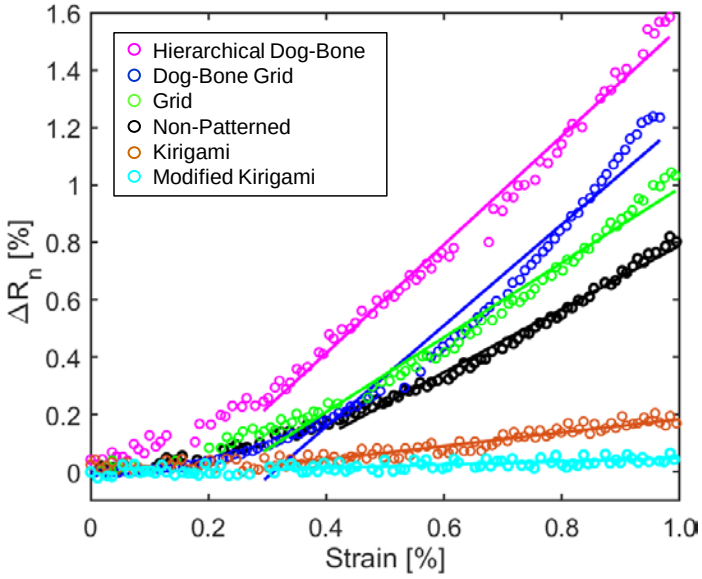

Figure 3.8 The ΔR_n of the CNT-latex specimens are plotted as functions of the increasingly applied strain during one loading cycle. Linear least-squares regression lines are fitted to data where strain ≥ 0.3%.

about 0.06, 0.2, 1.3, 1.7, and 1.9, respectively. Furthermore, Figure 3.9 summarizes the ΔGF_n obtained from different topologies as compared to that of the Non-Patterned control set (~ 1.1). One can observe that the stress-concentrating topologies enhanced the strain sensitivity of the CNT-latex nanocomposites by ~ 70% (*i.e.*, Hierarchical Dog-Bone), while the stress-releasing structures suppressed piezoresistivity by ~ 95% (*i.e.*, Modified Kirigami). These results further demonstrated that the topological design-based approach could consistently manipulate different piezoresistive nanocomposite material systems, paving ways for next-generation multifunctional materials development and strategies for engineering specific material properties.

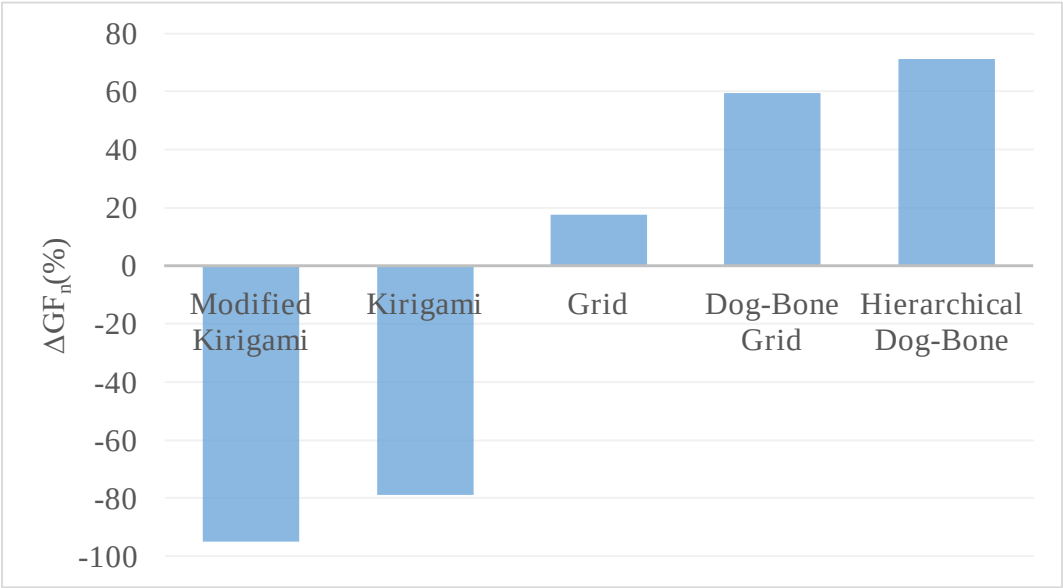

Figure 3.9 The ΔGF_n obtained by different topological designs as compared to the Non-Patterned control set.

3.4. Numerical Analysis of Electromechanical Response

3.4.1. Linear piezoresistive material models

To further investigate the topological effects on the strain sensing performance of nanocomposite thin films, numerical analysis of their electromechanical response was first conducted based on a calibrated linear piezoresistive material model. Here, the simulation was performed in COMSOL by coupling the Solid Mechanics Module with the Electric Currents Module. Initially, the nanocomposite thin films were simulated by modifying the material properties of the COMSOL built-in material model for piezoresistive p-doped silicon. Particularly, the piezoresistive coupling matrix (Π) was calibrated to fit the experimental measurements for the control set of Non-Patterned specimens, including both GNS-EC and CNT-latex nanocomposites for the corresponding material systems. In general, for piezoresistors, the current electric field strength (E) can be expressed as follows:

$$E = \rho \cdot I + \Delta\rho \cdot I \tag{3.1}$$

where I represents the current, ρ is the original resistivity of the material, and $\Delta\rho$ is the change in resistivity resulting from mechanical excitations (*e.g.*, applied loads). In other words, $\Delta\rho$ is related to mechanical stress (σ), which can be expressed in the form of constitutive relationship, as follows [160]:

$$\Delta\rho = \Pi \cdot \sigma \tag{3.2}$$

In the context of three-dimensional (3D) modeling of cubic symmetry materials with isotropic conductivity (*e.g.*, silicone), Equation 3.2 becomes:

$$\begin{bmatrix} \Delta\rho_{xx} \\ \Delta\rho_{yy} \\ \Delta\rho_{zz} \\ \Delta\rho_{yz} \\ \Delta\rho_{xz} \\ \Delta\rho_{xy} \end{bmatrix} = \begin{bmatrix} \pi_{11} & \pi_{12} & \pi_{12} & 0 & 0 & 0 \\ \pi_{12} & \pi_{11} & \pi_{12} & 0 & 0 & 0 \\ \pi_{12} & \pi_{12} & \pi_{11} & 0 & 0 & 0 \\ 0 & 0 & 0 & \pi_{44} & 0 & 0 \\ 0 & 0 & 0 & 0 & \pi_{44} & 0 \\ 0 & 0 & 0 & 0 & 0 & \pi_{44} \end{bmatrix} \cdot \rho \begin{bmatrix} \sigma_{xx} \\ \sigma_{yy} \\ \sigma_{zz} \\ \sigma_{yz} \\ \sigma_{xz} \\ \sigma_{xy} \end{bmatrix} \tag{3.3}$$

where π_{ij} are the elements of the piezoresistive coupling matrix Π and are defined as piezoresistive coefficients [160-162]. Assuming the nanocomposites also possess similar isotropic electrical properties as silicone, the piezoresistive coefficients of the nanocomposite material models were first linearly calibrated based on the experimentally measured strain response (*i.e.*, ΔR_n time histories) of the Non-Patterned sample set. Then, the calibrated material models were used to simulate the electromechanical responses of different topological designs, whose results were compared with the corresponding experimental measurements. Here, the fixed-end of each material model (Section 3.2.2) was assigned as electrical ground, while the other end was set as the terminal. A DC of 2 mA was then injected between the ground and terminal, which is similar to the experimental resistance measurement mode of the DMM as mentioned earlier.

First, for the GNS-EC nanocomposite thin films, Figure 3.10a shows the spatial distribution of electric potential, as well as isosurfaces of electric potential in the Non-Patterned material model, when it was subjected to 1% tensile strain applied in the direction of the y-axis. It can be seen that its electric potential is uniformly distributed in the material except for regions near the boundaries (due to ground and terminal effects), which was consistent with the assumption of homogeneous material properties. In addition, the strain response of the material models could be obtained by probing the terminal electric potential for each deformation case. In Figure 3.10b, the normalized change in electric potential ($\Delta V_n=\Delta V/V_0$) of the calibrated Non-Patterned control set was plotted as a function of applied strains and overlaid with the corresponding experimentally measured ΔR_n results. Here, ΔV and V_0 represent the change in the terminal electric potential and initial (unstrained) terminal electric potential, respectively. It can be seen that the simulated material possessed similar strain sensitivity as the actual GNS-EC nanocomposite thin films.

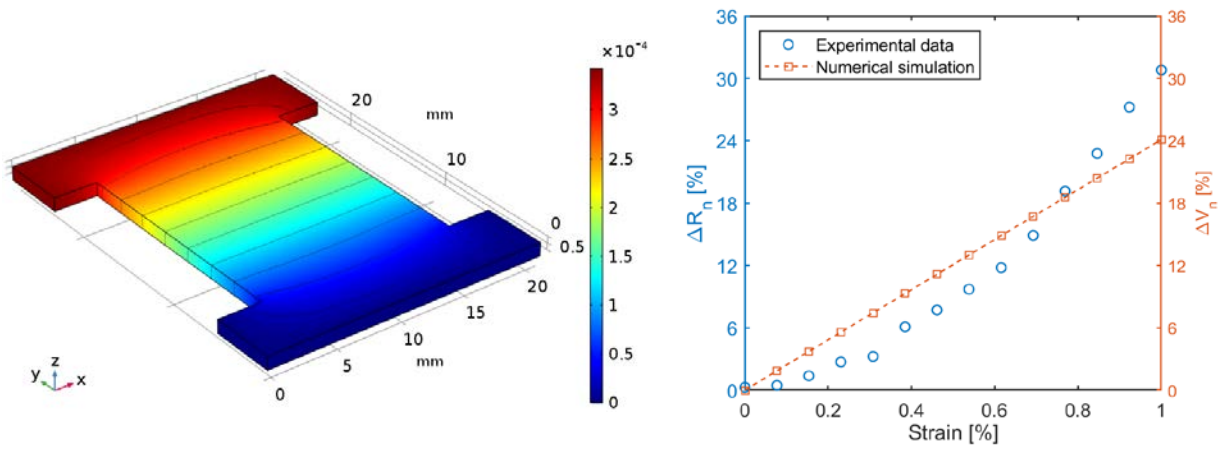

(a) (b)

Figure 3.10 (a) The electrical potential distribution along with the isosurfaces of electric potential in the Non-Patterned material model when subjected to 1% tensile strain is plotted. (b) The FE model was calibrated using experimental results from the Non-Patterned topology, and ΔV_n with respect to applied strains are compared to the experimentally measured ΔR_n values.

However, the experimental measurements exhibited slight nonlinear behavior that could not be simulated using the piezoresistive numerical model. It is hypothesized that the nonlinear strain response potentially resulted from inhomogeneous changes in the nanocomposites' microstructure during applied strains and deformations [76, 145]. Thus, to further enhance the accuracy of the electromechanical simulation, Section 3.4.2 intends to account for potential inhomogeneous material property changes using nonlinear percolated material models.

Nevertheless, the calibrated material model's piezoresistivity was then directly assigned to the different topological models for characterizing their electromechanical performance. Figure 3.11 shows the variations of ΔV_n for different topological material models subjected to increasingly applied tensile strains up to 1%. Similar to the experimental results, one can find that the simulated stress-concentrating topologies were more sensitive to strain, while the stress-releasing ones could decrease strain sensitivity. In the meantime, it should be noted that the linear numerical model underestimated the absolute values of the strain sensing responses for the corresponding specimens.

In addition, this study also implemented the same FE analysis approach to simulate the electromechanical responses of the CNT-latex nanocomposite thin films. Figure 3.12 shows the computed ΔV_n for different topological material models, including the pre-calibrated Non-Patterned control set. The linear piezoresistive model could also simulate the relative change in strain sensitivity introduced by different topological designs. Overall, the linear electromechanical FE analyses successfully demonstrated how thin film topologies would affect bulk film strain sensitivity, and the results were consistent with those observed from the experiments.

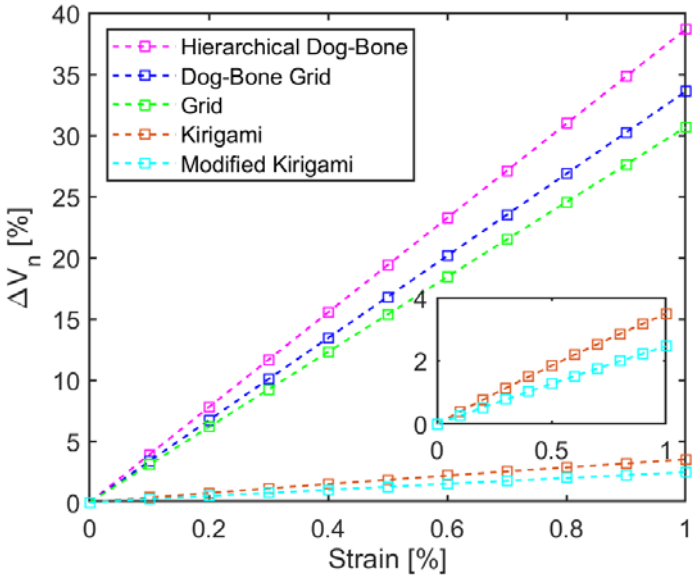

Figure 3.11 The electromechanical responses of different topological material models when they were subjected to up to 1% tensile strain were determined through multi-physics FE modeling. The inset shows a zoomed-in view of the Kirigami-based material models' electromechanical responses.

3.4.2. Percolated inhomogeneous material models

The previous section modeled the nanocomposites using homogeneous piezoresistive material models, which could not simulate the nonlinear behavior observed from experimental data. Thus, this section aims to employ material models with inhomogeneous electrical properties to introduce nonlinearity to the simulated electromechanical response. Here, the nanocomposites were considered as percolated material systems, which include randomly distributed electrical defects (*i.e.*, low electrical conductivity) within the material. It was hypothesized that the experimentally observed piezoresistivity of the nanocomposite thin films mainly stemmed from mechanical loading-induced disturbances to the electrical defects distribution. To be specific, increasingly applied tension could generate more electrical defects in the material system, which would correspondingly increase the bulk electrical resistance of the nanocomposites. In other

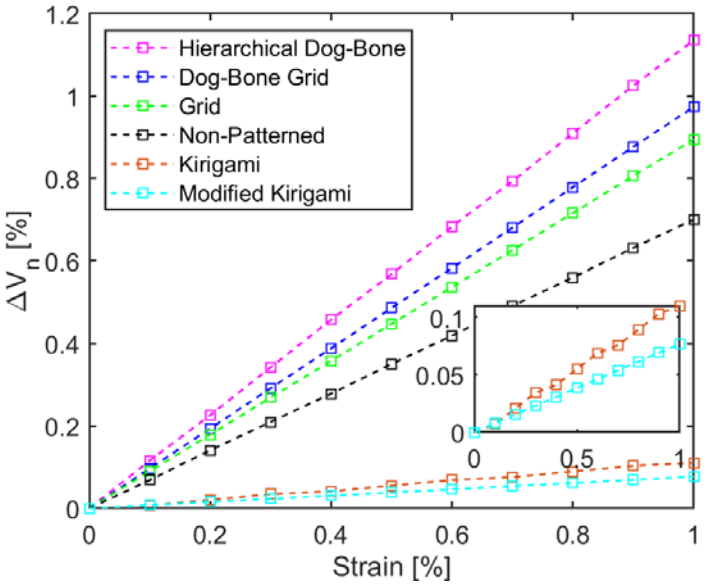

Figure 3.12 The electromechanical responses of different topological material models when they were subjected to up to 1% tensile strain were determined through multi-physics FE modeling. The inset shows a zoomed-in view of the Kirigami-based material models' electromechanical responses.

words, the proposed approach ultimately would generate a material model that possesses randomly distributed inhomogeneous features (*i.e.*, electrical defects), which would propagate according to externally applied mechanical deformations and cause an increase in its electrical resistance.

Based on the aforementioned assumption, in a 3D domain of interest with dimensions of 40 × 40 × 0.1 mm^3 (*i.e.*, slightly larger than the dimensions of the designed topologies), a randomized statistical data set was first generated using a combination of trigonometric functions as follows [163, 164]:

$$f(x,y,z) = \sum_{k=-K}^{K}\sum_{l=-L}^{L}\sum_{m=-M}^{M} a(k,l,m)cos(2N\pi(kx+ly+m(40z))+\varphi(k,l,m)) \quad (3.4)$$

where the slowest oscillation of the cosine waves was defined by $2\pi/2N\pi = 1/N$, which determined the periodicity of the synthesized data. With $N = 25$ in this study, the spatial period length was 40

mm so that the 3D domain of interest could include all the randomly generated dataset without bias. On the other hand, *k*, *l*, and *m* are spatial frequencies that determined the fastest oscillations of the cosine waves, whose maximum values are *K*, *L*, and *M*, respectively. Generally, larger spatial frequencies could improve the spatial resolution of the data, but it would also increase computational cost, especially for 3D cases. In this study, considering the dimensions of the material models, it was set that $K = L = M = 200$ m^{-1}; then the shortest wavelengths in the x, y, and z directions were 0.2 mm. To avoid generating cosine wave functions of biased oscillation directions, *k*, *l*, and *m* were allowed to take on negative values. In addition, $\varphi(k, l, m)$ represents phase angles, which were generated with a uniform distribution that ranged from $-\pi/2$ to $\pi/2$. Furthermore, $a(k, l, m)$ represents oscillation amplitude coefficients, which were determined by:

$$a(k, l, m) = \frac{g(k,l,m)}{(k^2+l^2+m^2)^{\frac{\beta}{2}}} \tag{3.5}$$

where the function $g(k, l, m)$ had a random Gaussian distribution ($g(k, l, m) \sim N(0, 1)$), and β is the spectral exponent to attenuate higher frequencies so as to generate smooth amplitude coefficients [165]. It should be noted that, since the 3D domain is a thin slab (*i.e.*, smaller z-dimensions), the z-coordinate values were scaled up 40 times to include all the dataset. Figure 3.13 shows the synthesized random data distributed in the 3D domain, and Figure 3.13 shows five slices on the y-z plane of the thin slab to expose the data distribution inside of the slab. The randomized dataset was attributed to each patterned material model by truncating it from the same 3D thin slab. At this point, the randomized data were dimensionless and did not represent any physical properties.

Then, to employ the dimensionless synthesized data to represent physical property parameters, one could multiple Equation 3.4 with a corresponding function that holds

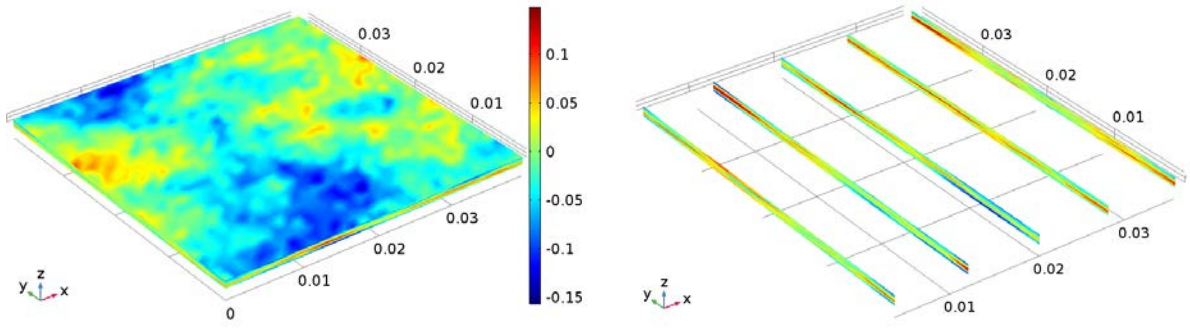

(a) (b)

Figure 3.13 (a) The synthesized randomized data distribution in the thin slab. (b) Randomized data distributions on five slices on the y-z plane within the thin slab.

corresponding physical meaning. To use the randomized statistical data set to represent material electrical conductivity distribution in this work, Equation 3.4 was multiplied by a simplified constant C [S m^{-1}], which ideally should be calibrated with experimental data (*i.e.*, nanocomposite conductivity measurements). However, since this study would mainly evaluate the normalized changes in the terminal electrical potential of the material models under tension, as opposed to absolute values of the electrical potentials, obtaining the exact value of C was not crucial. Furthermore, in order to introduce the aforementioned electrical defects (*i.e.*, inhomogeneous material features), Boolean expression was implemented to convert the randomized conductivity values into binary data distribution, and it can be expressed as follows:

$$\sigma(x, y, z) = C[0.1 + 0.9 \times (|f(x, y, z)| > \tau(x, y, z))] \tag{3.6}$$

where $\sigma(x, y, z)$ represent the conductivity value at coordinate (x, y, z), and $\tau(x, y, z)$ is a pre-defined threshold function. Here, the absolute values of the synthesized randomized data were considered for mathematical simplicity. Equation 3.6 indicates that the electrical conductivity at a specific

location could only be either 0.1*C* or *C*, which represents electrical defects and intact electrical connection, respectively.

In addition, due to the experimentally observed piezoresistive performance of the nanocomposite thin films, their electrical conductivity should to be coupled with their mechanical response when subjected to applied tensions. Based on the previously mentioned hypothesis, electromechanical performance coupling was obtained by establishing the following relationship:

$$\tau(x, y, z) = \phi\left(\frac{\gamma_i(x,y,z)}{\gamma_0}\right) \tag{3.6}$$

where $\gamma_i(x, y, z)$ represents the von Mises stress values at coordinate (x, y, z) when the patterned material model was subjected to uniaxial tensile strains (ranging from 0 to 1%). γ_o is the von Mises stress value at the center location of the Non-Patterned material model under 1% tensile strain (*i.e.*, control stress). Both $\gamma_i(x, y, z)$ and γ_0 could be obtained from FE analyses of the stress distributions performed in Section 3.2 for different material models. In other words, Equation 3.6 evaluates the relative changes in stress distribution introduced by the designed topologies, as compared to the Non-Patterned control set. In addition, the ϕ function could be established by calibrating the percolated material model for the control set with corresponding experimental data. The simplest form of the ϕ function would be a linear function, whose simulated responses for the patterned material models were found to be more accurate than those obtained from nonlinear ϕ functions. This was because the patterned material models featured much higher stresses than the Non-Patterned control set under the same amount of deformations (*i.e.*, large $\frac{\gamma_i(x,y,z)}{\gamma_0}$ values), and the nonlinear ϕ functions performed poorly for extrapolation. Thus, the remainder of this study used a monotonically increasing linear ϕ function. From Equations 3.5 and 3.6, one can estimate that

more concentrated stresses would lead to more electrical defects, whereas released stress would avoid electrical defect formation and propagation, which was consistent with the initial hypothesis.

For the GNS-EC nanocomposite system, similar to homogeneous linear material modeling, the percolated material model was first calibrated based on the Non-Patterned control set. Figure 3.14a shows the spatial distribution of electric potential, overlapped with isosurfaces of electric potential in the Non-Patterned material model, when it was subjected to 1% tensile strain along the y-axis. It can be seen that the electric potential was non-uniformly distributed in the material, indicating that inhomogeneous electrical conductivity distribution was successfully introduced to the material model. In Figure 3.14b, the ΔV_n of the calibrated Non-Patterned control set was plotted as a function of applied strains and overlaid with the corresponding experimentally measured ΔR_n results, as well as the ΔV_n computed using linear piezoresistive model, for comparison purposes. Overall, the inhomogeneous material model not only introduced nonlinearity to the simulated strain response but also more accurately characterized the strain sensitivity of the GNS-EC nanocomposites than the linear model. Furthermore, Figures 3.15a, 3.15b, 3.15c, and 3.15d show the electrical conductivity distributions of the calibrated Non-Patterned material model when it was subjected to 0.5% and 1% tensile strains, respectively. The electrical defects clearly propagated in the material when subjected to larger strains.

Then, the calibrated material model was implemented to simulate the electromechanical responses of the other patterned material models. Figures 3.16 to 3.20 demonstrate the electrical defects distributions and development in the Grid, Dog-Bone Grid, Hierarchical Dog-Bone, Kirigami, and Modified Kirigami material models when they were subjected to 0.2% and 1%

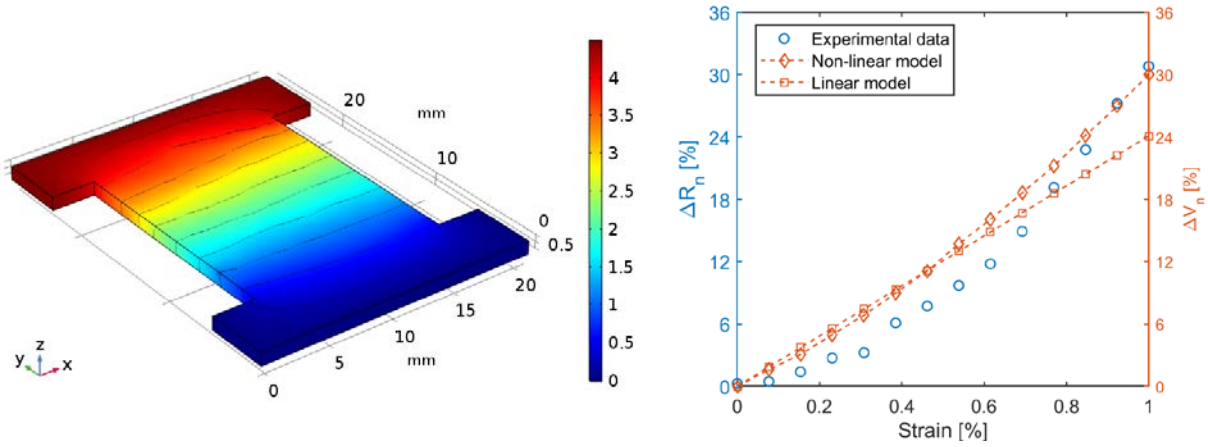

(a) (b)

Figure 3.14 (a) The electrical potential distribution along with the isosurfaces of electric potential in the Non-Patterned material model when subjected to 1% tensile strain is plotted. (b) The non-linear FE model was calibrated using experimental results from the Non-Patterned topology, and ΔV_n with respect to applied strains are compared to the experimentally measured ΔR_n values as well as that obtained from previous linear model.

strains, respectively. From Figures 3.16 to 3.20, it should be mentioned that the electrical defects mainly formed and propagated at the stress-concentrating regions. For the Kirigami topologies, since stress was effectively released from the material, the electrical defects barely developed even at 1% strain. In addition, Figure 3.21 overlays the simulated electromechanical responses of all the patterned material models as functions of applied strains. The proposed inhomogeneous material models agreed well with the experimental strain sensing tests, where both showed that the stress-concentrating topologies could enhance nanocomposites thin film piezoresistivity, while the stress-releasing topologies could significantly suppress their strain sensing responses.

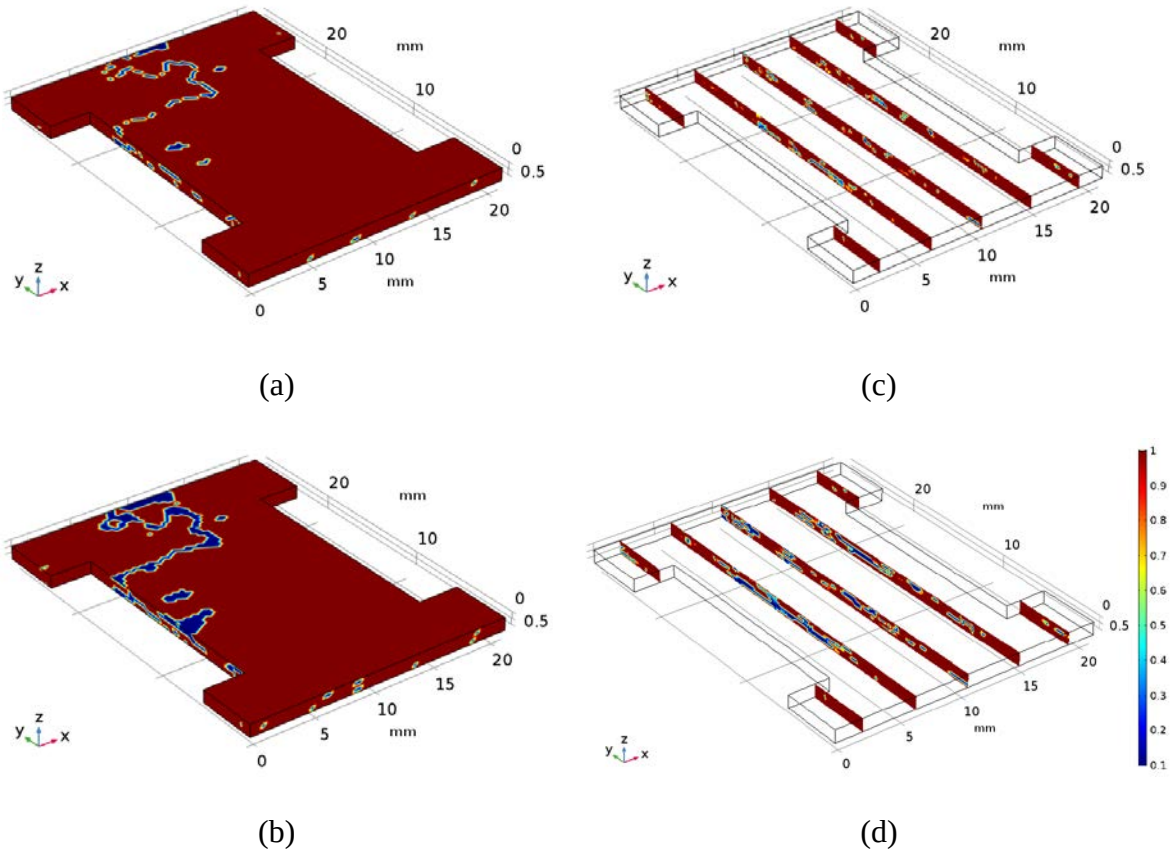

Figure 3.15 (a – b) The electrical conductivity distributions in the Non-Patterned material model when it was subjected to 0.5% and 1% tensile strains along the y-axis, respectively. (c – d) Five cross-sections of the electrical conductivity distributions in (a) and (b), respectively. (a - d) share the same color bar.

3.5. Summary and Conclusions

This chapter focused on investigating the effects of topological designs on the strain sensing performance of nanocomposite thin films. The hypothesis was that the strain sensitivity of a piezoresistive nanocomposite could be controlled by tailoring its topological design and its corresponding stress and strain distribution during applied loading. To engineer and control stress distributions in these thin films, this study proposed two types of topologies, namely, stress-concentrating patterns and Kirigami-based stress-releasing structures. FE models of these

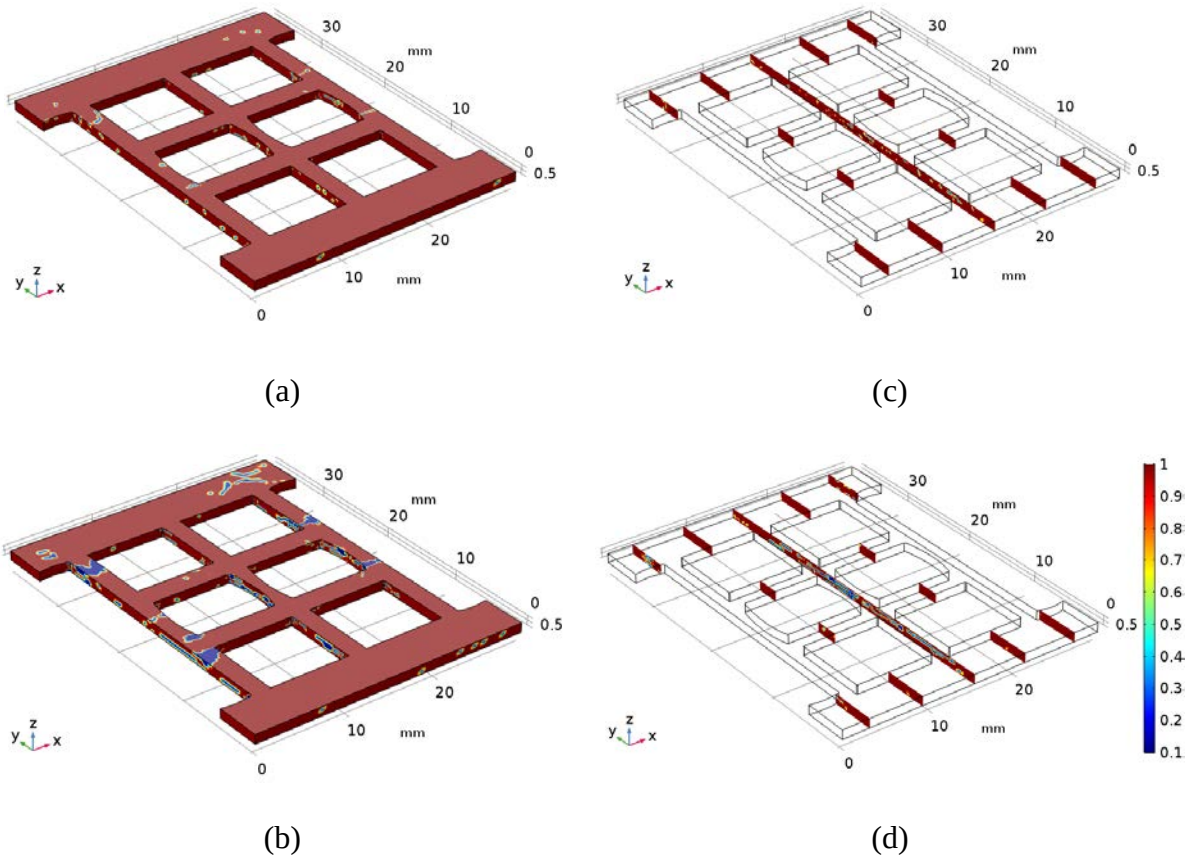

Figure 3.16 (a – b) The electrical conductivity distributions in the Grid material model when it was subjected to 0.2% and 1% tensile strains along the y-axis, respectively. (c – d) Five cross-sections of the electrical conductivity distributions in (a) and (b), respectively. (a - d) share the same color bar.

topologies simulated the stress distributions in the patterned thin films and showed that they could effectively change thin film mechanical response. Then, patterned GNS-EC and CNT-latex nanocomposites were fabricated following the screen-printing and spray-coating techniques described in Chapter 2. Their strain sensing performance was characterized by performing electromechanical tests on the various specimens. It was found that, regardless of the nanocomposite material systems, the stress-concentrating topologies could enhance bulk film strain sensitivity, while the Kirigami-based stress-releasing topologies could effectively suppress piezoresistive response. Furthermore, to numerically investigate the topological effects on the

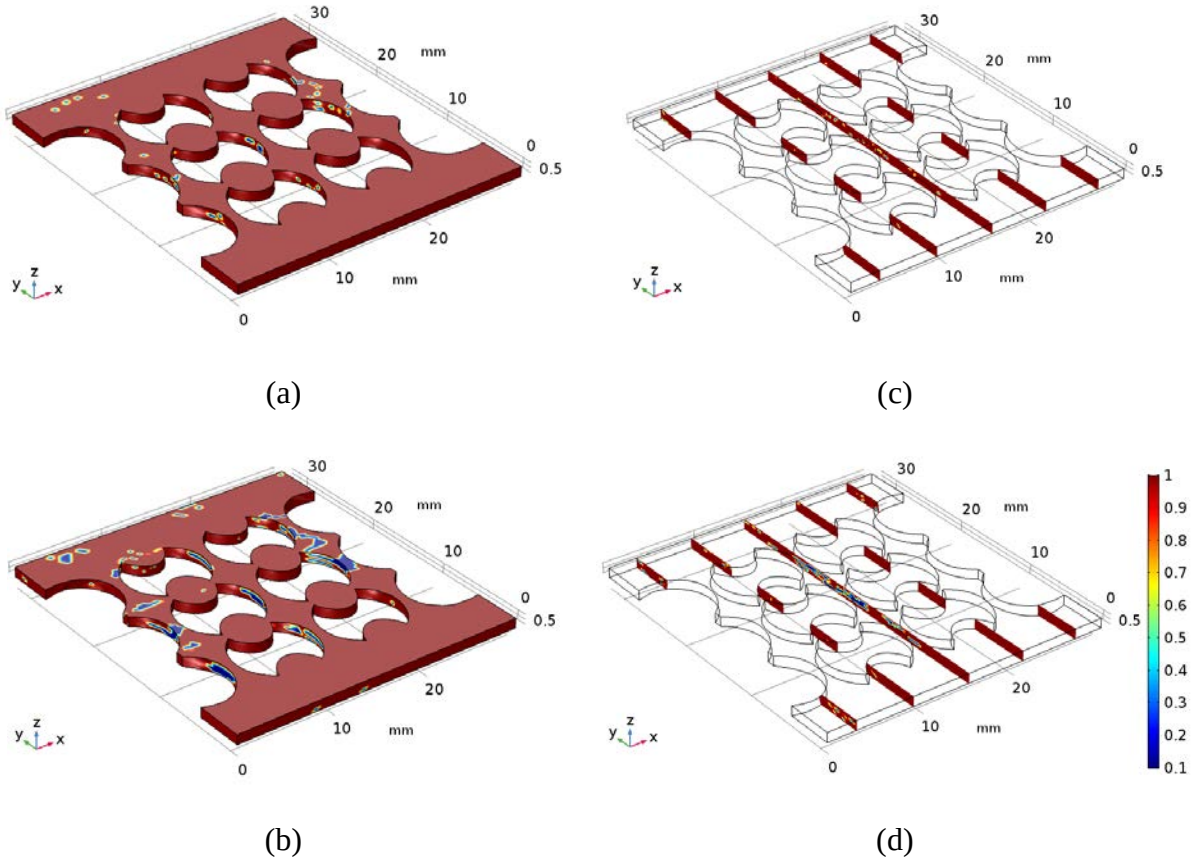

Figure 3.17 (a – b) The electrical conductivity distributions in the Dog-Bone Grid material model when it was subjected to 0.2% and 1% tensile strains along the y-axis, respectively. (c – d) Five cross-sections of the electrical conductivity distributions in (a) and (b), respectively. (a - d) share the same color bar.

nanocomposites' piezoresistivity, both a linear piezoresistive material model and an inhomogeneous percolated material model were developed and implemented. Prior to them being utilized to simulate the patterned material models, both models were calibrated using experimental data obtained from the Non-Patterned control sets. It was found that both models suggested similar topological effects on the nanocomposites' piezoresistive behavior as experimental measurements. In addition, the statistical randomized data-based percolated material model could more accurately characterize the nonlinear strain sensing response of the nanocomposite thin films.

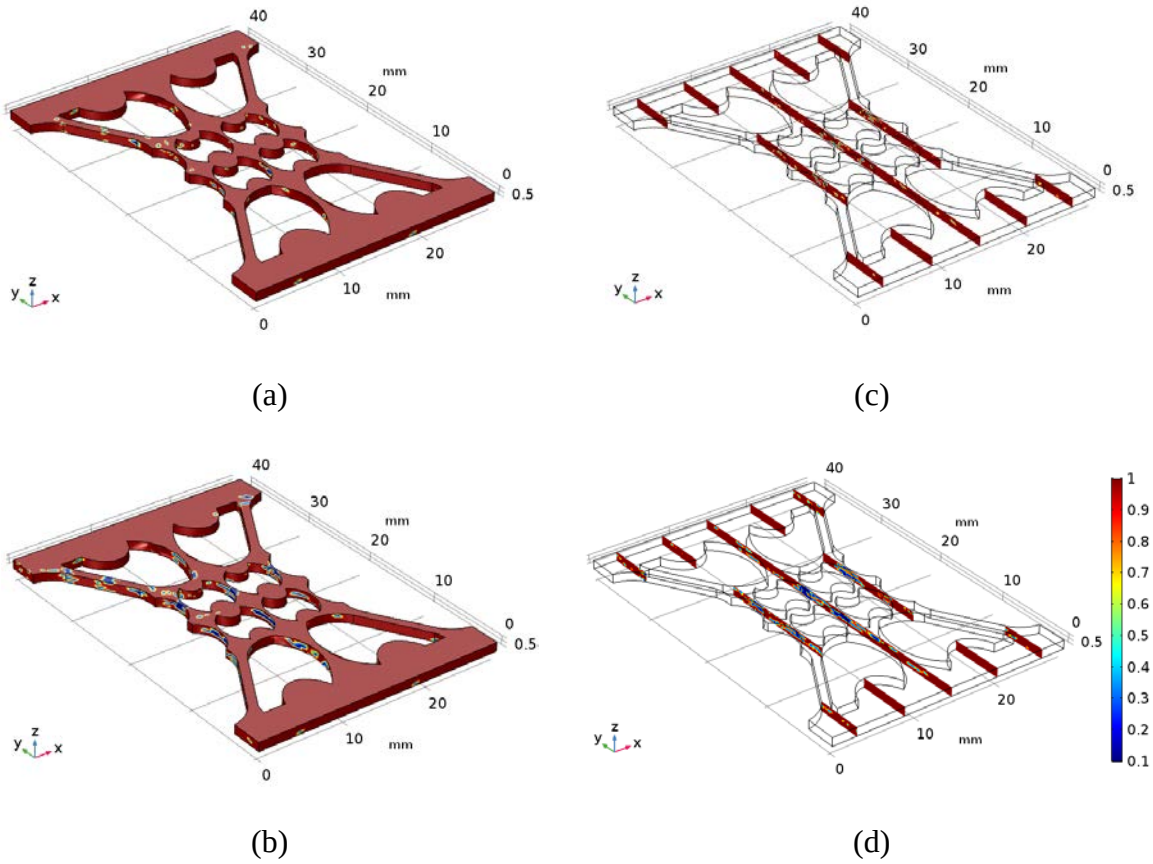

Figure 3.18 (a – b) The electrical conductivity distributions in the Hierarchical Dog-Bone Grid material model when it was subjected to 0.2% and 1% tensile strains along the y-axis, respectively. (c – d) Five cross-sections of the electrical conductivity distributions in (a) and (b), respectively. (a - d) share the same color bar.

Overall, this work demonstrated that the topological design-based approach holds remarkable promise for strategically engineering the performance and properties of functional materials so as to achieve desired multifunctionalities for various target applications. This methodology could potentially overcome the current relatively empirical material development limitation while efficiently encoding predictable material performance and multifunctionalities during manufacturing.

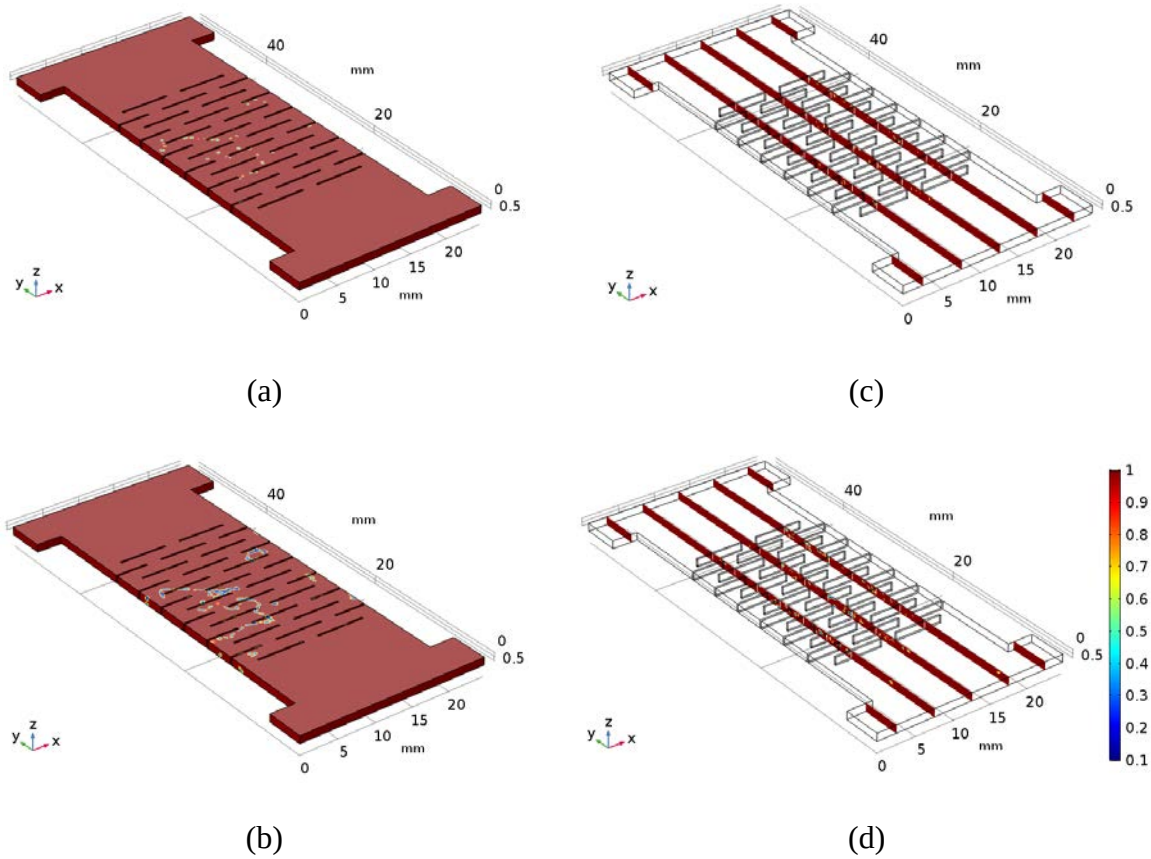

(a) (c)

(b) (d)

Figure 3.19 (a – b) The electrical conductivity distributions in the Kirigami material model when it was subjected to 0.2% and 1% tensile strains along the y-axis, respectively. (c – d) Five cross-sections of the electrical conductivity distributions in (a) and (b), respectively. (a - d) share the same color bar.

Chapter 3, in part, is a reprint of the material as it appears in Topological Design of Carbon Nanotube-based Nanocomposites for Strain Sensing, L. Wang, G. Vella, and K. J. Loh, 2019; Topological Design and Characterization of Piezoresistive Nanocomposites, L. Wang, G. Vella, W.-H. Chiang, and K. J. Loh, 2019; and in part is currently being prepared for submission for publication of the material, Topological Design-Encoded Strain Sensing Performance of Graphene Nanocomposites, L. Wang and K. J. Loh, 2019. The dissertation author was the primary investigator and author of these papers.

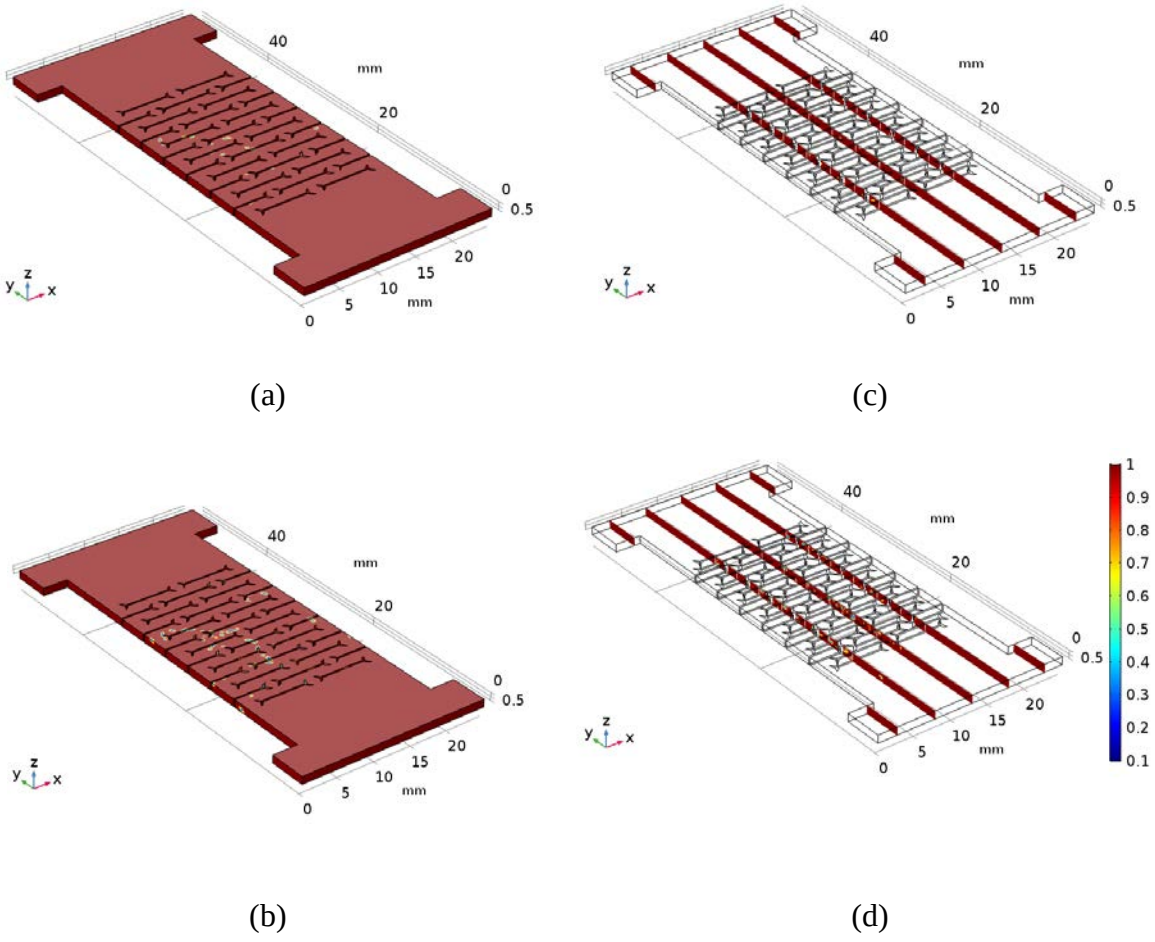

(a) (c)

(b) (d)

Figure 3.20 (a – b) The electrical conductivity distributions in the Modified Kirigami material model when it was subjected to 0.2% and 1% tensile strains along the y-axis, respectively. (c – d) Five cross-sections of the electrical conductivity distributions in (a) and (b), respectively. (a - d) share the same color bar.

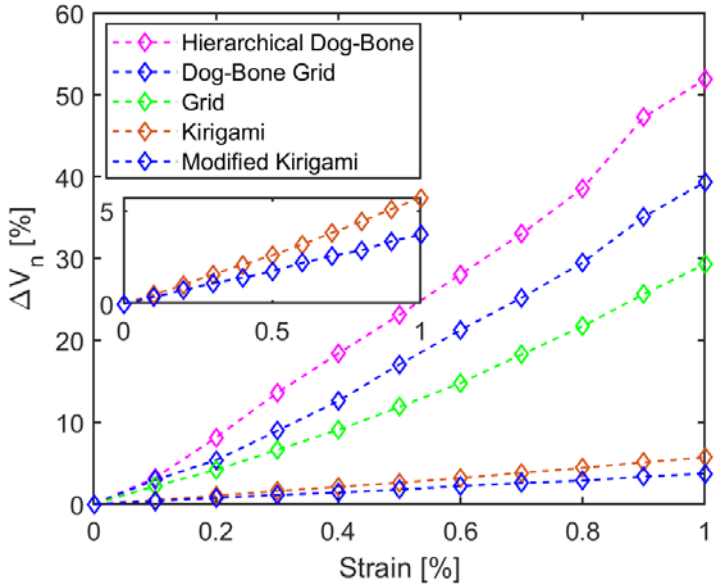

Figure 3.21 The electromechanical responses of different topological material models when they were subjected to up to 1% tensile strain were determined through multi-physics FE modeling. The inset shows a zoomed-in view of the Kirigami-based material models' electromechanical responses.

Chapter 4. Wearable Nanocomposite Sensors for Human Physiological Monitoring

4.1. Introduction

Chapter 2 demonstrated that the CNT- and GNS-based nanocomposites could be fabricated in a low-cost and scalable manner by leveraging optimized spray coating, screen printing, and micro-patterning techniques. The tensile cyclic tests showed that the nanocomposite thin films possessed stable and repeatable strain sensing properties. Furthermore, Chapter 3 proposed a topology design approach to program the nanocomposites' strain sensing properties during their manufacturing, and this approach established the foundation for encoding more complex sensing modalities and functionalities (*e.g.*, temperature and pH sensing) in these nanocomposites.

Based on the aforementioned CNT- and GNS-based nanocomposites, the objective of this chapter is to implement them as strain sensing elements to validate their applications for monitoring human physiological performance (*i.e.*, as wearable sensors). In particular, two different sensing systems were designed, namely, CNT fabric sensors and printed GNS sensors, as building blocks for smart garments and smart skins, respectively. Both designs have been

demonstrated to be mechanically robust, flexible, and compliant to the human body without causing user discomfort. As for the targeted human performance parameters, the nanocomposite sensors were first employed to monitor human motions, including hand motions and eye blinking. It should be noted that human motion monitoring can remarkably facilitate athletic performance assessment, physical therapy development, senior fall prediction, human-machine interfaces, and musculoskeletal studies, among others. In addition, the designed sensing systems were utilized for monitoring human vital signals, including respiration and pulsation, which can be potentially used for personalized healthcare, such as the early diagnosis of cardiovascular diseases.

4.2. Carbon Nanotube Nanocomposite-based Smart Garments

4.2.1. Fabric Sensor Fabrication

The sensing elements were spray-fabricated CNT-latex nanocomposite thin films (Chapter 2.2). As shown in Figure 4.1a, electrodes were directly established on both ends of the thin films (gage length: 48 mm). The film was sandwiched between two layers of double-sided iron-on adhesives and fabrics, and then integrated together by ironing (ironing temperature was ~ 130 ˚C). Finally, the fabric sensors were cut to form 16 × 132 mm^2 smaller specimens for testing. The

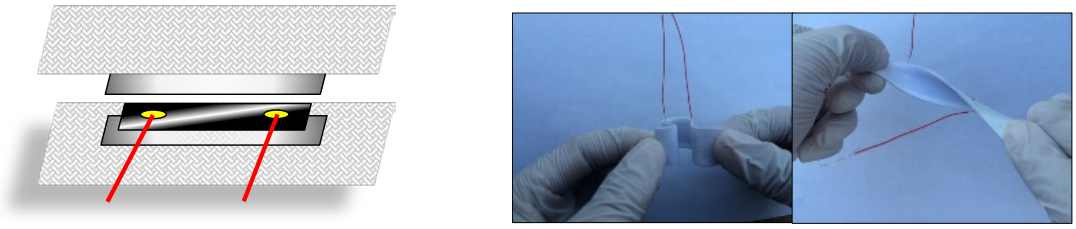

(a) (b)

Figure 4.1 (a) Illustration of the sandwich structure of fabric sensors. (b) Photographs of an assembled sensor subjected to large deformations.

photographs of an assembled specimen in Figure 4.1b indicate that the fabric sensor was highly flexible and that the sandwiched structure was strong enough to undergo large deformations.

4.2.2. Human Motion Monitoring

The sensing elements were spray-fabricated CNT-latex nanocomposite thin films (Chapter 2.2). Validation of human motion monitoring was first performed using a 2 *wt*% CNT fabric sensor for detecting finger bending movements. To be specific, the fabric sensor was longitudinally adhered onto the index finger of a human subject, as shown in the insets of Figure 4.2. During the test, the finger repetitively bent to roughly three different angles, and the sensor's resistance change was recorded by a DMM in real-time. Based on the different angles of finger bending during the tests, the entire monitoring process could be divided into three regions, namely, i, ii, and iii, as marked in Figure 4.2. Within each region, the finger bent back-and-forth multiple times. Owing to the high flexibility of the fabric sensor, it could conform to the finger and deform together, thereby generating electrical resistance changes that followed well with finger movements. Obviously, larger bending angles could generate higher changes in resistance due to greater strains being

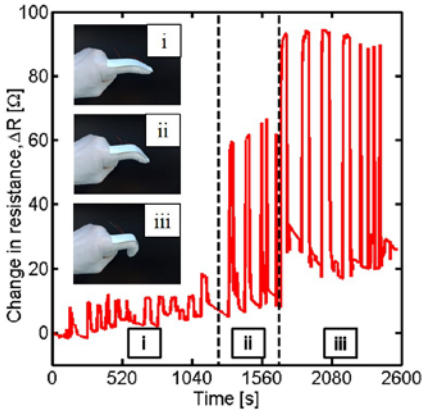

Figure 4.2 Change in resistance of a fabric sensor during finger bending motion tests.

applied. Also, region iii in Figure 4.2 indicates that the fabric sensor was able to detect various finger bending patterns, including holding at the same angle for a few seconds, as well as higher frequency bending movements. On the other hand, the drift in its baseline resistance could be caused by stress relaxation of fabrics, which could be minimized if fabric sensors were pre-loaded or if the fabric sensors are later integrated with a glove instead of being directly attached to the finger.

4.2.3. Respiration Monitoring

The fabric sensors were also used to monitor respiration, where the goal is to capture strain changes caused by thorax expansion and contraction during respiration. Here, sensor design was improved by utilizing conductive threads and stainless steel snap buttons for the electrodes, instead of single-strand wires, as shown in Figure 4.3a. The inset of Figure 4.3b shows both sides of the assembled fabric sensor. Here, conductive threads were sewed tightly on the snap buttons to establish reliable electrical contacts. Resistance measurements were obtained using the snap buttons as electrodes. This new sensor design allowed the fabric sensors to be even more flexible.

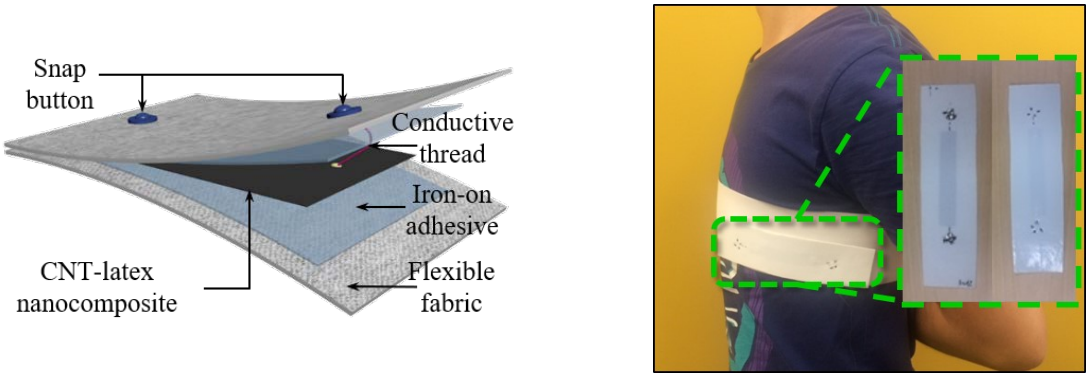

(a) (b)

Figure 4.3 (a) Fabric sensor with conductive threads and snap buttons and (b) attached to a chest band for respiration monitoring.

In addition, with the use of snap buttons, these sensors can be readily installed onto or disassembled from garments, which enabled the sensors to be reusable or exchangeable.

In the respiration monitoring tests, each fabric sensor was implemented on a customized chest band with snap buttons. The chest band was worn by a human subject, as exhibited in Figure 4.3b, and the electrical resistance of the fabric sensor was recorded as the subject breathed. To ensure favorable strain transfer from thorax motion to the sensor, the chest band had to be tight, while the fabric sensor should be taut after installation. In this study, the subject stood still and breathed at a roughly fixed respiration rate, while resistance was measured using a DMM. It should be mentioned that the subject was asked to take deeper breaths, so respiration rate was lower than the typical standard for an adult at rest (*i.e.*, 12 to 20 breaths-min^{-1}). The respiration monitoring tests could be divided into two subsections based on different purposes.

In the first subsection, to validate that the fabric sensors were capable of capturing strain changes near the thorax during respiration, the human subject breathed in different patterns. In particular, the subject sometimes inhaled and exhaled quickly, while occasionally holding the breath for a few seconds. Figure 4.4a shows the representative change in resistance of a 1 *wt*% CNT fabric sensor due to the expansion and contraction motions of the subject's thorax during respiration. One can observe that chest expansion introduced increases in resistance (*i.e.*, applied tension to the sensor), while contraction enabled resistance to restore back to its original level (*i.e.*, released tension). The fabric sensor exhibited stable, reversible, and repeatable response with high signal-to-noise ratio. Besides, Figure 4.4b illustrates that sharp peak-like (i) and step-like (ii) resistance changes could be correlated to fast breathing and breath-holding, respectively. Thus, by integrating the fabric sensors with a chest band, respiration could be monitored in real-time.

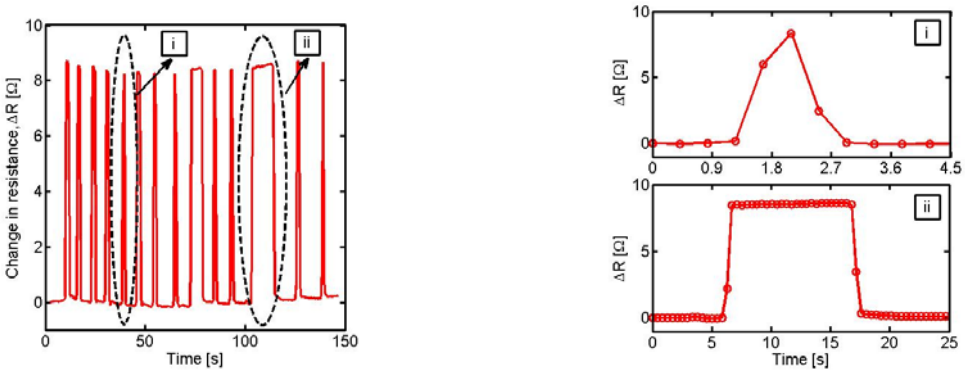

(a) (b)

Figure 4.4 (a) Change in resistance of a fabric sensor during respiration monitoring test. (b) Regular breathing shows sharp peak in change in resistance (i), whereas breath-holding leads to step-like response (ii).

Furthermore, this study also used the fabric sensor measurements for estimating respiration rate (as a significant vital signal). To accomplish this, instead of tediously counting the number of resistance change peaks (*i.e.*, number of breaths taken), the fast Fourier transform (FFT) was used to convert time-domain data to the frequency-domain. Therefore, for this case, the human subject held still and breathed deeply at a slow but regular rate. The data acquisition system recorded data at three times the sampling rate (66 Hz) as compared to previous tests but would unfortunately introduce higher levels of baseline noise to the raw data. To compensate for this, the collected data was first processed using a moving-average approach [166]. Figure 4.5a shows the moving-average, down-sampled, resistance time history results, in which the moving-average was computed using every 51 sets of data. From these results, it is clear that the sensor was still able to quantify resistance changes due to respiration. In addition, one can also observe from Figure 4.5a certain amounts of baseline resistance drift. This could be a coupled result of ambient temperature changes and slight body movements, among others. Therefore, the goal of using FFT was to extract respiration rate in light of noisy and resistance drifts due to ambient effects. In this study, FFT was

conducted using a 60 s moving-window with a time step of 2 s. An example time window, as well as the sensor's response within the time window, is presented in the inset of Figure 4.5a.

The inset of Figure 4.5b demonstrates the corresponding power spectrum (*i.e.*, FFT result) of the same time window shown in the inset of Figure 4.5a. The dominant peak of the power spectrum would occur in the frequency range from 0 to 0.5 Hz, which was then considered as the range of interest. Figure 4.5b zooms in the power spectrum in the 0 to 0.5 Hz frequency range. The frequency corresponding to the peak of the power spectrum peak in Figure 4.5b corresponded to the subject's respiration rate. Since this moving-window FFT analysis was performed in real-time (*i.e.*, using a time window with a step size of 2 s), the extracted respiration rate for each window could be calculated and plotted as a function of time, as shown in Figure 4.6. The results shown in Figure 4.6 suggest that these fabric sensors could be potentially used for monitoring respiration. It should be note that, since the human subject breathed deeply during this test, the respiration rate was relatively slow at 4 – 5 breaths min^{-1}.

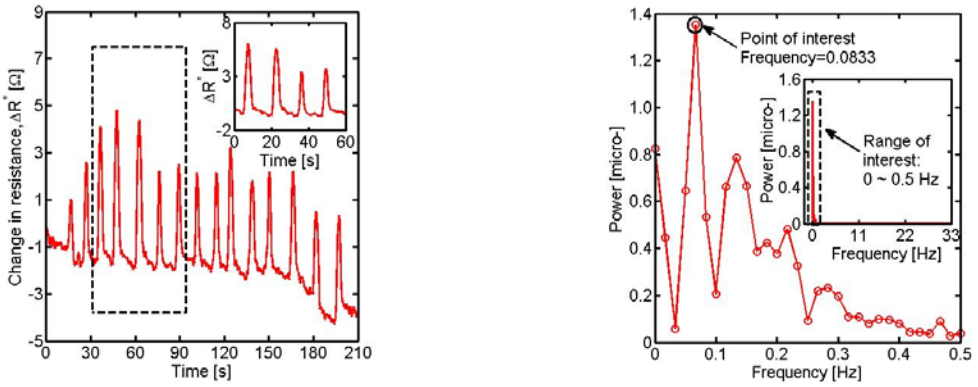

(a) (b)

Figure 4.5 (a) Change in resistance of a fabric sensor acquired during respiration monitoring tests. Inset shows sensor response within a narrower time window. (b) Representative power spectrum of respiration monitoring resistance time history data. Inset shows power spectrum peak (respiration rate) can be easily identified.

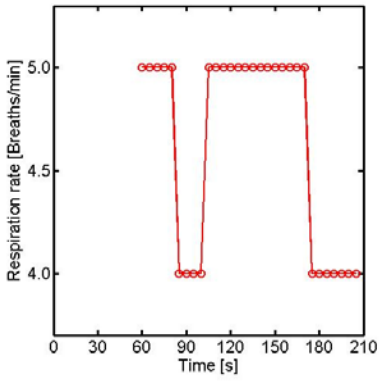

Figure 4.6 Computed respiration rates (updated every 2 s) in real-time.

4.3. Graphene Nanocomposite-based Sensing Skins

4.3.1. Printed graphene sensor-skin compliance

Here, PGS were fabricated by micro-patterning the GNS-CO890 solution on ultra-thin medical tape substrates (Chapter 2.5). Figure 4.7a shows a PGS in its (i) un-deformed state and adhered onto the forearm of a subject; thereafter, the PGS was able to deform compliantly with

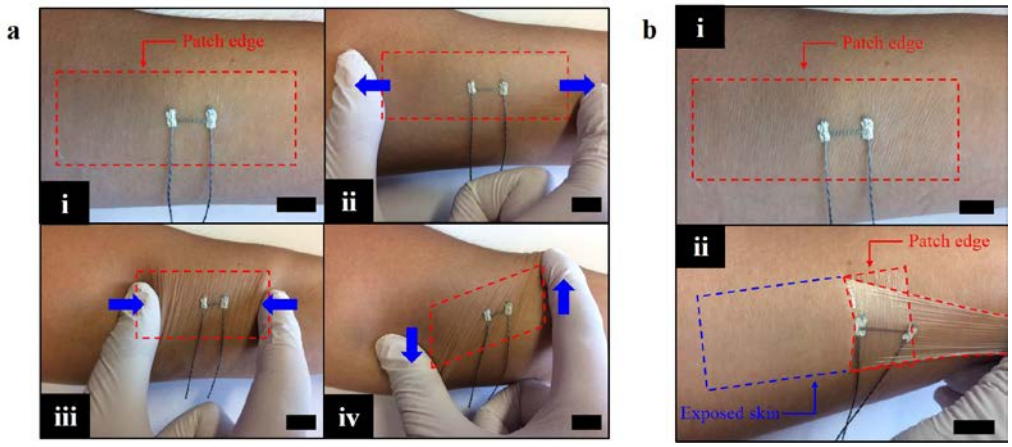

Figure 4.7 (a) Images of a PGS attached onto the skin in its (i) un-deformed state, followed by being subjected to (ii) compression, (iii) stretching, and (iv) shear. (b) (i) A PGS attached onto skin underwent 100 cycles of stretching/compressing. (ii) A PGS was peeled off and partially removed from the skin after being mounted for 2 h. The skin did not show any signs of sensitivity towards the tapes and PGS. All scale bars, 20 mm.

different motions that induced (ii) compression, (iii) tension, and (iv) shear to the sensor. In addition, no damage to the PGS nor detachment occurred after it was repeatedly stretched and compressed for 100 cycles, thereby indicating its mechanical robustness to repeated use, as is shown in Figure 4.7b (i). Furthermore, when the human subject performed daily activities with the PGS attached for 2 h, the subject's motion was not interrupted or constrained by the PGS, owing to its ultra-lightweight (3.9 mg cm^{-2}) and high flexibility. After the PGS was detached from the skin, no irritation (*e.g.*, skin rash) was observed from where it was attached, as can be seen in Figure 4.7b (ii). Thus, the design allows the PGS to be easily attached and removed as necessary, which can be used as a disposable and low-cost skin-mountable device.

4.3.2. Motion pattern recognition

To demonstrate the PGS' potential for monitoring various human activities in real-time, a series of experiments were conducted. Here, the PGS specimens tested consisted of four printed layers, mainly to leverage the superior sensing properties of the 4-layer PGS for accurate measurements. First, the PGS was attached to a subject's index finger for detecting finger movements. Figure 4.8 (i) and (ii) depict the top and side views of the experimental setup, respectively, where the graphene sensing element was aligned with the longitudinal direction of the index finger. During the tests, the finger repeatedly bent to different pre-calibrated angles (Figures 4.8 (iii) ~ (vi)) in a random manner so as to prevent biasing the results if bending was monotonically increased. In the meantime, the PGS' resistance time history was recorded.

Figure 4.9a shows a representative ΔR time history of the PGS when the finger repeatedly bent to different pre-calibrated angles in a random manner so as to prevent biasing the results if bending was monotonically increased. The inset of Figure 4.9a is the PGS' response corresponding

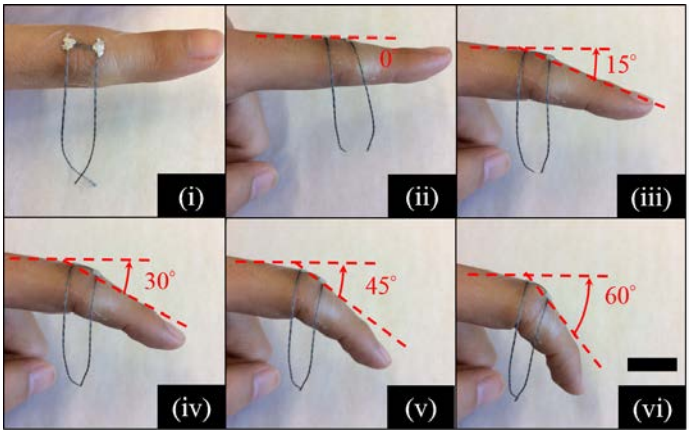

Figure 4.8 (i) Top view of a PGS mounted onto the index finger. (ii-vi) Side views of the finger bent to different angles (i.e., 0˚, 15˚, 30˚, 45˚, and 60˚, respectively).

to 15˚ of bending. In Figure 4.9b, the average ΔR_n and its standard deviations are plotted as a function of the corresponding bending angles. A least-squares regression line was fitted to the data in Figure 4.9b, and an approximately linear sensor response can be observed. However, it can also be observed from Figure 4.9b that some deviation to this linear response can be observed,

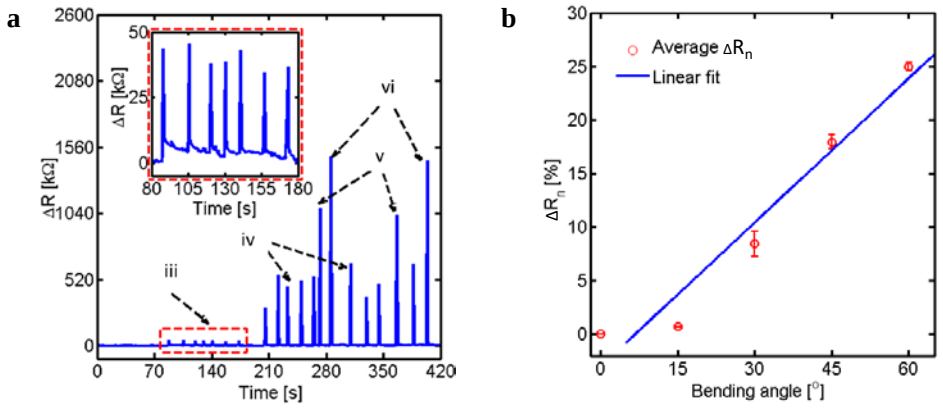

Figure 4.9 (a) The ΔR time history of the PGS corresponding to finger bending. The inset shows the ΔR due to the 15˚ of finger bending case (highlighted in the dashed box). (b) The average ΔR_n plotted as a function of bending angles (standard deviations as error bars) and fitted with a least-squares regression line.

particularly when bending increased from the initial straight state (0˚) to 15˚. This deviation could be a result of the low levels of strains applied when the finger was only bent to 15˚.

Furthermore, it should be noted that, in real-world applications, wearable sensors can be subjected to sophisticated, multi-axis strains (including shear). In order to develop wearable sensors that can characterize complex skin deformations and infer corresponding muscle contractions, simultaneous strain measurements in different directions are needed. Therefore, by further leveraging the advantages of printing technology, PGS was patterned to form a rosette. The sensing elements included three GNS strips oriented in three different directions (*i.e.*, S_a, S_b, and S_c), as shown in the inset of Figure 4.10b (i). Here, to validate multi-directional strain sensing, the PGS rosette was adhered onto the back of a subject's hand (see Figure 4.10b (i)) for distinguishing different hand motion patterns. Figure 4.10b (ii) shows a schematic illustration of the orientation of the PGS rosette with respect to a predefined Cartesian coordinate system.

Figure 4.11a (top) shows that the subject moved the (i) thumb, (ii) index, (iii) middle, (iv) ring, and (v) pinky fingers, individually, and then (vi) typing "*UCSD*" on the keyboard. Figure

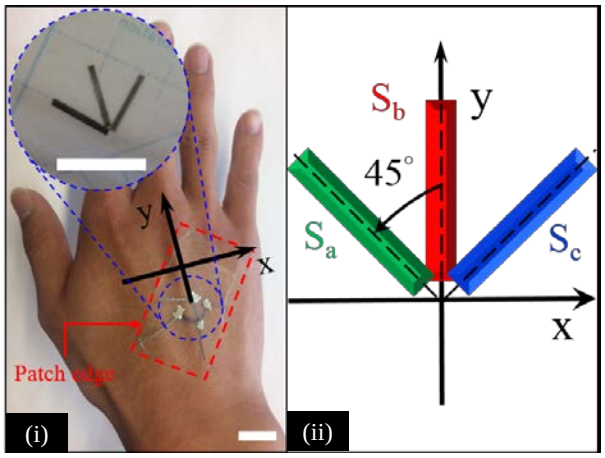

Figure 4.10 (i) Top view of a PGS rosette attached to the back of the hand. The inset shows the PGS rosette before mounting. (ii) A schematic of the orientation of the PGS rosette.

4.11b (bottom) shows the corresponding ΔR_n time history response of each sensing element in the PGS rosette, which indicates that different finger movements induced unique and complex strain patterns that were detectable by the rosette. The strain components (*i.e.*, ε_x, ε_y, and shear ε_{xy}) were calculated based on the classical strain transformation equation [167]:

$$\varepsilon_i = \varepsilon_x \cos^2\theta_i + \varepsilon_y \sin^2\theta_i + \gamma_{xy} \sin\theta_i \cos\theta_i \qquad (i = a, b, c) \tag{4.1}$$

where θ_a, θ_b, and θ_c represent the angles from the ε_x-direction (*i.e.*, where counterclockwise is positive to the S_a, S_b, and S_c directions), which are 135˚, 90˚, and 45˚, respectively (Figure 4.10 ii). In addition, the principal strains (*i.e.*, maximum strain ε_1 and minimum strain ε_2) and principal direction (ε_1) were calculated as follows:

$$\varepsilon_{1,2} = \frac{\varepsilon_x + \varepsilon_y}{2} \pm \frac{1}{2}\sqrt{(\varepsilon_x - \varepsilon_y)^2 + \gamma^2{}_{xy}} \tag{4.2}$$

$$\theta_1 = \frac{1}{2} tan^{-1}\left(\frac{\gamma_{xy}}{\varepsilon_x - \varepsilon_y}\right) \tag{4.3}$$

By assuming that strain varied linearly between sensing elements of the rosette, one could map the spatial strain distribution on the back of the hand using the strain transformation results obtained from the PGS rosette. In particular, Figure 4.11b shows a schematic illustration for the derivation details. The dashed semicircle shows the sensing region of interest. $\vec{n}_0$ is the unit directional vector pointing to an arbitrary point (x_0 , y_0), whereas $\vec{n}_x$ is projection of $\vec{n}_0$ onto the x-axis. The angle between $\vec{n}_x$ and $\vec{n}_0$ are denoted as θ_0. Then, the following can be obtained:

$$\vec{n}_x = (1, 0);\ \vec{n}_0 = \frac{(x_0, y_0)}{\sqrt{x_0^2 + y_0^2}} \tag{4.4}$$

$$cos\,\theta_0 = \vec{n}_x \cdot \vec{n}_0 = \frac{x_0}{\sqrt{x_0^2+y_0^2}};\ \sin\theta_0 = \vec{n}_x \times \vec{n}_0 = \frac{y_0}{\sqrt{x_0^2+y_0^2}} \tag{4.5}$$

$$\varepsilon_0 = \varepsilon_x\, cos^2\,\theta_0 + \varepsilon_y\, sin^2\,\theta_0 + \gamma_{xy}\, sin\,\theta_0\, cos\,\theta_0 \tag{4.6}$$

where ε_0 represents the strain at the arbitrary point. It was assumed that strain remained constant along each radial direction from the origin, and ΔR_n was converted to strains using 21 as the *GF*. Strain mapping was performed using MATLAB.

Figure 4.11c illustrates the spatial-temporal maps of strain distributions of the hand corresponding to different fingers moving. Figure 4.11c shows that the PGS successfully captured and distinguished the minor change in strain distribution on the hand due to contractions of different muscle groups when different fingers moved. Instead of implementing multiple sensors on each finger as reported previously [76, 168, 169], this study showed that a single PGS rosette could recognize the movements of the entire hand with high fidelity. The PGS can be beneficial for establishing new human-machine interfaces, as well as providing insightful information for human behavioral assessment and muscle-epidermis interactions.

4.3.3. Eye blinking monitoring

Besides sensing human motions, the PGS was utilized to detect eye blinking, as is depicted in the inset of Figure 4.12a. Eye movement and blinking are significant clinical parameters for behavior-based diagnosis of impaired consciousness (*i.e.*, coma, vegetative state, and minimally conscious state (MCS)) for patients with brain damage [170]. On the other hand, as for patients with locked in syndrome (LIS) who have complete tetraplegia while preserving intact consciousness and eye movement and blinking, their communication solely depends on eye movement and blinking [171, 172]. In addition, the frequency and intensity of eye blinking can

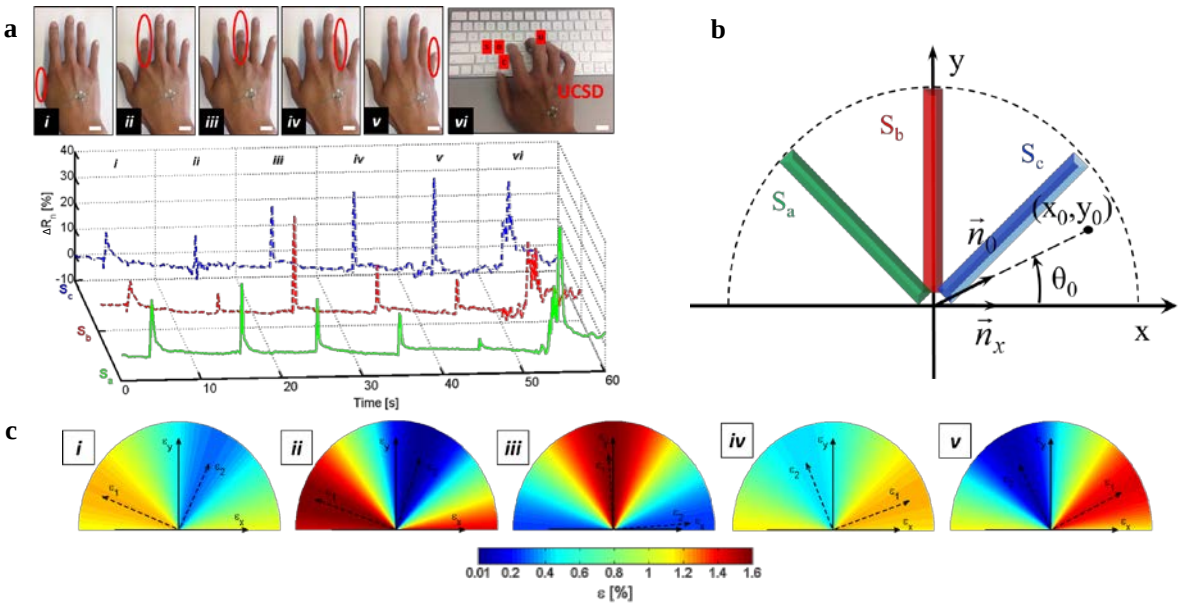

Figure 4.11 (a) (Top) Images of different finger and hand motion patterns (*i.e.*, when the subjected moved the (i) thumb, (ii) index finger, (iii) middle finger, (iv) ring finger, and (v) pinky finger, followed by (vi) typing "*UCSD*"). (Bottom) The representative ΔR_n time history of each sensing element of the PGS rosette corresponding to the different motions. All scale bars, 20 mm. (b) A schematic of mapping the complex 2D strain field. (c) Spatial-temporal maps of strain distribution induced by different hand motions in (a), as measured by the PGS rosette, overlaid with the computed principal strains (ε_1 and ε_2).

indicate human fatigue to some extent. Therefore, by monitoring eye blinking, the PGS is envisioned to facilitate high-fidelity diagnosis of consciousness, improve communications with LIS patients, and facilitate detection of fatigue.

Figure 4.12a shows the ΔR_n time history response of the PGS when the subject blinked repeatedly, where each drop in ΔR_n indicates a blink. Here, the PGS' resistance decreased because the GNS sensing element was compressed in the vertical direction together with the lateral canthus when the eye closed. Figure 4.12b shows a representative detailed view of the change in ΔR_n during an eye blink (*i.e.*, corresponding to the region highlighted in Figure 4.12a). The results confirmed that eye closing and opening corresponded to the drop and increase in ΔR_n, respectively. In

addition, the form factor of the PGS enabled it to capture the transient blinking process in a reversible manner without restricting eye motions or causing user discomfort.

4.3.4. Pulsation monitoring

Furthermore, the PGS' capability for monitoring pulsation was studied, as is shown in the inset of Figure 4.13a. Radial pulse is one of the most representative vital signals that is commonly measured in clinical practice to quantify human physiological performance (*e.g.*, blood pressure, heart rate, and vascular stiffness) [173]. Moreover, radial pulse wave monitoring also facilitates early diagnosis of cardiovascular diseases. Here, the PGS' potential for monitoring pulsation was explored by attaching the PGS onto the surface of the skin close to the radial artery of a human subject's (a 25-year-old male) wrist. The PGS was used to measure pulse signal when the subject was at rest and after rigorous exercise for 40 s.

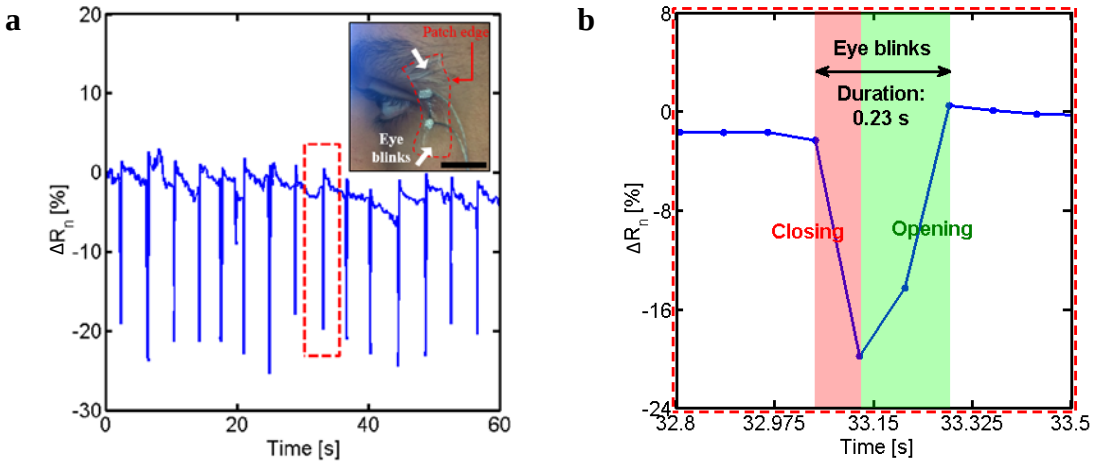

Figure 4.12 (a) The representative ΔR_n time history of a PGS corresponding to eye blinking. The inset shows a PGS that was mounted on the subject' lateral canthus. (b) Detailed view of the ΔR_n data included in the dashed box in (a).

Figure 4.13a shows the pulse signal measured by the PGS when the subject was at rest and after rigorous exercise. The PGS exhibited good SNR due to its high strain sensitivity and conformability. Figure 4.13b provides a detailed view of the cardiac cycles highlighted in Figure 4.13a. The typical features of a radial pulse wave (including systolic peak, diastolic peak, and dicrotic notch) are distinguishable from the sensor's measurements when the subject was at rest [173-175]. The time interval between the systolic and diastolic peaks (ΔT) was measured as ~ 310 ms, which was normal for adults in their 20s [174]. It is known that ΔT depends on artery stiffness, which increases with age. Artery stiffness is a precursor for various cardiovascular diseases, such as myocardial infarction and stroke [176]. To further quantify artery stiffness, stiffness index (SI) can be calculated as follows [174, 175]:

$$SI = \frac{H}{\Delta T} \tag{4.7}$$

where H is the height of the human subject. Here, SI was calculated to be ~ 5.6 m s^{-1}, which is within the normal range for a healthy adult [174, 175]. However, the measured radial pulse waveform could not distinguish the aforementioned features after the subject exercised (Figure 4.13b) [173].

In addition, to quantify heart rate, the radial pulse signals were analyzed using continuous wavelet transform (CWT), thereby enabling time and frequency localization. Figures 4.13c and 4.13d show the real-time heart rate spectrograms when the subject was at rest and after exercise, respectively. The red regions represent dominant frequencies of the radial pulse signals, which were converted to heart rates. The average heart rates of the subject at rest and after exercise were 60 beats per minute (bpm) and 114 bpm, respectively, which were both within the normal range.

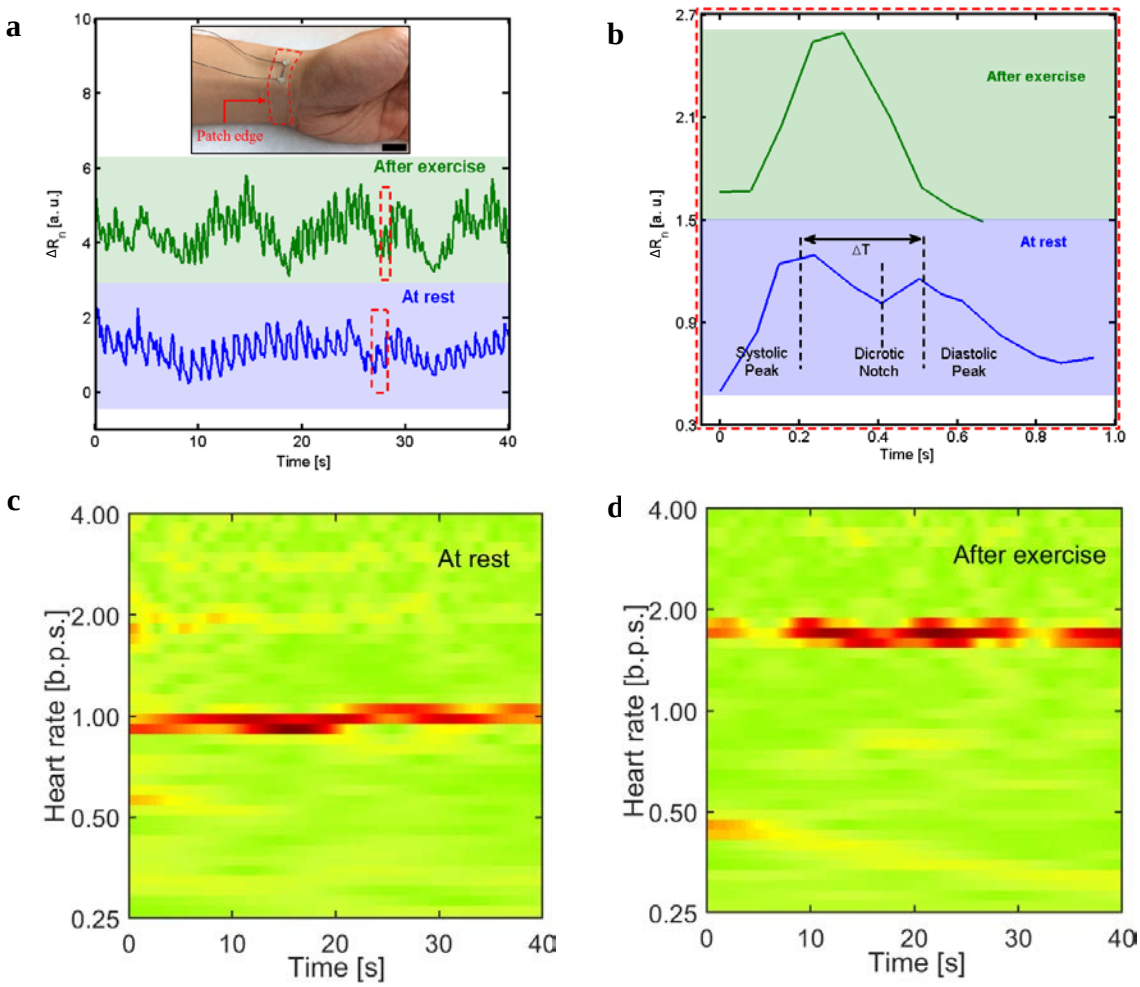

Figure 4.13 (a) The representative ΔR_n time history of the PGS when it was employed for monitoring radial pulse of a human subject at rest and after exercise. The inset shows the sensor attached to the wrist of the subject. ΔR_n is of arbitrary unit for easy comparison. Scale bar, 20 mm. (b) The radial pulse waveforms in the dashed boxes in (a). (c, d) Heart rate spectrograms when the subject was at rest and after exercise, respectively. The red regions indicate the dominant frequencies (*i.e.*, measured heart rates).

4.4. Summary and Conclusions

In this chapter, CNT-based fabric sensors and PGS were used as discrete wearable sensors for monitoring human physiological performance. To be specific, the CNT-based fabric sensors were first applied to detect finger bending movements as a proof-of-concept demonstration for human motion monitoring. It was found that they could capture different bending motions and

exhibited relatively stable response. Second, the fabric sensors were integrated with a chest band for monitoring respiration. The resistance change of the fabric sensors was well-correlated with the expansion and contraction movements of the subject's thorax. Furthermore, respiration rate was successfully extracted using a moving-window FFT analysis, and the results could be visualized in real-time. The results obtained in this study suggest that these CNT-based fabric sensors could potentially be used for applications, such as multifunctional wearable sensors or be integrated as part of "smart garments".

The second major part of this chapter demonstrated that the designed PGS was highly flexible, ultra-lightweight, conformable, and could be easily adhered to or detached from the skin. In addition, to investigate its applications for human monitoring, the PGS was strategically attached to different parts of the human body. The experiments showed that the PGS was capable of quantifying finger bending motions, identifying hand motion patterns (and strain distributions), monitoring eye blinking, and capturing radial pulse signals. To improve the practical applicability of PGS, future work will focus on incorporating flexible wireless transmission circuits. In addition, by further employing versatile and low-cost printing techniques, more robust and high-performance sensor designs, including multi-materials and multi-modal sensing capabilities, can be achieved. Overall, based on the studies in this chapter, the vision is that the nanocomposite sensors can potentially be used as low-cost, disposable, wearable devices for human-machine interfaces, rehabilitation, human performance assessment, and even telemedicine.

Chapter 4, in part, is a reprint of the material as it appears in Micro-Patterned Graphene Sensing Skins for Human Physiological Monitoring, L. Wang, K. J. Loh, W.-H. Chiang, and K. Manna, 2018; and Wearable Carbon Nanotube-Based Fabric Sensors for Monitoring Human

Physiological Performance, L. Wang and K. J. Loh, 2017. The dissertation author was the primary investigator and author of these papers.

Chapter 5. Nanocomposites-Based Spatial Sensing Systems

5.1. Introduction

Chapter 4 focused on utilizing the piezoresistive nanocomposite thin films as sensing elements for monitoring human motions and physiological health, where the nanocomposites were integrated with flexible substrates (*i.e.*, fabrics and medical tapes). The proposed sensing devices were highly flexible and compliant to the human body, which enhanced data accuracy and avoided user discomfort. Although the nanocomposites-based sensing systems exhibited significant advantages over conventional rigid electronic transducers, the aforementioned methodology still relied upon discrete sensing, implying that the acquired data were only relevant to the locations where they were instrumented. Therefore, the primary objective of this chapter was to design and characterize a spatial sensing system that is capable of identifying and locating potential anomalies. Densely distributed sensing was demonstrated using fabric-based nanocomposite sensors for pressure sensing applications. The outcome of this study was the validation of a nanocomposites-based spatial sensing system that could be implemented on both engineered structures and the human body.

In the context of large-scale monitoring applications, distributed sensing is more desirable for comprehensively acquiring spatial information of target structures, so as to identify and locate abnormal structural performance and to efficiently inform the decision-making process (*e.g.*, for structural maintenance and retrofitting) [34, 177]. It should be noted that spatial sensing can be challenging when sensing streams are acquired from traditional transducers, since there is an inherent tradeoff between spatial sensing resolution and the difficulty, logistics, and costs associated with installing a dense network of sensors [34, 40, 178].

To address the aforementioned sensing limitations and to achieve spatial sensing, this chapter focuses on integrating the proposed nanocomposite thin films with imaging and signal processing techniques, namely, electrical impedance tomography (EIT) and compressed sensing (CS), respectively. The coupled densely distributed sensing systems could truly leverage the unique property of multifunctional nanocomposites such that every location across the continuous thin films are sensitive to different stimuli (*e.g.*, strains).

This chapter starts with introducing the concept and formulation of EIT (Section 5.2), where the main challenge was to efficiently and accurately solve the inverse problem to reconstruct the conductivity (or resistivity) distribution of the nanocomposite sensing element. To handle such a challenge, a CS scheme was adopted to take advantage of the prior knowledge of typical EIT problems (*i.e.*, spatial sparsity), as discussed in Section 5.3.4. Then, Section 5.4 demonstrated the application of the coupled system to detect spatially distributed deformations and puncture damage, so as to characterize the performance of the distributed sensing system. Last, Section 5.4.3 conducted a resolution analysis of the EIT inverse problem reconstruction and compares the results computed using Tikhonov regularization algorithm (discussed in Wang *et al.* [179]) and sparsity reconstruction algorithm, respectively.

5.2. Electrical Impedance Tomography

5.2.1. Forward problem

Electrical impedance tomography is essentially an electrical imaging technique, where it determines the electrical conductivity (or resistivity) distribution of a conductive body of interest [180-182]. In practical experiments, the conductive body is interrogated using an electrical current, and the induced boundary voltages are all recorded. This procedure needs to be repeated for several times with current injected from different pairs of electrodes to gather enough spatial information of the conductive body. The boundary voltage measurements are used as inputs to the EIT algorithm. Thus, the EIT technique is advantageous in that it is capable of characterizing the internal electrical properties of an object only based on measurements obtained along its boundary [180, 182]. Provided that the electrical conductivity distribution of the body is sensitive to applied strains (*i.e.*, piezoresistive materials), the boundary voltages will also change accordingly, depending on the distribution of strain exerted on the conductive body. Therefore, one can use EIT and a piezoresistive material (which in this case is the nanocomposite sensing films) for quantifying the strain distributions of structural components where the system is implemented.

In general, the EIT algorithm includes the forward and inverse problems. The forward problem aims to solve for boundary voltages (v) based on an assumed conductivity (σ) distribution. Without any current sources within the object (Ω), the forward problem can be formulated as a simplified 2D Laplace's equation as follows:

$$\nabla \cdot (\sigma \nabla v) = 0 \quad in\ \Omega \tag{5.1}$$

The complete electrode model (CEM) is recognized as one of the most accurate and efficient models for mathematically modeling the EIT measurement procedure [183-185]. The

CEM considers electrodes ($\{e_l\}_{l=1}^{L}$) as perfect conductors (*i.e.*, shunting effect), as well as the contact impedance at electrodes and object interfaces. The CEM can be expressed as follows:

$$\begin{cases} v + z_l \sigma \frac{\partial v}{\partial n} = V_l & on\, e_l,\, l = 1, 2, \cdots, L \\ \int_{e_l} \sigma \frac{\partial v}{\partial n} dS = I_l & for\, l = 1, 2, \cdots, L \\ \sigma \frac{\partial v}{\partial n} = 0 & on\, \Gamma \end{cases} \tag{5.2}$$

where z_l is the contact impedance between boundary electrodes and the object Ω, n is unit vector outward normal to the surface ($\Gamma = \partial\Omega$) of the object Ω, and L is the total number of boundary electrodes. V_l and I_l ($l = 1, \cdots, L$) are the measured electrode potentials and injected current on the l^{th} electrode, respectively. In addition, injected current satisfies the charge conservation law by imposing Equation 5.3:

$$\sum_{l=1}^{L} I_l = 0 \tag{5.3}$$

Furthermore, the grounding potentials are imposed using Equation 5.4:

$$\sum_{l=1}^{L} V_l = 0 \tag{5.4}$$

In the EIT forward problem, the assumed isotropic electrical conductivity σ, injected current I, and contact impedance z_l are known *a priori*. The forward problem is typically solved using the weak-form of Equation 5.1 in conjunction with a finite element model (FEM) of the conductive body Ω. Then, the forward problem can be expressed as a set of linear equations combined in the form of

$$A(\sigma)b = I \tag{5.5}$$

where $A(\sigma)$ is a square matrix as a discretized expression of CEM, and b is a coefficient vector to be determined, which contains elemental nodal potentials as well as boundary electrode voltages. Here, $A(\sigma)$ is invertible for σ so that there exists a unique solution to the forward problem [184, 186].

5.2.2. Inverse problem

Reconstructing the inverse problem is relatively more challenging in the EIT problem, and this has attracted extensive studies focusing on enhancing the efficiency and accuracy of the algorithms [180, 182, 184, 187]. If the forward problem is expressed using a general operator as follows:

$$V = F(\sigma) \tag{5.6}$$

where $F(\sigma)$ is the operator that maps injected current to boundary electrode potentials based on corresponding conductivity distribution σ. V represents boundary voltages, which can be either theoretically calculated values (Equation 5.1) or experimentally measured data V_{meas} (with measurement noise added to the right-hand side of Equation 5.6).

On the other hand, the inverse problem seeks to estimate the conductivity distribution σ of the body Ω from boundary voltages V, which can be expressed as

$$V = F^{-1}(\sigma) \tag{5.7}$$

Given an initial estimate of σ_0 that is close to the actual solution, the forward operator $F(\sigma)$ can be linearized by only considering the first-order term in its Taylor expansion, as follows:

$$F(\sigma) = F(\sigma_0) + F'(\sigma - \sigma_0) \tag{5.8}$$

where F' represents the Jacobian matrix (J) for discretized elements calculated at σ_0. In the context of practical applications (*i.e.*, the interest of this study), the inverse problem aims to compute σ based on experimentally measured boundary voltage data (V_{meas}) and the forward problem computed values. Letting $\delta V = V_{meas} - F(\sigma_0)$, Equation 5.8 can be re-written as:

$$\delta V = J\delta\sigma \tag{5.9}$$

where $\delta\sigma = \sigma - \sigma_0$ represents the inhomogeneous conductivity inclusion in the conductive body Ω, which can be correlated to mechanical disturbance to the sensing materials' electrical properties in this study. Thus, reconstructing the change in electrical conductivity (or resistivity) of the sensing materials by solving the EIT inverse problem can allow one to noninvasively identify and locate anomalies in the structure (especially since the sensing material's electrical properties are pre-calibrated to applied strains in this study).

In ideal cases, Equation 5.9 implies that $(J^T J)\delta\sigma = J^T \delta V$. However, in practice, there can be computational errors in forward problem modeling as well as measurement noise in the experiments. Due to the ill-posedness of the EIT inverse problem, small computational or experimental errors can lead to a significantly inaccurate reconstruction solution, which makes it challenging to minimize the difference between experimental measurements and simulated forward problem values [182, 187]. Therefore, to stably reconstruct the inverse problem, a penalty term (or regularization term) that includes assumptions consistent with prior information needs to be imposed, which results in the commonly used objective function as follows:

$$\delta\sigma = argmin\frac{1}{2}\|J\delta\sigma - \delta V\|_2 + \lambda\phi(\delta\sigma) \tag{5.10}$$

where $\phi(\delta\sigma)$ is the penalty function, and λ is the regularization parameter that balances data fitting and the penalty term.

In addition, from a practical application standpoint, reliably solving the EIT inverse problem requires changes in signals that are sufficiently above the experimental noise level and computational errors. In other words, the conductive body Ω needs to generate significant enough electrical property changes when subjected to external perturbations. Therefore, for damage detection and monitoring applications, it is of paramount importance to develop high-performance strain sensing materials (*i.e.*, conductive body) (Chapter 2) that are potentially capable of resolving small changes in structural strain/stress distributions, thereby generating corresponding data of high signal-to-noise ratio.

5.2.3. Tikhonov reconstruction

Tikhonov regularization has been most commonly used to reconstruct the EIT inverse problem. It employs L_2 minimization as the penalty term (*i.e.*, $\phi(\delta\sigma)$ in Equation 5.10). Then, the objective function can be expressed as:

$$\delta\sigma = argmin\frac{1}{2}\|J\delta\sigma - \delta V\|_2 + \frac{\alpha}{2}\|L\delta\sigma\|_2 \tag{5.11}$$

where α is the regularization parameter that balances the data fitting and L_2 regularization. L is an appropriate regularization matrix, which is formulated as an identity matrix in this study (*i.e.*, $L = I$). Then, the solution to the linearized regularization problem can be obtained as (with $L = I$):

$$\delta\sigma = (J^T J + \alpha I)^{-1} J^T \delta V \tag{5.12}$$

Upon solving Equation 5.12, a new estimate for σ can be obtained with $\sigma_{i+1} = \sigma_i + \delta\sigma$. Then, the algorithm iteratively updates the reconstruction by using the new estimate for σ as an

initially assumed value (*i.e.*, Gauss-Newton method). The stopping criterion can be based on either the relative error in boundary voltage prediction or the number of iterations, depending on the demands for reconstruction accuracy and computational costs. Although the Tikhonov regularization is relatively easy to solve, it tends to impose an over-smoothing effect on the EIT inverse problem reconstruction. As a result, the reconstructed EIT images are usually blurred, indicating a considerably compromised resolution and accuracy [181, 186, 188].

5.2.4. Sparsity reconstruction

In order to further to improve the resolution and accuracy of the EIT inverse problem reconstruction, a CS scheme was adopted in this study [181, 186]. Particularly, CS theory states that, if the unknown signal is sparse, it can be accurately reconstructed using far less measured data than that obtained at the data acquisition rate required by Shannon's law [189-193]. In fact, most of the real-life physical signals are sparse (*i.e.*, fulfilling the assumption of CS) on an appropriate basis, which renders CS theory promising for a plethora of signal processing related applications, such as imaging, geophysics, and astronomy, among others [190-192].

In the context of typical EIT problems, the images (*i.e.*, signals) to be reconstructed include only a limited portion of interesting features (*i.e.*, significant entries), which is embedded in an uninteresting background. It indicates a prior knowledge of sparsity (in the spatial domain) in the EIT problem and that the CS theory is applicable. Particularly, this study has implemented L_1-norm regularization as the penalty term in Equation 5.10, since it was shown to be capable of leveraging signals' sparsity [191, 192]. Then, the formulation of the objective function becomes:

$$\delta\sigma = argmin\frac{1}{2}\|J\delta\sigma - \delta V\|_2 + \lambda\|\delta\sigma\|_1 \tag{5.13}$$

where λ is the regularization parameter that balances data fitting and L_1-norm penalty term. $\|\delta\sigma\|_1$ is the L_1-norm of $\delta\sigma$, which essentially refer to the sum of the absolute values of $\delta\sigma$.

Since the L_1-norm penalty term makes the regularization function non-differential, it requires a robust algorithm to efficiently minimize the objective function. With the advancement of CS methodologies, various algorithms have been proposed to solve the L_1-norm regularization problem, which show different performances depending on specific application scenarios [181, 188, 191, 192]. Particularly, this study mainly employed a two-step iterative shrinkage thresholding (TwIST) algorithm due to its relatively more robust performance in the target applications. The TwIST algorithm was first developed by Bioucas-Dias *et al.* [194] based on the standard iterative shrinkage thresholding (IST) method. It aims to more efficiently solve ill-posed problems while maintaining the good denoising performance of IST. Here, to adopt the TwIST method for solving EIT inverse problem, the algorithm has been modified as follows:

$$\delta\sigma_1 = \varphi_\lambda(\delta\sigma_0 + J^T(\delta V - J\delta\sigma_0)) \tag{5.14}$$

$$\delta\sigma_{t+1} = (1-\alpha)\delta\sigma_{t-1} + (\alpha-\beta)\delta\sigma_t + \beta\varphi_\lambda(\delta\sigma_t + J^T(\delta V - J\delta\sigma_t)) \tag{5.15}$$

where α and β are parameters determined by prior data. It should be noted that $\delta\sigma_{t+1}$ is dependent on both $\delta\sigma_{t-1}$ and $\delta\sigma_t$, which is the reason the algorithm involves two steps. The TwIST algorithm will transform to IST if the parameter α equals to 1 (*i.e.*, $\delta\sigma_{t+1}$ depends only on $\delta\sigma_t$). φ_λ is the soft shrinkage operator, which is in the form of:

$$\varphi_\lambda(\delta\sigma_t, \lambda) = sign(\delta\sigma_t)max(|\delta\sigma_t| - \lambda, 0) \tag{5.16}$$

The stopping criteria of the iterative algorithm can be based on either the relative error lower than pre-defined threshold or the number of iterations.

5.3. Spatial Sensing Validation Experiments

5.3.1. Fabric sensor fabrication and sample preparation

The spray-fabricated CNT-latex nanocomposites were used as sensing elements (260 × 200 mm^2) for the fabric sensors (Chapter 2). A schematic of the procedure for assembling the sensors is shown in Figure 5.1a. First, 8 × 6 electrodes (28 in total) with an equal spacing were established on the four boundaries of the sensing films by drying silver paint over conductive threads and the film. The number of electrodes can be customized depending on the dimensions of the sensing films and the desired sensing resolution. Conductive threads, which are commercially available, were used in lieu of other types of electrodes (*e.g.*, copper tape or multi-strand wires) for maximizing the flexibility of the fabric sensors. Then, the sensing element was integrated with the fabric by sandwiching it between two layers of iron-on adhesives and then ironing them directly onto the polyester fabric. This procedure resulted in a highly flexible, strong, waterproof, and integrated sandwich structure. Figure 5.1b shows a photograph of an assembled fabric sensor prototype, which was also used for experimental testing.

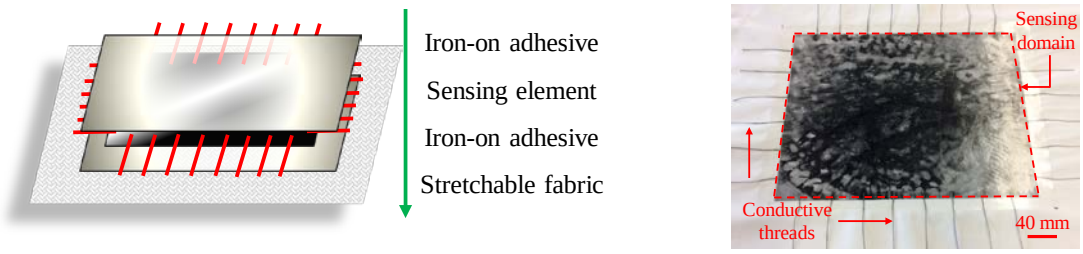

(a) (b)

Figure 5.1 (a) An MWCNT-latex thin film is integrated with flexible fabric, and (b) a photograph of a fabric sensor prototype.

5.3.2. Spatially distributed pressure and impact damage detection

The boundaries of the aforementioned fabric sensor (Figure 5.1b) was mounted on a customized support, which had a cavity below the sensing domain of the fabric sensor to allow pressure-induced out-of-plane deformations. The schematic of the experimental setup is shown in Figure 5.2. Spatial sensing tests were conducted by interrogating the sensor to collect the necessary boundary voltage measurements for EIT spatial conductivity reconstruction. Here, a customized data acquisition (DAQ) system was employed to perform automated EIT measurements. A Keithley 6221 current source was interfaced with the switch to inject 5 mA of direct current (DC) across a certain pair of boundary electrodes. To automatically switch the pair of electrodes for injecting a different DC excitation pattern, the current generator was interfaced with a Keysight 34980A multifunctional switch, which was controlled using a customized *Matlab* program. Furthermore, the switch includes a built-in DMM that could measure and record voltages that developed between the other pairs of electrodes. The entire set of voltage measurements were then used as inputs to the EIT algorithm for reconstructing the fabric sensor's conductivity (or resistivity) distribution. It should be noted that the accuracy and resolution of the sensing results could be potentially improved by including more boundary electrodes. However, this will in turn

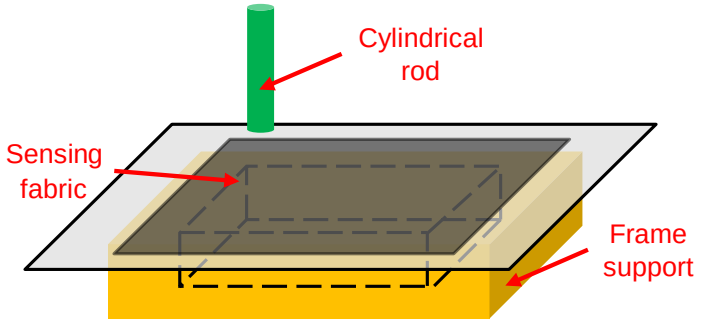

Figure 5.2 Schematic of the spatial pressure distribution experimental setup.

increase the time needed for experimental measurements and computational demand required for solving the EIT inverse problem. Therefore, an optimized boundary electrodes setup (*i.e.*, from a sensing hardware perspective) should be designed to strike a balance between accuracy and efficiency, specifically, when considering real-world applications. In addition to the sensing hardware optimization, the EIT algorithm (*i.e.*, from a computational perspective) could also be optimized to obtain enhanced sensing performance, which was also in the scope of this study and will be discussed later in this section.

The EIT DAQ system was commanded to obtain an initial set of boundary voltage measurements when no pressure or damage was introduced to the specimen (*i.e.*, to establish the baseline). Then, for the pressure sensing test, cylindrical rods were used to apply localized pressure at different regions on the sensing fabric. On the other hand, the last set of experiments introduced permanent damage to the fabric sensor. Puncture damage was created, one-by-one, by penetrating and leaving a small hole in the fabric sensor using a sharp rod.

From the strain sensing performance characterized in Chapter 2, it was expected that applied pressure would generate an increase in sensing films' electrical resistance at the corresponding locations. Thus, by using EIT to reconstruct the relative change in resistivity distribution of the sensing fabric (relative to the baseline), the location and magnitude of applied localized pressure could be identified. It should be noted that this chapter aims to highlight the enhanced resolution and accuracy of the EIT inverse problem reconstruction through employing the sparsity reconstruction algorithm (Equations 5.13 to 5.16), as compared to the results obtained using conventional Tikhonov reconstruction algorithm (Equations 5.11 to 5.12) that are discussed in Wang *et al.* [179].

As mentioned earlier, two experimental cases were investigated, namely, nondestructive pressure sensing tests and impact damage detection tests. During the pressure sensing tests, the fabric sensor was first subjected to a single pressure point. Figures 5.3a to 5.3d illustrate the positions of applied pressure points (*i.e.*, highlighted by the red circles). Based on the sparsity reconstruction algorithm, Figures 5.3e to 5.3h show the computed EIT resistivity maps of the sensing fabric corresponding to the pressure "hot spots" applied in Figures 5.3a to 5.3d, respectively. The EIT results clearly show changes in resistivity ("highlighted spots") where pressure was applied, while the remainder of the sensing area reflected almost no change in electrical properties. This was consistent with the fact that the fabric only deformed locally where pressure was applied. Thus, the EIT results shown in Figures 5.3e to 5.3h demonstrate that pressure detection and localization could be achieved. It should be noted that, since applied force/pressure

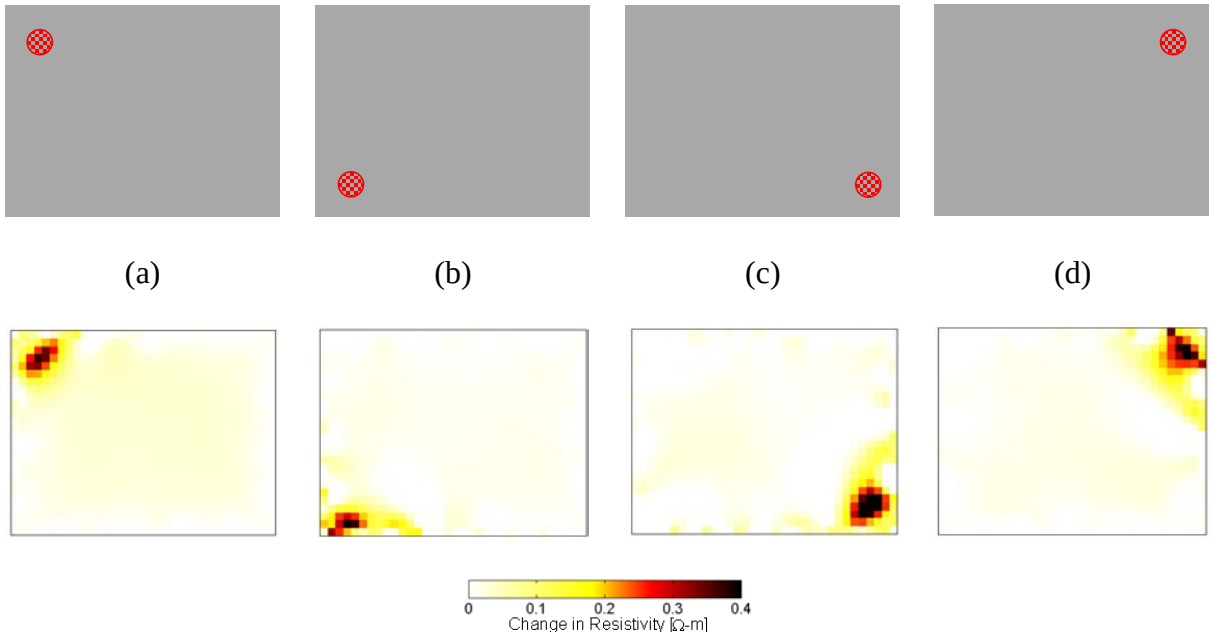

Figure 5.3 Localized pressure was applied to the fabric sensor near the (a) top-left, (b) bottom-left, (c) bottom-right, and (d) top-right corners. (e-f) Sparsity reconstruction obtained EIT resistivity maps corresponding to applied pressure at (a-d) locations, respectively.

was not recorded in this test, one could not back-calculate and compare estimated pressure with the actual applied pressure.

In addition to the single pressure point sensing tests, this study also sought to investigate the fabric sensor's ability to simultaneously capture multiple points of applied pressure. Here, two pressure points were applied on the fabric sensor at the same time, as depicted in Figures 5.4a to 5.4d; again, the applied pressure positions are highlighted by the red circles. The corresponding resistivity distributions, which were computed by solving the EIT inverse problem and subtracted from the baseline resistivity map and computed from the sparsity reconstruction algorithm, are shown in Figures 5.4e to 5.4h. Similar to the previous test results shown in Figure 5.3, the EIT resistivity maps show "highlighted spots" that corresponded to the locations of applied pressure.

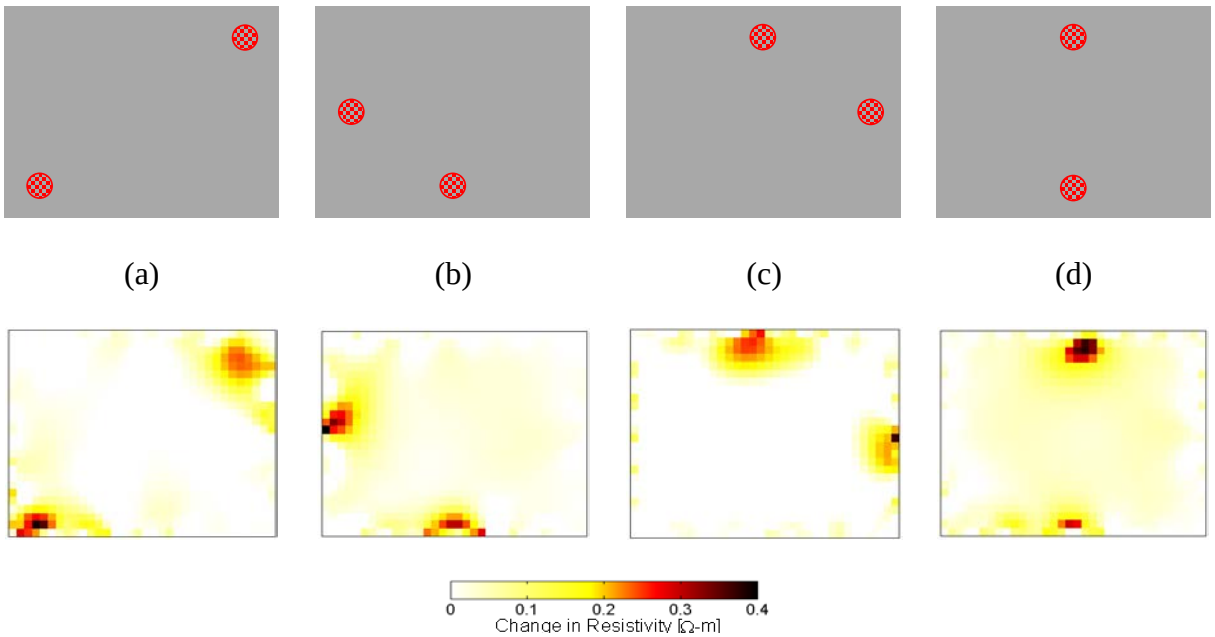

Figure 5.4 Localized pressure was applied at two points simultaneously at: (a) diagonal corners, (b) bottom and left edges, (c) top and right edges, and (d) top and bottom edges. (e-f) Sparsity reconstruction obtained EIT resistivity maps corresponding to applied pressure at (a-d) locations, respectively.

It can be observed that the proposed L_1-norm regularization algorithm could not only captured the applied pressure points simultaneously, but it also more accurately mapped the spatial pressure distributions than the conventional Tikhonov minimization (*i.e.*, L_2-minimization) (as was also found in Wang *et al.* [179]). These results confirm that the fabric sensors were capable of simultaneously resolving multiple externally applied pressure points. It should be noted that the two sets of experiment did not affect the integrity of the fabric sensor, which suggested that it was mechanically robust enough to undergo these deformations.

The second set of experiments sought to evaluate the fabric sensor's ability to capture impact-induced puncture damage. Thus, in this study, the fabric sensor was subjected to multiple punctures at different locations, and EIT analysis was conducted after the introduction of each damage scenario. Figures 5.5a to 5.5d show the schematic distributions of actual puncture damage on the fabric sensor specimen, where the damage locations are highlighted by red circles. Figures 5.5e to 5.5f show the corresponding EIT spatial resistivity maps, which were computed as the difference with respect to the undamaged baseline EIT map based on the sparsity regularization algorithm. These results clearly show that the multiple puncture holes were successfully detected and their locations identified, which correspond to the "highlighted spots" in the reconstructed images. Since punctures disconnected material locally, they created highly localized regions of high electrical resistivity (*i.e.*, theoretically infinite resistance and non-conductive). This localized increase in resistance was identified by the EIT-CS algorithm. However, the EIT algorithm would not be able to output an infinite resistivity, and the results appear smoothed to different extents near the vicinity of damage. The degree of smoothness and converged resistivity values would depend on the different inverse problem reconstruction algorithms employed. Theoretically, the L_1-norm regularization is capable of avoiding the over-smoothing effect that is inevitably

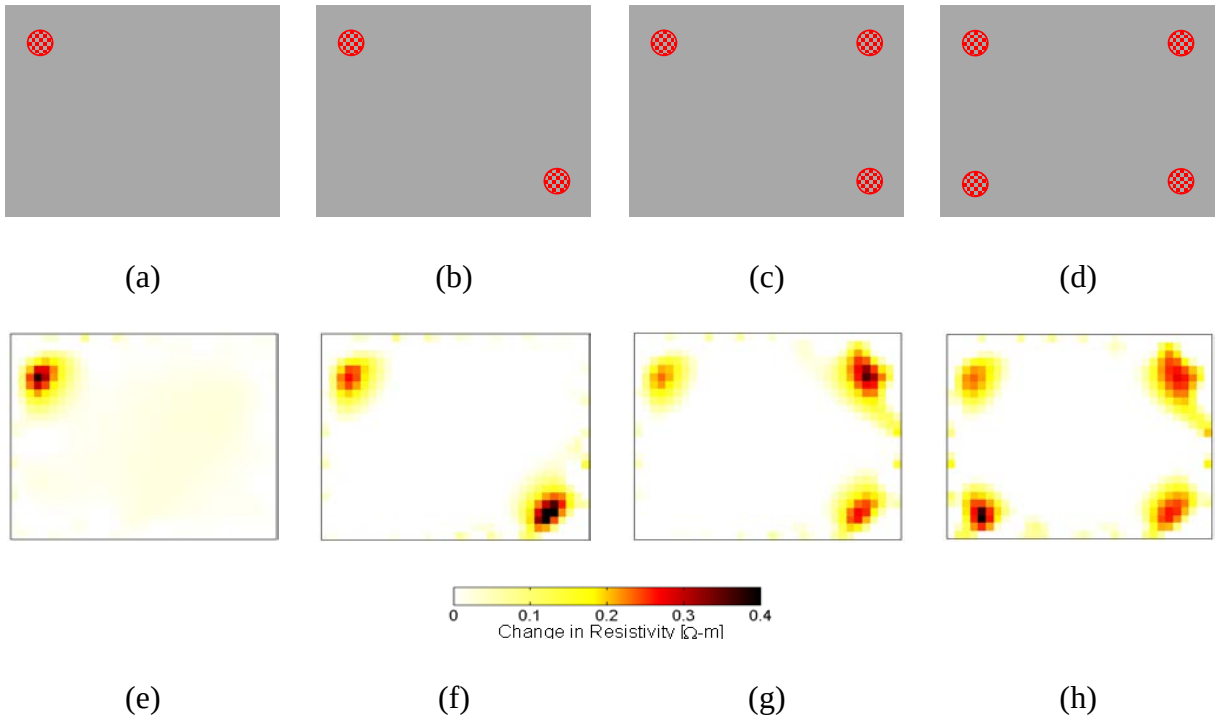

Figure 5.5 Puncture damage was introduced sequentially near the (a) top-left, (b) bottom-right, (c) top-right, and (d) bottom-left corners. (e-f) Sparsity reconstruction obtained EIT resistivity maps corresponding to (a-d) puncture damage cases are shown, respectively.

introduced by conventional Tikhonov regularization [181, 190-192, 194]. Further analysis on the smoothing effect on the EIT inverse problem reconstruction is provided in Section 5.4.3. Furthermore, in the context of practical applications, it is hypothesized that, as long as the boundary electrodes of the fabric sensors are not damaged, the coupled spatial sensing system should be able to detect and locate puncture damage that extend beyond just the four punctures demonstrated in this study.

5.3.3. Spatial resolution study

In addition to validating the spatial sensing capability of the coupled system, this section further investigated the resolution of the EIT inverse problem when using the sparsity

reconstruction versus Tikhonov reconstruction. As previously mentioned in Section 5.4.3, the L_1-norm regularization has demonstrated an improved reconstruction resolution as compared to the Tikhonov regularization (*i.e.*, L_2-norm) [179] based on observations of the computed resistivity maps. Particularly, to quantify and compare the resolutions of the inverse problem reconstruction, a resolution analysis was performed based on the puncture damage cases. In fact, Tikhonov regularization theoretically tends to heavily penalize the drastic change in electrical conductivity or resistivity (thus causing the over-smoothing effect). In contrast, the sparsity regularization penalizes all terms equally [190-192]. Thus, the puncture damage cases (*i.e.*, drastic changes in electrical property of the sensing element) are prime examples for demonstrating the over-smoothing effects induced by Tikhonov reconstruction and how sparsity reconstruction can be used to enhance reconstruction resolution and accuracy.

Here, the EIT reconstruction spatial resolution was evaluated based on pixel values of the reconstructed images. Particularly, the blur radius (*BR*) was used to quantify sensing resolution, which was defined and calculated as follows [195, 196]:

$$BR = \sqrt{\frac{A_R}{A_0}} \tag{5.17}$$

where A_0 is the total area of the domain of interest (*i.e.*, areas of the sensing films). A_R is the area that contains significant reconstructed changes that are larger than half of the maximum magnitude of the image pixel values, which can be expressed as

$$A_R = \sum_{i=1}^{N} A_i \ \ for\ all\ i\ that\ \delta\sigma_i \geq \frac{1}{2} max\ (\delta\sigma_i) \tag{5.18}$$

where *N* is the total number of pixels whose values are above the threshold. It can be seen from Equations 5.17 and 5.18 that smaller *BR* values indicate higher reconstruction resolution (*i.e.*, "highlighted spots" are more distinct and with less blurred features).

As previously mentioned, the resolution analysis in this Section was based on the experimental data on spatial puncture damage cases. Figure 5.6 shows a comparison of the *BR* values of EIT inverse problem reconstruction computed using Tikhonov and sparsity reconstruction algorithms, respectively. The chart clearly shows that the L_1-norm regularization was able to enhance the reconstruction resolution for all the damage cases, which was consistent with previous observations of the reconstructed resistivity maps.

5.4. Summary and Conclusions

In this chapter, as-fabricated piezoresistive nanocomposite thin films were coupled with imaging and signal processing techniques to achieve spatial sensing. The sensing strategy allowed

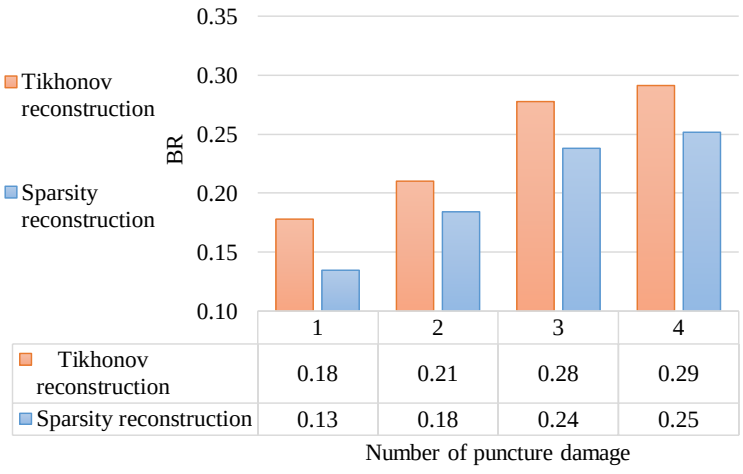

Figure 5.6 *BR* values of the EIT inverse problem reconstruction for all puncture damage cases computed with the Tikhonov and sparsity reconstruction algorithms, respectively.

one to interrogate and map the electrical property changes in the nanocomposite thin films by relying solely on the boundary voltage measurements, and the resulting resistivity maps enabled one to locate and visualize potential damage or abnormally high stress/strain distributions in the structure. In particular, this study employed an EIT measurement strategy and algorithm (which comprises the forward and inverse problems) to noninvasively characterize the electrical property distribution of strain-sensitive materials. One of the major challenges that this chapter aims to address was to develop a robust algorithm that could more accurately and efficiently solve the EIT inverse problem and generate high-resolution reconstruction maps. In particular, this study adopted a CS scheme and imposed L_1-norm regularization (computed using the TwIST algorithm) to leverage the prior information of spatial sparsity present in typical EIT problems.

Furthermore, this chapter conducted a set of experimental demonstrations for characterizing the spatial sensing performance of the nanocomposite-EIT coupled system. Specifically, fabric sensors with a set of boundary electrodes were designed and fabricated to be compatible with the EIT measurement scheme. During the experiments, the fabric sensors were subjected to locally applied pressure points (*i.e.*, nondestructive), as well as several impact-induced puncture damages (*i.e.*, destructive). The EIT-CS algorithm was employed to reconstruct the resistivity maps of the sensing films for each deformation and damage case. It was shown that the proposed spatial sensing system could successfully identify and locate the applied mechanical disturbance. In addition, a spatial resolution analysis verified that the sparsity reconstruction algorithm could effectively enhance the EIT inverse problem reconstruction resolution with respect to those solved by conventional Tikhonov reconstruction algorithm. Therefore, the L_1-norm regularization is recommended here for computing typical EIT inverse problem, and the remainder of this dissertation is mainly based on the sparsity reconstruction algorithm.

Furthermore, it should be noted that the EIT-CS algorithm was used to reconstruct conductivity/resistivity distribution change relative to the baseline distribution, rather than quantifying the absolute values of the conductivity/resistivity change. This was mainly because system errors (including computational errors and measurement noise) could be mostly avoided by subtracting the baseline distribution. Future work could focus on minimizing the system errors so that to reconstruct the absolute change in the sensing films' conductivity/resistivity, which could enable the spatial sensing systems to identify, locate, and quantify the change in structural mechanical performance. The quantified spatial mechanical response could potentially be used for updating physical models of corresponding structural components.

Overall, this chapter demonstrated that spatial sensing could be achieved by coupling the piezoresistive nanocomposite thin films with the EIT-CS algorithm. Due to the high-performance strain sensing materials manufactured in this study, there is promise for utilizing these coupled spatial sensing systems to more accurately characterize stress/strain distributions, whose detection based on conventional transducers may otherwise be compromised by system noise and errors. The following chapter will highlight the large-scale applications of these spatial sensing systems for monitoring the structural integrity of physical assets, as well as for assistive rehabilitation for amputated patients.

Chapter 6. Nanocomposite-Based Spatial Sensing Systems for Structural and Human Health Monitoring

6.1. Introduction

Chapters 2 and 3 introduced several design and manufacturing strategies for developing multifunctional nanocomposites, whose applications for monitoring human physiological performance was demonstrated in Chapter 4. To leverage the unique distributed sensing advantage of these nanocomposites, Chapter 5 introduced a coupled spatial sensing system for noninvasively interrogating the change in electrical properties of these nanocomposite sensors. Since the electrical response of these materials are pre-calibrated to applied strains, the results could be correlated to the mechanical (*i.e.*, strain and stress) performance of structures and their components.

The primary objective of this chapter is to demonstrate the relatively large-scale application of densely distributed sensing using nanocomposite sensors coupled with EIT. Specifically, this

chapter highlights two application scenarios. Fist, Section 6.2 demonstrates implementing the nanocomposites-based spatial sensing system to monitor and evaluate the structural integrity of a full-scale reinforced concrete shear wall that was subjected to cyclic lateral loads. Then, Section 6.3 discusses nanocomposite fabric sensor-based sensing systems for assistive rehabilitation and pressure ulcers prevention, particularly for lower-limb amputees fitted with socket prostheses.

6.2. Integrated Sensing System for Reinforced Concrete Shear Wall

6.2.1. Reinforced concrete shear wall health monitoring

Reinforced concrete shear walls (RCSWs) have been widely used for enhancing civil infrastructure ductility under seismic events as a means to improve infrastructure system safety [197-199]. However, their integrity can be compromised by multi-hazards-related extreme loads as well as long-term degradation. To ensure the RCSWs' structural reliability, in addition to conventional manual visual inspection of concrete cracks, various SHM and non-destructive evaluation (NDE) techniques have been proposed to more efficiently and accurately assess the condition of RCSWs. For instance, acoustic emission (AE) has unique advantages in monitoring the formation and propagation of cracks in RCSWs. In general, AE requires the implementation of an array of piezoelectric transducers on the structure to detect propagating stress waves released when concrete cracks. The features extracted from the detected AE signals (*e.g.*, peak amplitude, arrival time, and frequency, among others) can be used to evaluate structural integrity [197, 200, 201]. In addition, several integrated SHM techniques for monitoring concrete cracks have been developed by embedding the sensing devices in concrete structures, such as distributed fiber optic sensors [37, 202], piezoelectric ceramic-based smart aggregates [203, 204], and CNT-based sensors [205-207]. The embedded sensing approaches not only require transducers to be

sufficiently robust to survive the harsh construction conditions, but they also need to avoid (or minimize) disruption to the construction process and timeline.

Therefore, this study aims to demonstrate the potential of applying nanocomposite-based spatial sensing system for large-scale civil infrastructures and for monitoring their structural integrity. In particular, a full-scale RCSW was designed as a ductile structural component, which was subjected to under simulated seismic loading. To assist monitoring and evaluating RCSW integrity (*i.e.*, specifically, potential local damage development during the load tests), the CNT-based nanocomposite sensing skin was spray-coated onto the surface of the wall structure. The EIT-CS algorithm was employed to investigate structural damage-induced changes in the electrical property of the sensing skin.

6.2.2. Experimental setup and test procedures

Here, the RCSW was designed, constructed, and tested according to current design codes, and a detailed description can be found in Faraone *et al.* [208]. In short, the aspect ratio (*i.e.*, height-to-weight) of the wall specimen was 2, so that the slender wall is expected to exhibit flexure-dominated behavior (ASCE 7 2016 and ACI Committee 318 2014). Figures 6.1a and 6.1b show schematics of the experimental setup and a photograph of the east façade of the corresponding specimen, respectively. The RCSW was mounted on the strong floor through a reinforced concrete footing. Seismic loading was simulated by applying a combination of axial load (*i.e.*, dead load) and cyclic lateral load. Specifically, four post-tensioned rebars were used to apply a total axial load of 500 kips (2225 kN) from the top of the reinforced concrete load stub to the wall through two steel beams that were transversely installed on the load stub. The axial load was first applied to the wall and was maintained throughout the entire duration of the load test. In

addition, cyclic lateral load was generated using a horizontal hydraulic actuator, whose load and displacement capacities were 500 kips (2225 kN) and ± 24 in, respectively. One end of the actuator was installed on the strong wall, while the other end was attached to the left side (*i.e.*, south side) of the load stub, as shown in Figure 6.1. The construction of the RCSW and testing was performed in the Powell Labs at the University of California, San Diego.

The cyclic load test followed the displacement-controlled protocol suggest by ACI 374.2R-13 (ACI Committee 374 2013), and more details are described in Faraone *et al.* [208]. The actual experiment consisted of applying three load cycles, with each cycle set designed to induce 0.125%, 0.25%, 0.5%, 0.7%, and 1.0% drift; thereafter, two load cycles of 1.5%, 2.0%, and 2.5% drift each were applied. The test ended once the structure reached 3.0% drift, since significant reduction in load capacity was observed.

To characterize structural damage, visible concrete crack patterns were documented, and their widths were individually measured following each loading cycle. However, visual inspection can be subjective, labor-intensive, and fundamentally limited to identify potential subsurface damage. Therefore, this study mainly focused on employing the nanocomposite-based spatial sensing system (Chapter 5) to facilitate monitoring and evaluating wall integrity. One of the main objectives was to identify and locate seismic load-induced structural anomalies that were invisible to the naked eye. It was hypothesized that the high strain-sensing performance of the nanocomposite thin films could reveal the presence of micro-cracks and/or subtle changes in strain distributions as a result of subsurface concrete cracking. To enhance the sensing accuracy and sensitivity via relatively more direct stress/strain transfer from the structure to the sensing material, nanocomposite thin films were integrated with the reinforced concrete system by means of spray-coating the films directly onto the structure.

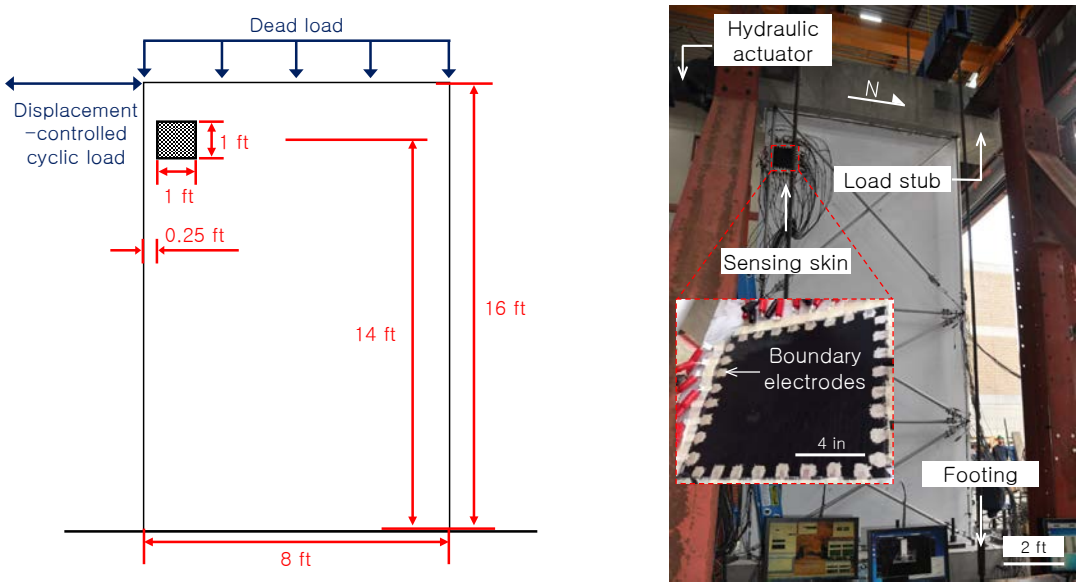

(a) (b)

Figure 6.1 (a) Schematics of the sensing skin implementation on the RCSW specimen and the simulated seismic load test setup. (b) A photograph of the east façade of the RCSW specimen. The inset shows a zoomed-in view of the spray-coated sensing skin with established boundary electrodes. (Note: 1 ft = 12 in = 304.8 mm)

However, it should be noted that it is generally challenging to perform *in situ* fabrication of nanomaterials at civil construction sites, mainly due to the required sophisticated material processing procedures, scalability of the fabrication techniques, and harsh construction environment. Thus, practical large-scale applications, especially in infrastructure monitoring, of nanomaterial-based sensors have been very limited to date. Therefore, another objective of this study was to demonstrate that robust and scalable manufacturing techniques (introduced in Chapter 2) are promising to break though the current "bottle neck" of real-life applications of multifunctional nanomaterials, especially for infrastructure health monitoring.

Specifically, prior to the load test, the CNT-based nanocomposite sensing skin was spray-coated onto the surface of the RCSW using an airbrush, forming a 12 × 12 in^2 (304.8 × 304.8 mm^2)

sensing domain, as shown in Figure 6.1. The spray-coated CNT-based ink was air-dried overnight. It should be noted that even though the structural surface was rough and vertical (in addition to limited accessible space during construction), the nanocomposite-based sensing system was successfully implemented without disturbing the construction process. To couple the sensing skin with the EIT measurement strategy, 8 × 8 electrodes were established along the boundaries of the coating using aluminum tape and conductive silver paint. Here, aluminum tape was used to improve signal quality, since they are more resistant to oxidation than copper. The electrodes were then extended and connected to the EIT DAQ system (Chapter 5) via coaxial cables to avoid signals being corrupted by environmental electromagnetic noise. Overall, the entire coating and specimen preparation process indicated that the spray-coating technique was robust and compatible with such large-scale applications.

Prior to testing, an EIT boundary voltage dataset was acquired to establish the global undamaged baseline of the coating (and RCSW structure). This baseline corresponded to the case when axial loads were imposed on the structure, but no lateral loading was applied to the RCSW structure yet. During testing, boundary voltages were acquired at the end of each load cycle.

6.2.3. Local structural performance monitoring

The seismic load test induced buckling and fracturing of boundary longitudinal rebars in the wall specimen at the finally applied 3.0% drift case, which led to ~ 20% reduction in its load capacity. Ultimately, the RCSW failed in flexure (as expected from initial design) and exhibited a residual drift of 0.7 in (18 mm) in the southern direction. Figure 6.2a shows a photograph of the east façade of the RCSW (sensing skin side) at the completion of the load test. The visible damage formation and propagation was analyzed by documenting the concrete crack patterns and

measuring the crack widths using linear potentiometers. More details about the crack damage evaluation can be found in Faraone *et al.* [208]. The highest visible concrete crack developed at ~ 160 in (4.064 m) from the top surface of the reinforced concrete footing, which was slightly below the location of the spray-coated sensing skin. Figure 6.2b shows a zoomed-in photograph of the sensing skin and its vicinity at the conclusion of the load test. It can be observed that the sensing skin remained intact (*i.e.*, no visible concrete cracks occurred in the sensing domain).

As mentioned earlier, the structural performance at the sensing skin location was further investigated using the coupled spatial sensing system. Specifically, the boundary voltage measurements were used as inputs to the EIT-CS algorithm to compute the electrical resistivity distribution of the sensing skin. The cyclic lateral load-induced changes in resistivity distribution were obtained by subtracting the results with the global baseline resistivity distribution of the sensing skin (*i.e.*, the undamaged case), which was acquired prior to the start of testing. Figure 6.3 shows the reconstructed maps of changes in resistivity distribution corresponding to applied drifts of different magnitudes. One can observe that there was a highlighted spot at the bottom left corner of the sensing domain, and it became increasingly more obvious (*i.e.*, change in resistivity increased) as larger drifts were applied to the RCSW specimen. Since the nanocomposite thin film was directly integrated with the concrete, the change in stress/strain distribution at the corresponding region could disrupt the electrical resistivity distribution of the piezoresistive nanocomposite thin film, forming anomalous features in the resistivity maps. Therefore, it was hypothesized that the captured local highlighted spot (*i.e.*, anomaly) was potentially caused by irreversible stress/strain concentration developed at that specific location during the load test.

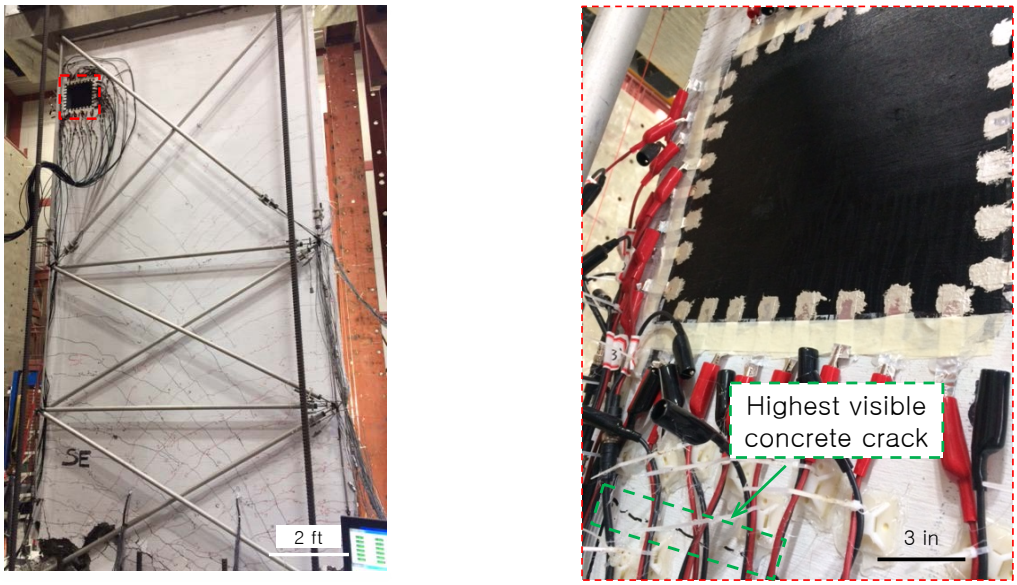

(a) (b)

Figure 6.2 (a) A photograph of the east façade of the RCSW specimen at the completion of the load test. (b) A zoomed-in view of the sensing domain and its vicinity (highlighted in the red dashed box in (a)), where the highest visible concrete crack was highlighted in the green dashed box. (Note: 1 ft = 12 in = 304.8 mm)

These results indicate that the coupled spatial sensing system could potentially capture anomalies in structural behavior and damage that may be hidden from visual inspection. In addition, since it is well known that irreversible stress/strain concentration in structural components could potentially lead to structural damage, this study successfully demonstrated an example for which the integrated sensing system could help guide further structural inspection on regions with suspected damage.

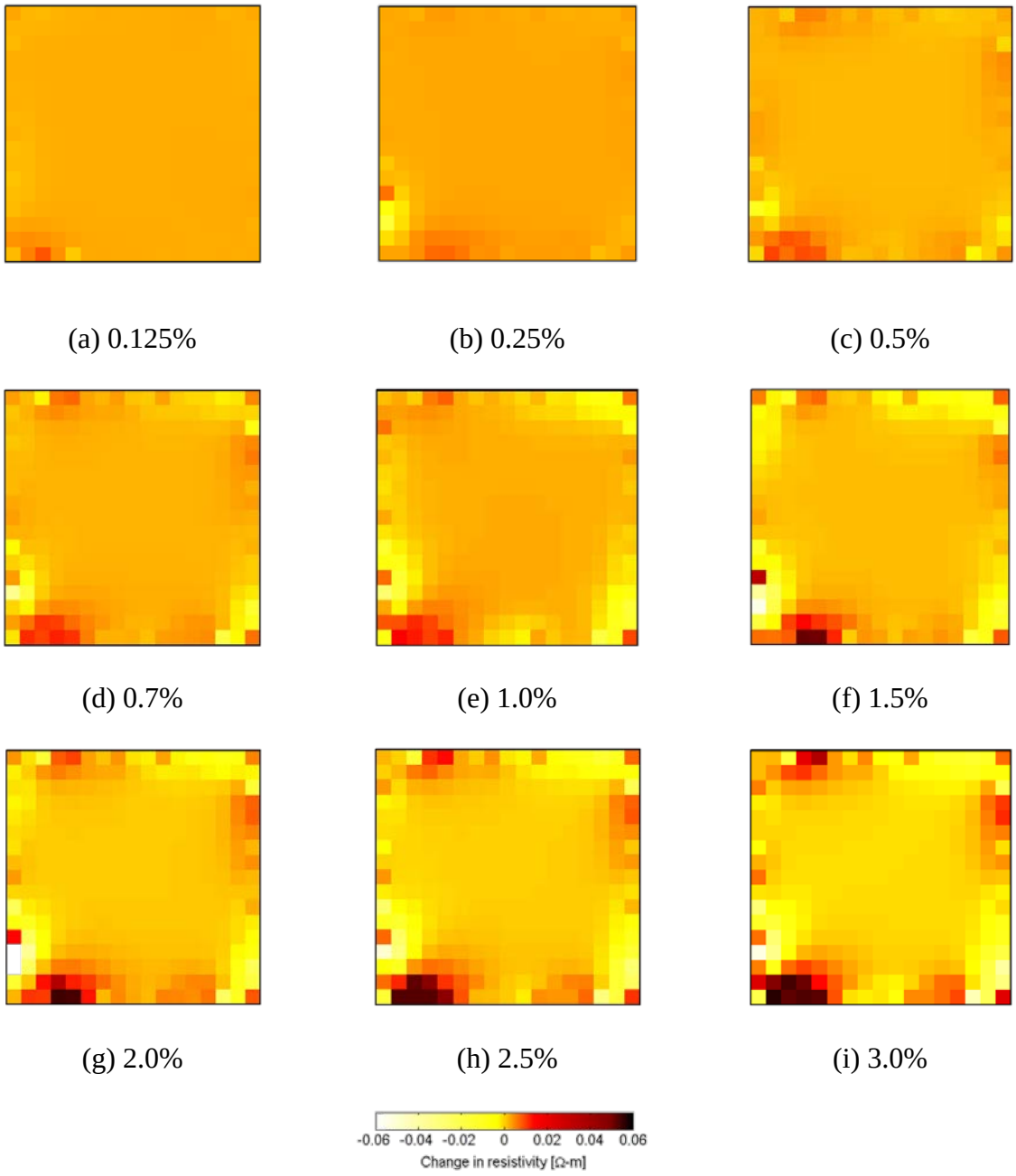

Figure 6.3 (a – i) EIT-CS algorithm reconstructed changes in resistivity distribution of the nanocomposite sensing skin corresponding to different drifts of the RCSW specimen.

6.2.4. Summary and conclusions

This section focused on demonstrating the scalability of the nanocomposite-based spatial sensing system for monitoring the health of large-scale civil infrastructures through a collaborative

effort on testing a full-scale RCSW specimen. Here, the CNT-based nanocomposite sensing skin was directly spray-coated onto a portion of the RCSW specimen. The RCSW was then subjected to simulated seismic loading, while distributed strain measurements were acquired using the sensing skin and a customized EIT DAQ system. The EIT-CS algorithm was employed to interrogate the structural integrity of a region of the RCSW by computing the resistivity distribution of the sensing skin corresponding to different drift ratios (or damage states). Based on the EIT results obtained from this study, the spatial sensing system was successfully validated for its ability to detect and locate anomalies or damage in the structure caused by cyclic loading, which could facilitate a more detailed structural integrity inspection thereafter. Another major finding of this study was that the spray-coating manufacturing technique employed was scalable and compatible with *in-situ* implementation at a construction site. Overall, the manufacturing technique and sensing methodology gives promise for utilizing functional nanomaterials for civil infrastructure and structural health monitoring applications.

Future work will compare the sensing results with theoretical structural responses characterized by finite element analysis, specifically, of the stress/strain distribution in the vicinity of the sensing domain. This study was a preliminary step towards employing high-performance multifunctional materials for large-scale integrated infrastructure sensing. However, it should be noted that, considering system implementation costs, signal processing complexities, and data relevance, it might be sufficient and more efficient to implement these multifunctional materials-based sensing system only at critical and/or damage susceptible structural components, which could be determined *a priori* through numerical modeling.

6.3. Smart Socket Prostheses and Pressure Ulcers Prevention

Similar to the infrastructure systems, human body can also be considered as a mechanical system. However, since human biomechanical system is highly flexible, conventional bulky transducers, which are designed for rigid structures, are fundamentally challenged to accurately and non-intrusively monitor human performance. Therefore, this section aims to implement the flexible spatial sensing system to monitor human body and engineered structures interactions. In particular, the target application is assisting amputee rehabilitation with pressure-sensing smart socket prostheses.

6.3.1. Socket prostheses

Hundreds of thousands of people each year undergo limb amputation as a result of either traumatic injury or peripheral vascular disease [209]. In the United States, for instance, there are approximately 84,500 to 114,000 amputation cases per year [210, 211]. This number is expected to be increasing due to the increase in the aging population and as diseases such as diabetes continue to grow.

To help the patient regain physical mobility post-amputation, a prosthesis, which consists of a socket, a shank, the ankle, and foot (*i.e.*, for lower-limb amputees), is prescribed to replace the removed limb [212, 213]. The socket is responsible for coupling the residual limb (or stump) with the rest of the components of the prosthesis. One of the most challenging procedure for a prosthetist is to design a customized socket due to the uniqueness of each patient's residual limb [213]. Even though the socket is customized, lower-limb amputees (~ 75% of them) still often experience problems related to pressure ulcer due to the lengthy and repetitive mechanical perturbation applied by the socket [214, 215].

Pressure ulcers refer to the tissue breakdown in localized regions in the skin and/or underlying tissue, where prolonged mechanical loading prevents healthy capillary flow [209, 216]. Studies have shown that the prevalence of pressure ulcers ranges from 8% to 23%, depending on the subject group being studied [209]. In addition, pressure ulcers are usually painful, difficult and expensive to treat, and can potentially lead to re-amputation in serious cases. As a consequence, pressure ulcers significantly threaten the physical and financial health of these amputees, not to mention that these issues place a considerable burden on the global healthcare system. For instance, the annual cost for pressure ulcer care in the U.S. exceeds ~$11 billion, with individual costs amounting to as much as $70,000 for each ulcer diagnosed.

Pressure ulcers can develop both on the superficial skin layers and in the deep tissue, depending how the skin and tissue are loaded. In particular, superficial ulcers are predominantly caused by shear stresses acting on the skin layers, while deep ulcers are mainly due to long-lasting compression of tissue in bony body parts [217, 218]. Previous studies showed that the measured interfacial pressure and shear stress in a prosthesis are 415 kPa and 65 kPa, respectively [219, 220]. For reference, only 8 kPa pressure is large enough to hinder skin blood flow [221], which explains the prevalence of these pressure ulcers. It should be noted that deep ulcers can develop at a faster rate than superficial ones, forming large areas of ulceration. In addition, deep ulcers are inherently difficult to be identified and can be easily ignored until they become visible and too late to be treated, which makes them the most severe ulcers. Therefore, when it comes to pressure ulcer care, prevention is remarkably cheaper and more efficient than current forms of treatments [209].

One of the common approaches to determine ulcer condition is by visual and physical inspection [209]. However, the assessment results are highly subjective relative to the experience of clinicians. Besides, visual inspection is usually ineffective for diagnosing deep ulcers at early

stages. On the other hand, various imaging techniques have been applied for better assessing pressure ulcers. For instance, X-ray can determine ulcer status by injecting contrast media into the wound. B-mode ultrasonography is a noninvasive method for imaging both the surface and embedded necrotic tissues through scanning the inspection probe across the wound while recording the corresponding images [222]. Although these imaging techniques provide an accurate qualitative assessment, they usually require specific imaging systems that can only be operated by clinicians in a controlled environment.

On the other hand, many endeavors have been undertaken to implement sensing devices onto prostheses to monitor pressure generated at the interface. For example, a network of strain transducers can be integrated in the socket [213], so as to measure the pressure distribution in the socket, which can provide valuable information for socket design as well as for identifying abnormal pressure locations and “hot spots”. However, conventional transducers are discrete devices, which makes them inefficient and inaccurate for mapping the pressure distribution over large areas. In addition, large quantities of those rigid transducers integrated in the socket can lead to user discomfort.

In this work, a next-generation socket prosthesis design was considered and is shown in Figure 6.4a. It has two main components, which are the composite strips (covered by fabric) on the periphery and a socket base at the bottom. Figure 6.4b shows the top and bottom views of the socket base structure, and it can be seen that its top surface is similar to the side of a truncated cone. First, a piezoresistive CNT-based fabric sensor was designed to conform to the surfaces of the composite strips and socket base. Second, the sensor was interrogated at its boundaries, and the raw data was used in conjunction with an EIT algorithm for achieving distributed pressure

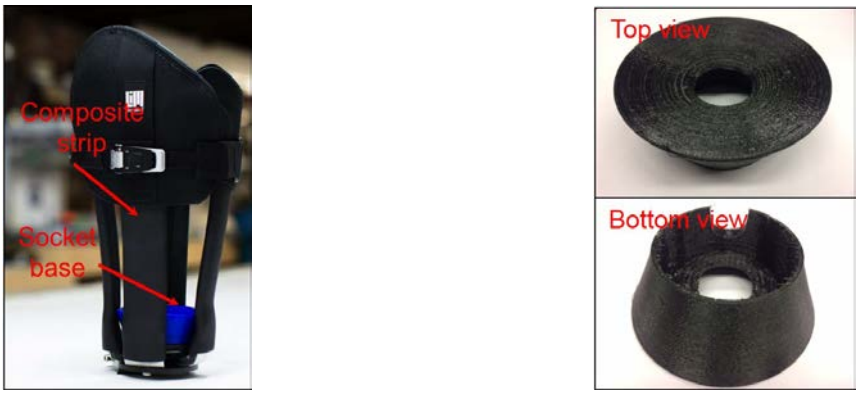

(a) (b)

Figure 6.4 (a) A picture of a next-generation prosthetic socket as well as the (b) top and bottom views of the socket base are shown.

mapping. Then, the strain sensing and pressure mapping performance of the fabric sensors were characterized.

6.3.2. Spatial pressure distribution monitoring

Here, to demonstrate the fabric sensors' potential for monitoring pressure distributions on different components in the socket prosthesis, the fabric sensors were shaped to form a 2D, thin, rectangular strip (Figures 6.5a and 6.5c) and a 3D truncated cone (Figures 6.5b and 6.5d), which were designed to fit the geometry of the composite strip and the socket base, respectively. This shows the advantage of the fabric sensor design, which allows one to readily customize the shapes and dimensions of the sensing materials.

To realize distributed pressure sensing, the fabric sensors were used in conjunction with an EIT measurement strategy and algorithm. Here, a Keithley 6221 current generator was utilized to inject 1 mA of DC across a preselected pair of boundary electrodes. To automatically switch the pair of electrodes for injecting a different DC excitation pattern, the current generator was

interfaced with a Keysight 34980A multifunctional switch, which was controlled using a customized Matlab program. Furthermore, the switch includes a built-in DMM that could measure and record voltages that develop between the other pairs of electrodes. The entire set of voltage measurements were then used as inputs to the EIT algorithm for reconstructing the fabric sensor's conductivity (or resistivity) distribution.

Prior to conducting the distributed pressure sensing tests, the EIT DAQ system was commanded to obtain an initial set of boundary voltage measurements when the fabric sensors were in their undeformed state (*i.e.*, baseline). Thereafter, the fabric sensor strip was first tested by pressing the fabric sensor, using fingers, at different points along the entire strip. The goal was to simulate abnormally high pressure points on the amputee's residual limb, potentially either due to inappropriate design/fitment or physical changes of the residual limb itself over time. Similarly,

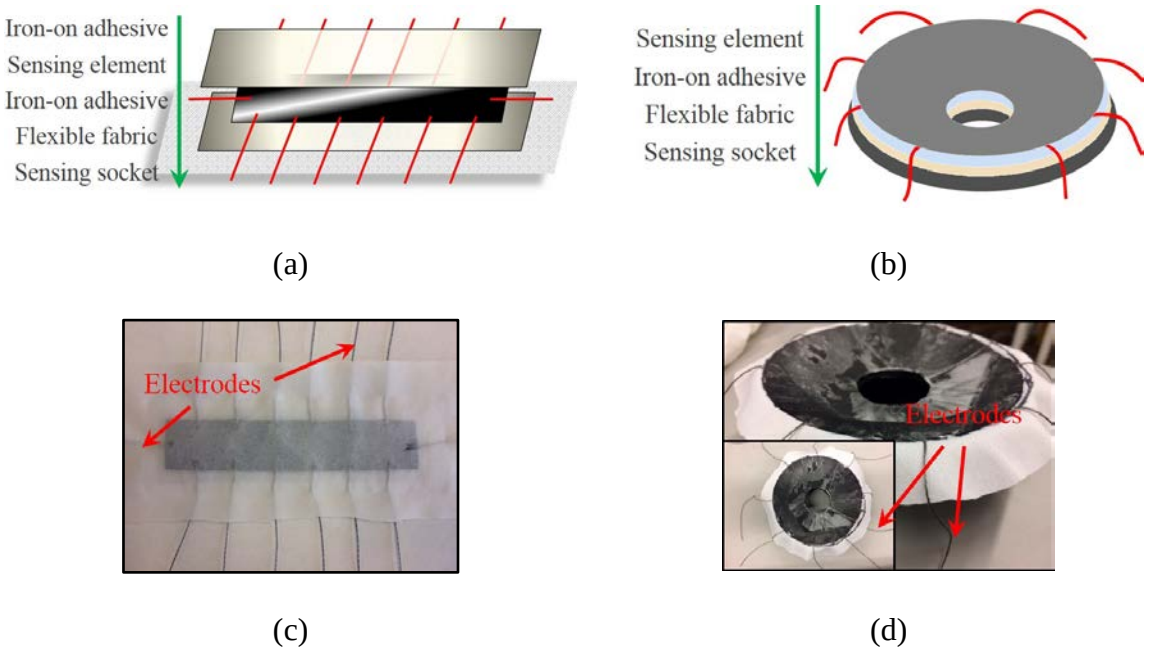

Figure 6.5 (a) Fabric sensors had a laminated structure and (b) were cut to different shapes and integrated with fabric substrate. Fabric sensors were prepared to form (c) a rectangular strip and (d) to conform to the socket base.

the socket base with the fabric sensor was subjected to applied localized pressure points by pressing the top surface of the socket base and fabric sensor (Figure 6.6). For each case, the EIT DAQ system collected the corresponding boundary voltage measurements.

The fabric sensor strip was first subjected to localized pressure sensing tests. Figure 6.7 shows the pictures of where the pressure points were applied to the fabric sensor strip (left column), as well as the corresponding EIT reconstructed resistivity maps (right column). It should be noted that these EIT results show changes in resistivity of the deformed state with respect to its undeformed baseline. According to the color bar, darker colors refer to larger increases in resistivity. Since the fabric sensor strip was only locally deformed, each EIT reconstruction result of Figure 6.7 shows a distinct highlighted spot (*i.e.*, localized increase in resistivity) at the vicinity where the specimen was pressed. In addition, the fabric sensor strip was subjected to multiple pressure points at different locations. Figure 6.8 shows the photographs of introduced pressure points (left column) and their corresponding reconstructed resistivity maps of the sensing fabric (right column). It was found that the fabric sensor could locate the pressure points with relatively high accuracy across the entire strip.

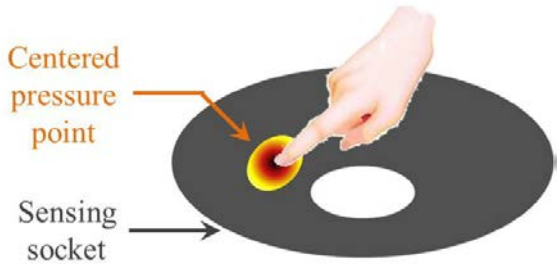

Figure 6.6 Localized pressure was applied to the fabric sensor on the socket base.

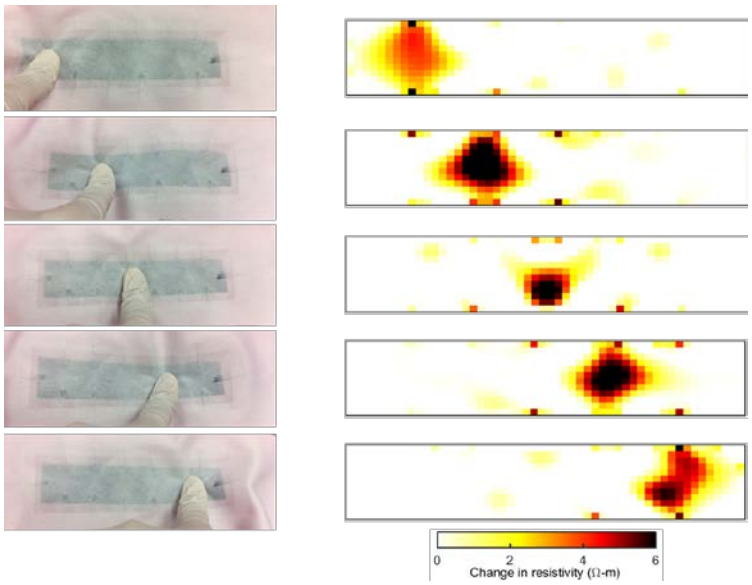

Figure 6.8 The EIT reconstruction results of the fabric sensor strip when it was subjected to localized pressure points applied at different locations are shown side-by-side.

Next, the socket base with the fabric sensor was fabricated and tested for sensing distributed pressure along its 3D surface. Similar to the fabric sensor strips, the socket base with the fabric sensor was subjected to applied concentrated pressure points at multiple locations. Figure 6.9 presents the EIT resistivity images of the socket base after it was deformed by manually

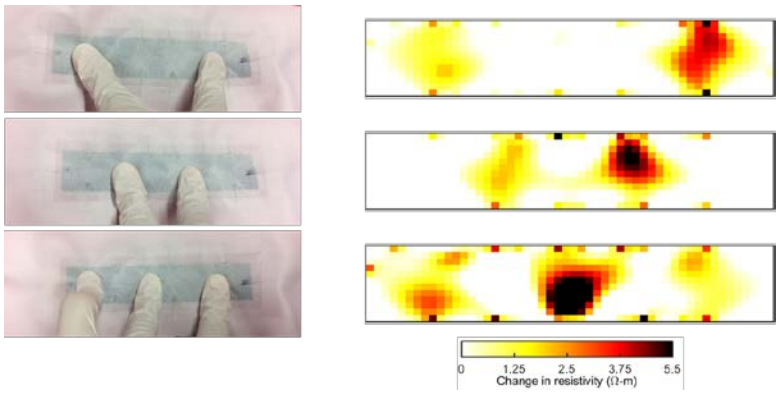

Figure 6.7 The EIT reconstruction results of the fabric sensor strip when it was subjected to multiple localized pressure points applied at different locations are shown side-by-side.

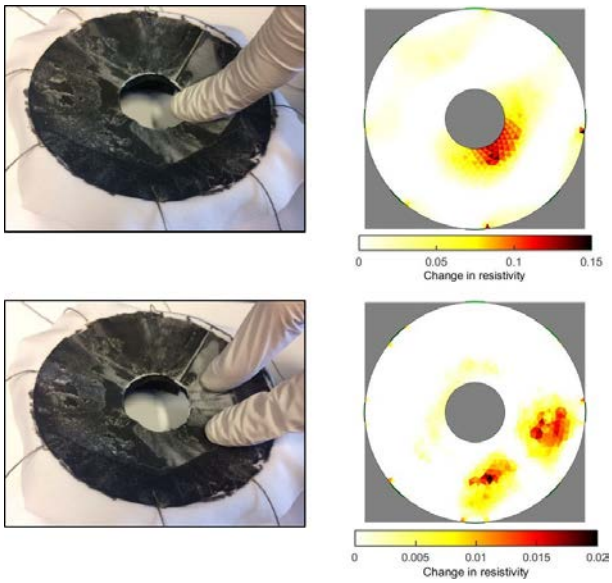

Figure 6.9 The socket base and fabric sensor was subjected to localized pressure points, and the corresponding EIT reconstructed pressure distributions successfully identified the localized pressure point(s).

pressing at different locations (left column). The corresponding resistivity maps (right column) are also shown in Figure 6.9; again, these EIT results show the changes in resistivity distribution with respect to its undeformed baseline. Overall, these results confirmed that pressure hot spots could be detected effectively and accurately. These results validated that the CNT-based fabric sensors could be integrated with next-generation smart socket prostheses for distributed pressure sensing.

6.3.3. Summary and conclusions

In this section, fabric sensors were designed and employed for monitoring distributed contact pressure along the interior surface of socket prostheses as a means to monitor an amputee's residual limb health and to prevent pressure ulcer formation. To achieve spatial sensing and to leverage the unique feature that every location of the entire sensing films is sensitive to strains (or equivalently pressure), the fabric sensors were coupled with the EIT-CS algorithm. Furthermore, this study performed preliminary pressure distribution sensing tests on the fabric sensor strip and

the sensing socket base by applying pressure at different locations so as to simulate the possible interactions between an amputee's residual limb and the socket prosthesis. It was found that the EIT resistivity maps captured localized increases in resistance at regions where pressure was applied. Therefore, this work demonstrated that the fabric sensors could be customized to conform to complex geometries and be implemented with socket prostheses for distributed pressure sensing and pressure ulcer prevention.

Chapter 6, in part, is a reprint of the material as it appears in Nanocomposite Fabric Sensors for Socket Prostheses, L. Wang and K. J. Loh, 2018. The dissertation author was the primary investigator and author of these papers.

Chapter 7. Conclusions

7.1. Summary of Results

This primary objective of this dissertation was to develop, characterize, and implement nanocomposite-based sensing systems for structural health and human performance monitoring. This work aimed to overcome some of the current challenges for implementing multifunctional materials in a practical manner so as to pave the way for the next-generation of more robustly integrated sensing systems for acquiring high-quality data on structural and human performance.

In Chapter 2, three different bottom-up manufacturing techniques were introduced to fabricate the CNT- and GNS-based nanocomposite thin films. Each fabrication technique featured unique advantages. To be specific, spray-coated CNT-based nanocomposites could be readily implemented on large-scale structures, either directly on structural surfaces or embedded in the structural materials (*e.g.*, concrete and composites). Screen-printed GNS-based nanocomposites could be rapidly patterned to form large-scale thin films and be well integrated with porous substrate materials (*e.g.*, fabrics and paper). On the other hand, micro-patterning was advantageous in printing nanomaterial-based inks on various substrates with high-precision (*i.e.*, microscale) and could potentially enable automatic multi-material patterning. The effectiveness of these

manufacturing techniques was evaluated by investigating the microstructures of the resulting nanocomposites, which showed that the CNTs and GNS could be uniformly dispersed in the polymeric matrices.

In addition, Chapter 2 also performed a series of cyclic load tests to investigate the strain sensing performance of the designed nanocomposites. It was found that these nanocomposite thin films were piezoresistive and exhibited stable and repeatable strain sensing response. As compared with commercial metal foil strain gages, the manufactured nanocomposites possessed superior strain sensitivity and a much larger measurable strain range. For instance, screen-printed GNS-based sensors were ~ 37 times more sensitive when $\varepsilon \geq 10\%$, and the micro-patterned GNS-based sensors were ~ 10 times more sensitive when $\varepsilon \leq 10\%$).

However, the manufacturing processes were empirically optimized for each material system so as to obtain the optimal fabrication efficiency and piezoresistive properties. This process is commonly involved when developing functional materials. To develop a more universally applicable material engineering methodology that can predictably encode material properties for desired applications and to bring these nanocomposites one step closer to field implementations, Chapter 3 proposed a topological design-based approach to strategically manipulate nanocomposite strain sensing properties. This approach was investigated based on the GNS- and CNT-based nanocomposite thin films that were fabricated in Chapter 2. It was found from the load tests that, regardless of the nanocomposite material systems, inhomogeneous topology-induced stress concentrations could enhance bulk film piezoresistive response, which could facilitate designing high-sensitivity strain sensors. On the other hand, stress releasing topologies (*i.e.*, Kirigami-based structures in this study) were shown to be promising for decoupling sensing signals induced by strains/deformation from the primary desirable measurand (*e.g.*, temperature-induced

resistance changes). Furthermore, in Chapter 3, numerical analyses were conducted to characterize the electromechanical responses of the patterned nanocomposites. To be specific, a linear piezoresistive material model and a statistical nonlinear material model were employed. Both material models were first calibrated using experimental data on the strain sensing response of the Non-Patterned control set specimens. Then, the calibrated materials models were implemented to simulate the electromechanical responses of the patterned samples. It was found that both models showed similar effects of topological designs on the nanocomposite's piezoresistivity that were consistent with experimental characterization results, and the nonlinear material models could more accurately match the experimental findings.

Chapter 4 implemented CNT- and GNS-based nanocomposites as discrete strain sensing elements to validate their applications for monitoring human physiological performance. To be specific, CNT-based fabric sensors were designed to first detect finger bending movements as a proof-of-concept demonstration for human motion monitoring, which exhibited relatively stable response. Then, a smart chest band was designed based on the fabric sensors for monitoring respiration. In addition, a PGS was developed to form sensing skins that featured high flexibility and conformability, which could be readily adhered to or detached from the skin. The PGS was demonstrated to be capable of quantifying finger bending motions, identifying hand motion patterns, monitoring eye blinking, and capturing radial pulse signals.

However, since Chapter 4 only employed the designed nanocomposites as discrete sensing elements, Chapter 5 designed spatial sensing systems by coupling the piezoresistive nanocomposite thin films with EIT and CS algorithms. The main purpose of marrying EIT with thin film strain sensors was to overcome a major limitation of current sensing technologies, which is discrete sensing. Here, to enhance the EIT reconstruction resolution, a CS scheme was adopted

to leverage prior information of spatial sparsity present in typical EIT problems. To validate the spatial sensing capability of the coupled system, Chapter 5 conducted a series of distributed pressure and impact damage sensing tests based on fabric sensors. It was found that the spatial sensing system could successfully identify and locate applied pressure points as well as puncture damages. In addition, the resolution analysis demonstrated that the L_1-norm regularization algorithm was capable of more accurately solving EIT inverse problem than conventional Tikhonov regularization.

Building on Chapter 5, Chapter 6 mainly employed the coupled spatial sensing systems for large-scale structural and human health monitoring applications. To be specific, in the first demonstration scenario, a CNT-based nanocomposite thin film was spray-coated onto the surface of a full-scale reinforced-concrete shear wall specimen. This work showed that the spray-coating manufacturing technique was scalable and compatible with *in situ* implementation at a construction site. During the simulated seismic loading tests, the nanocomposite-based sensing system was employed to monitor structural integrity of its instrumented region on the RCSW specimen. The computed EIT results could detect and locate anomalies or damage in the structure caused by cyclic loading. Furthermore, another major target application in Chapter 6 focused on implementing the fabric sensor-based spatial sensing system on socket prostheses for monitoring pressure distributions on the interface between an amputee's residual limb and the socket structure. Here, the shapes and dimensions of the fabric sensors could be readily customized to be applied on different components of the socket without causing user discomfort. It was found that the EIT resistivity maps could identify and locate regions with high pressure hot spots.

7.2. Contributions and Future Work

As the first stage of SHM paradigm, sensor-based data acquisition systems directly define the capability, cost, and practical applicability of SHM systems for different structures. While various off-the-shelf sensing devices have currently been employed for SHM, the pressing demands for more robust sensing capabilities has motivated extensive efforts dedicated to developing innovative sensing techniques. As discussed in Chapter 1, one of the most promising approaches is by leveraging the unique properties of nanostructured materials for designing high-performance sensing materials. One of the grand challenges for implementing the nanomaterials for real-life applications is associated with how current methods frequently require sophisticated manufacturing techniques and have poor scalability.

Hence, one of the major contributions of this dissertation was the development of high-performance nanocomposite-based sensing systems by leveraging and optimizing simple, scalable, and low-cost manufacturing techniques. This work demonstrated that the designed nanocomposites not only possessed superior strain sensing performance as compared to commercial strain gages, but they were also compatible with large-scale applications, ranging from integrated infrastructure sensing to wearable sensors for smart socket prostheses. Based on these manufacturing techniques, future work will focus on designing multi-modal sensing materials that are sensitive to multiple structural performance parameters (*e.g.*, pH and temperature), in addition to stress and strains. The goal is to more comprehensively evaluate multiple aspects of structural health using a single integrated sensing system.

In addition, to overcome the discrete sensing limitation of current transducers, this dissertation coupled nanocomposite thin films with EIT and CS algorithms to realize spatial

sensing. From a computational perspective, the major challenge is to accurately and efficiently solve the EIT inverse problem and generate high-resolution reconstructed conductivity maps. Tikhonov regularization (*i.e.*, L_2-norm) is commonly used to solve the inverse problem, which generally introduces over-smoothing effects and compromises reconstruction resolution and accuracy. This dissertation adopted the CS scheme and imposed L_1-norm regularization (computed using the TwIST algorithm) to leverage prior information of spatial sparsity present in typical EIT problems. The experimental results demonstrated that the sparsity reconstruction algorithm effectively enhanced the EIT inverse problem reconstruction resolution. Thus, this dissertation recommended the L_1-norm regularization for solving the EIT inverse problem.

Furthermore, in the context of developing functional materials, current approaches mainly focus on engineering the material system by means of trial-and-error. In addition, these approaches typically designed different material systems for specific target applications, which could barely take advantage of the potential multifunctionality of these nanocomposites. To overcome these limitations, this dissertation contributed an innovative material property engineering methodology. To be specific, this dissertation experimentally demonstrated that, by solely changing the thin films' topologies, the strain sensitivity ranges of the GNS- and CNT-based nanocomposites could be significantly expanded to − 99% to + 50% and − 95% to + 70% as compared to their corresponding Non-Patterned control sets, respectively. Besides, the experimental findings were mostly consistent with numerically simulated electromechanical responses. These results indicated that the piezoresistivity of the nanocomposite thin films could be effectively manipulated by designing their topologies (in addition to tuning their nanomaterial constituents). Future work will improve the accuracy of the numerical material models to better simulate the experimentally measured nanocomposites' strain sensing responses. The topological design approach will also be

further validated for other piezoresistive nanocomposite material systems.

Overall, this dissertation demonstrated a step towards achieving next-generation multifunctional material-based sensing systems for monitoring engineered structures and human health. While the capability of these sensing systems needs to be further validated in more complex and practical application scenarios, this study validated remarkable potentials of these nanocomposite sensing materials for acquiring high-quality data related to structural and human performances. In addition, the multifunctional material-based spatial sensing systems provide previously unavailable data streams, which can potentially motivate more advanced developments in data analytics and risk assessment tools that support both SHM and human health assessment.

References

[1] Grandt Jr A F 2003 *Fundamentals of structural integrity: damage tolerant design and nondestructive evaluation*John Wiley & Sons

[2] Lynch J P, Farrar C R, Michaels J E 2016 Structural health monitoring: technological advances to practical implementations [scanning the issue] *Proceedings of the IEEE* **104** 1508-1512

[3] Frangopol D M, Curley J P 1987 Effects of damage and redundancy on structural reliability *Journal of structural engineering* **113** 1533-1549

[4] Farrar C R, Worden K 2006 An introduction to structural health monitoring *Philosophical Transactions of the Royal Society A: Mathematical, Physical and Engineering Sciences* **365** 303-315

[5] Becerik-Gerber B, Siddiqui M K, Brilakis I, El-Anwar O, El-Gohary N, Mahfouz T, Jog G M, Li S, Kandil A A 2013 Civil engineering grand challenges: Opportunities for data sensing, information analysis, and knowledge discovery *Journal of Computing in Civil Engineering* **28** 04014013

[6] Chang P C, Flatau A, Liu S 2003 Health monitoring of civil infrastructure *Structural Health Monitoring* **2** 257-267

[7] Chakrabarti M. (2018). *Aging Gas Pipelines: The Dangers Of Outdated Infrastructure Around The U.S.* Available: https://www.wbur.org/onpoint/2018/11/15/natural-gas-explosions-pipelines-infrastructure

[8] Kelly J. (2017). *Look out below: Danger lurks underground from aging gas pipes*. Available: https://www.usatoday.com/story/news/nation/2014/09/23/gas-pipes-cast-iron-deaths-explosions-investigation/15783697/

[9] (2019). *Oroville Dam crisis*. Available: https://en.wikipedia.org/wiki/Oroville_Dam_crisis

[10] Chavez N, Simon D. (2019). *California's Oroville Dam spillway is facing its first big test since it collapsed two years ago*. Available: https://www.cnn.com/2019/04/02/us/california-oroville-dam-opens/index.html

[11] (2019). *Ponte Morandi*. Available: https://en.wikipedia.org/wiki/Ponte_Morandi

[12] Giles L. (2018). *What Caused the Genoa Bridge Collapse?* Available: https://www.constructionequipmentguide.com/what-caused-the-genoa-bridge-collapse/41781

[13] (2019). *1994 Northridge earthquake*. Available: https://en.wikipedia.org/wiki/Ponte_Morandi

[14] Adam S. (2019). *2018's Billion Dollar Disasters in Context*. Available: https://www.climate.gov/news-features/blogs/beyond-data/2018s-billion-dollar-disasters-context

[15] Dolan A H, Walker I J 2006 Understanding vulnerability of coastal communities to climate change related risks *Journal of Coastal Research* 1316-1323

[16] Davis K 1965 The urbanization of the human population *Scientific American* **213** 40-53

[17] Jackson S 2007 *6.1. 3 System resilience: capabilities, culture and infrastructure* INCOSE International Symposium

[18] Rasmussen J 1982 Human errors. A taxonomy for describing human malfunction in industrial installations *Journal of occupational accidents* **4** 311-333

[19] Reason J 1990 The contribution of latent human failures to the breakdown of complex systems *Philosophical Transactions of the Royal Society of London. B, Biological Sciences* **327** 475-484

[20] Nagel D C, "Human error in aviation operations," in *Human factors in aviation*, ed: Elsevier, 1988, pp. 263-303.

[21] Reason J 1995 Understanding adverse events: human factors *BMJ Quality & Safety* **4** 80-89

[22] Rankin W. (2007). *MEDA Investigation Process*. Available: http://www.boeing.com/commercial/aeromagazine/articles/qtr_2_07/article_03_1.html

[23] Malik T. (2015). *Deadly SpaceShipTwo Crash Caused by Co-Pilot Error: NTSB*. Available: http://www.space.com/30073-virgin-galactic-spaceshiptwo-crash-pilot-error.html

[24] Olarte O. (2011). *HUMAN ERROR ACCOUNTS FOR 90% OF ROAD ACCIDENTS*. Available: http://www.alertdriving.com/home/fleet-alert-magazine/international/human-error-accounts-90-road-accidents

[25] National Highway Traffic Safety Administration (2009). The contribution of medical conditions to passenger vehicle crashes. *U.S. Department of Transportation*. DOT HS 811 219.

[26] Farrar C R, Worden K 2012 *Structural Health Monitoring.: A Machine Learning Perspective*John Wiley & Sons

[27] Sohn H, Farrar C R, Hemez F M, Shunk D D, Stinemates D W, Nadler B R, Czarnecki J J 2003 A review of structural health monitoring literature: 1996–2001 *Los Alamos National Laboratory, USA*

[28] Balageas D, Fritzen C-P, Güemes A 2010 *Structural health monitoring*John Wiley & Sons

[29] Carden E P, Fanning P 2004 Vibration based condition monitoring: a review *Structural Health Monitoring* **3** 355-377

[30] Diamanti K, Soutis C 2010 Structural health monitoring techniques for aircraft composite structures *Progress in Aerospace Sciences* **46** 342-352

[31] Croxford A, Wilcox P, Drinkwater B, Konstantinidis G 2007 *Strategies for guided-wave structural health monitoring* Proceedings of the Royal Society of London A: Mathematical, Physical and Engineering Sciences

[32] Raghavan A 2007 Guided-wave structural health monitoring

[33] Lee B M, Loh K J 2015 A 2D percolation-based model for characterizing the piezoresistivity of carbon nanotube-based films *Journal of Materials Science* **50** 2973-2983

[34] Soga K, Schooling J 2016 Infrastructure sensing *Interface focus* **6** 20160023

[35] Majumder M, Gangopadhyay T K, Chakraborty A K, Dasgupta K, Bhattacharya D K 2008 Fibre Bragg gratings in structural health monitoring—Present status and applications *Sensors and Actuators A: Physical* **147** 150-164

[36] Chan T H T, Yu L, Tam H Y, Ni Y Q, Liu S Y, Chung W H, Cheng L K 2006 Fiber Bragg grating sensors for structural health monitoring of Tsing Ma bridge: Background and experimental observation *Engineering Structures* **28** 648-659

[37] Zhao X, Lv X, Wang L, Zhu Y, Dong H, Chen W, Li J, Ji B, Ding Y 2015 Research of concrete residual strains monitoring based on WLI and FBG following exposure to freeze–thaw tests *Cold Regions Science and Technology* **116** 40-48

[38] López-Higuera J M, Cobo L R, Incera A Q, Cobo A 2011 Fiber optic sensors in structural health monitoring *Journal of lightwave technology* **29** 587-608

[39] Giallorenzi T G, Bucaro J A, Dandridge A, Cole J H 1986 Optical-fiber sensors challenge the competition: Resistance to corrosion and immunity to interference head the list of benefits in detecting stimuli ranging from pressure to magnetism *IEEE spectrum* **23** 44-50

[40] Lynch J P, Loh K J 2006 A summary review of wireless sensors and sensor networks for structural health monitoring *Shock and Vibration Digest* **38** 91-130

[41] Paek J, Chintalapudi K, Govindan R, Caffrey J, Masri S 2005 *A wireless sensor network for structural health monitoring: Performance and experience* The Second IEEE Workshop on Embedded Networked Sensors, 2005. EmNetS-II.

[42] Hackmann G, Guo W, Yan G, Sun Z, Lu C, Dyke S 2013 Cyber-physical codesign of distributed structural health monitoring with wireless sensor networks *IEEE Transactions on Parallel and Distributed Systems* **25** 63-72

[43] Rice J A, Spencer Jr B 2008 *Structural health monitoring sensor development for the Imote2 platform* Sensors and Smart Structures Technologies for Civil, Mechanical, and Aerospace Systems 2008

[44] Cho S, Yun C-B, Lynch J P, Zimmerman A T, Spencer Jr B F, Nagayama T 2008 Smart wireless sensor technology for structural health monitoring of civil structures *Steel Structures* **8** 267-275

[45] Tanner N A, Farrar C R, Sohn H 2002 *Structural health monitoring using wireless sensing systems with embedded processing* Nondestructive Evaluation and Health Monitoring of Aerospace Materials and Civil Infrastructures

[46] Tanner N A, Wait J R, Farrar C R, Sohn H 2003 Structural health monitoring using modular wireless sensors *Journal of Intelligent Material Systems and Structures* **14** 43-56

[47] 2015 *Wearable Electronics Sensors: For Safe and Healthy Living* S. C. Mukhopadhyay Springer International Publishing 333

[48] Lee Y-D, Chung W-Y 2009 Wireless sensor network based wearable smart shirt for ubiquitous health and activity monitoring *Sensors and Actuators B: Chemical* **140** 390-395

[49] Pandian P S, Mohanavelu K, Safeer K P, Kotresh T M, Shakunthala D T, Gopal P, Padaki V C 2008 Smart Vest: Wearable multi-parameter remote physiological monitoring system *Medical engineering & physics* **30** 466-477

[50] Sokwoo R, Boo-Ho Y, Kuowei C, Asada H H 1998 *The ring sensor: a new ambulatory wearable sensor for twenty-four hour patient monitoring* Engineering in Medicine and Biology Society. Proceedings of the 20th Annual International Conference of the IEEE

[51] Anliker U, Ward J A, Lukowicz P, Troster G, Dolveck F, Baer M, Keita F, Schenker E B, Catarsi F, Coluccini L 2004 AMON: a wearable multiparameter medical monitoring and alert system *IEEE Transactions on information technology in Biomedicine* **8** 415-427

[52] Gopalsamy C, Park S, Rajamanickam R, Jayaraman S 1999 The Wearable Motherboard™: The first generation of adaptive and responsive textile structures (ARTS) for medical applications *Virtual Reality* **4** 152-168

[53] Loh K J-H 2008 Development of Multifunctional Carbon Nanotube Nanocomposite Sensors for Structural Health Monitoring

[54] Sebastian J, Schehl N, Bouchard M, Boehle M, Li L, Lagounov A, Lafdi K 2014 Health monitoring of structural composites with embedded carbon nanotube coated glass fiber sensors *Carbon* **66** 191-200

[55] Yao S, Swetha P, Zhu Y 2018 Nanomaterial-Enabled wearable sensors for healthcare *Advanced healthcare materials* **7**

[56] Lee J, Mahendra S, Alvarez P J 2010 Nanomaterials in the construction industry: a review of their applications and environmental health and safety considerations *ACS nano* **4** 3580-3590

[57] Loh K J, Kim J, Lynch J P, Kam N W S, Kotov N A 2007 Multifunctional layer-by-layer carbon nanotube–polyelectrolyte thin films for strain and corrosion sensing *Smart Materials and Structures* **16** 429-438

[58] Nambiar S, Yeow J T 2011 Conductive polymer-based sensors for biomedical applications *Biosensors and Bioelectronics* **26** 1825-1832

[59] Janáky C, Visy C 2013 Conducting polymer-based hybrid assemblies for electrochemical sensing: a materials science perspective *Analytical and bioanalytical chemistry* **405** 3489-3511

[60] Berti F, Todros S, Lakshmi D, Whitcombe M J, Chianella I, Ferroni M, Piletsky S A, Turner A P, Marrazza G 2010 Quasi-monodimensional polyaniline nanostructures for enhanced molecularly imprinted polymer-based sensing *Biosensors and Bioelectronics* **26** 497-503

[61] Yadav B, Srivastava R, Dwivedi C, Pramanik P 2008 Moisture sensor based on ZnO nanomaterial synthesized through oxalate route *Sensors and Actuators B: Chemical* **131** 216-222

[62] Gu F, Zhang L, Yin X, Tong L 2008 Polymer single-nanowire optical sensors *Nano Letters* **8** 2757-2761

[63] Neitzert H C, Vertuccio L, Sorrentino A 2011 Epoxy/MWCNT Composite as Temperature Sensor and Electrical Heating Element *Nanotechnology, IEEE Transactions on* **10** 688-693

[64] Aragay G, Pons J, Merkoçi A 2011 Recent Trends in Macro-, Micro-, and Nanomaterial-Based Tools and Strategies for Heavy-Metal Detection *Chemical Reviews* **111** 3433-3458

[65] Gogotsi Y 2006 *Nanomaterials Handbook* Y. Gogotsi CRC press, Taylor & Francis Group, USA

[66] Yoon H, Jang J 2009 Conducting-polymer nanomaterials for high-performance sensor applications: issues and challenges *Advanced Functional Materials* **19** 1567-1576

[67] Ahuja T, Kumar D 2009 Recent progress in the development of nano-structured conducting polymers/nanocomposites for sensor applications *Sensors and Actuators B: Chemical* **136** 275-286

[68] Wang J 2005 Nanomaterial-based electrochemical biosensors *Analyst* **130** 421-426

[69] Loh K J, Chang D 2010 Zinc oxide nanoparticle-polymeric thin films for dynamic strain sensing *Journal of Materials Science* **46** 228-237

[70] Gullapalli H, Vemuru V S, Kumar A, Botello-Mendez A, Vajtai R, Terrones M, Nagarajaiah S, Ajayan P M 2010 Flexible piezoelectric ZnO–paper nanocomposite strain sensor *small* **6** 1641-1646

[71] Son D, Lee J, Qiao S, Ghaffari R, Kim J, Lee J E, Song C, Kim S J, Lee D J, Jun S W 2014 Multifunctional wearable devices for diagnosis and therapy of movement disorders *Nature nanotechnology* **9** 397-404

[72] Pang C, Lee C, Suh K Y 2013 Recent advances in flexible sensors for wearable and implantable devices *Journal of Applied Polymer Science* **130** 1429-1441

[73] Hammock M L, Chortos A, Tee B C K, Tok J B H, Bao Z 2013 25th Anniversary Article: The Evolution of Electronic Skin (E-Skin): A Brief History, Design Considerations, and Recent Progress *Advanced materials* **25** 5997-6038

[74] Yamada T, Hayamizu Y, Yamamoto Y, Yomogida Y, Izadi-Najafabadi A, Futaba D N, Hata K 2011 A stretchable carbon nanotube strain sensor for human-motion detection *Nature nanotechnology* **6** 296-301

[75] Wang Y, Wang L, Yang T, Li X, Zang X, Zhu M, Wang K, Wu D, Zhu H 2014 Wearable and highly sensitive graphene strain sensors for human motion monitoring *Advanced Functional Materials* **24** 4666-4670

[76] Amjadi M, Pichitpajongkit A, Lee S, Ryu S, Park I 2014 Highly stretchable and sensitive strain sensor based on silver nanowire–elastomer nanocomposite *ACS nano* **8** 5154-5163

[77] Gong S, Schwalb W, Wang Y, Chen Y, Tang Y, Si J, Shirinzadeh B, Cheng W 2014 A wearable and highly sensitive pressure sensor with ultrathin gold nanowires *Nature communications* **5**

[78] Pang C, Lee G-Y, Kim T-i, Kim S M, Kim H N, Ahn S-H, Suh K-Y 2012 A flexible and highly sensitive strain-gauge sensor using reversible interlocking of nanofibres *Nature materials* **11** 795-801

[79] Kwak M K, Jeong H E, Suh K Y 2011 Rational Design and Enhanced Biocompatibility of a Dry Adhesive Medical Skin Patch *Advanced materials* **23** 3949-3953

[80] Lipomi D J, Vosgueritchian M, Tee B C K, Hellstrom S L, Lee J A, Fox C H, Bao Z 2011 Skin-like pressure and strain sensors based on transparent elastic films of carbon nanotubes *Nat Nano* **6** 788-792

[81] Fan F-R, Lin L, Zhu G, Wu W, Zhang R, Wang Z L 2012 Transparent triboelectric nanogenerators and self-powered pressure sensors based on micropatterned plastic films *Nano Letters* **12** 3109-3114

[82] Wang K, Meng Q, Zhang Y, Wei Z, Miao M 2013 High-Performance Two-Ply Yarn Supercapacitors Based on Carbon Nanotubes and Polyaniline Nanowire Arrays *Advanced materials* **25** 1494-1498

[83] Tee B C K, Wang C, Allen R, Bao Z 2012 An electrically and mechanically self-healing composite with pressure- and flexion-sensitive properties for electronic skin applications *Nat Nano* **7** 825-832

[84] Salvetat J-P, Briggs G A D, Bonard J-M, Bacsa R R, Kulik A J, Stöckli T, Burnham N A, Forró L 1999 Elastic and shear moduli of single-walled carbon nanotube ropes *Physical review letters* **82** 944-947

[85] Yu M-F, Files B S, Arepalli S, Ruoff R S 2000 Tensile loading of ropes of single wall carbon nanotubes and their mechanical properties *Physical review letters* **84** 5552-5555

[86] Walters D, Ericson L, Casavant M, Liu J, Colbert D, Smith K, Smalley R 1999 Elastic strain of freely suspended single-wall carbon nanotube ropes *Applied Physics Letters* **74** 3803-3805

[87] Tombler T W, Zhou C, Alexseyev L, Kong J, Dai H, Liu L, Jayanthi C, Tang M, Wu S-Y 2000 Reversible electromechanical characteristics of carbon nanotubes under local-probe manipulation *Nature* **405** 769-772

[88] Cao J, Wang Q, Dai H 2003 Electromechanical properties of metallic, quasimetallic, and semiconducting carbon nanotubes under stretching *Physical review letters* **90** 157601

[89] Grow R J, Wang Q, Cao J, Wang D, Dai H 2005 Piezoresistance of carbon nanotubes on deformable thin-film membranes *Applied Physics Letters* **86** 093104-093106

[90] Ma P-C, Siddiqui N A, Marom G, Kim J-K 2010 Dispersion and functionalization of carbon nanotubes for polymer-based nanocomposites: a review *Composites Part A: Applied Science and Manufacturing* **41** 1345-1367

[91] Jiang P, McFarland M J 2004 Large-scale fabrication of wafer-size colloidal crystals, macroporous polymers and nanocomposites by spin-coating *Journal of the American Chemical Society* **126** 13778-13786

[92] Ahmed F, Kumar S, Arshi N, Anwar M, Su-Yeon L, Kil G-S, Park D-W, Koo B H, Lee C G 2011 Preparation and characterizations of polyaniline (PANI)/ZnO nanocomposites film using solution casting method *Thin Solid Films* **519** 8375-8378

[93] Manna K, Wang L, Loh K J, Chiang W H 2019 Printed Strain Sensors Using Graphene Nanosheets Prepared by Water-Assisted Liquid Phase Exfoliation *Advanced Materials Interfaces* **6** 1900034

[94] Dharap P, Li Z, Nagarajaiah S, Barrera E 2004 Nanotube film based on single-wall carbon nanotubes for strain sensing *Nanotechnology* **15** 379

[95] Ko F, Gogotsi Y, Ali A, Naguib N, Ye H, Yang G, Li C, Willis P 2003 Electrospinning of continuous carbon nanotube-filled nanofiber yarns *Advanced materials* **15** 1161-1165

[96] Sen R, Zhao B, Perea D, Itkis M E, Hu H, Love J, Bekyarova E, Haddon R C 2004 Preparation of Single-Walled Carbon Nanotube Reinforced Polystyrene and Polyurethane Nanofibers and Membranes by Electrospinning *Nano Letters* **4** 459-464

[97] Renedo O D, Alonso-Lomillo M, Martínez M A 2007 Recent developments in the field of screen-printed electrodes and their related applications *Talanta* **73** 202-219

[98] Zhang Y, Sun X, Pan L, Li H, Sun Z, Sun C, Tay B K 2009 Carbon nanotube–ZnO nanocomposite electrodes for supercapacitors *Solid State Ionics* **180** 1525-1528

[99] Shin K Y, Hong J Y, Jang J 2011 Micropatterning of Graphene Sheets by Inkjet Printing and Its Wideband Dipole-Antenna Application *Advanced materials* **23** 2113-2118

[100] Kong D, Le L T, Li Y, Zunino J L, Lee W 2012 Temperature-dependent electrical properties of graphene inkjet-printed on flexible materials *Langmuir* **28** 13467-13472

[101] Li J, Ye F, Vaziri S, Muhammed M, Lemme M C, Östling M 2013 Efficient inkjet printing of graphene *Advanced materials* **25** 3985-3992

[102] Finn D J, Lotya M, Cunningham G, Smith R J, McCloskey D, Donegan J F, Coleman J N 2014 Inkjet deposition of liquid-exfoliated graphene and MoS 2 nanosheets for printed device applications *Journal of Materials Chemistry C* **2** 925-932

[103] Loyola B R, Saponara V, Loh K J, Briggs T M, O'Bryan G, Skinner J L 2013 Spatial sensing using electrical impedance tomography *Sensors Journal, IEEE* **13** 2357-2367

[104] Loyola B R, Briggs T M, Arronche L, Loh K J, La Saponara V, O'Bryan G, Skinner J L 2013 Detection of spatially distributed damage in fiber-reinforced polymer composites *Structural Health Monitoring* **12** 225-239

[105] Mortensen L P, Ryu D H, Zhao Y J, Loh K J 2013 Rapid Assembly of Multifunctional Thin Film Sensors for Wind Turbine Blade Monitoring *Key Engineering Materials* **569** 515-522

[106] Wang L, Loh K J 2016 Spray-coated carbon nanotube-latex strain sensors *Science Letters Journal* **5**

[107] Shin M K, Oh J, Lima M, Kozlov M E, Kim S J, Baughman R H 2010 Elastomeric conductive composites based on carbon nanotube forests *Advanced materials* **22** 2663-2667

[108] Thostenson E T, Ren Z, Chou T-W 2001 Advances in the science and technology of carbon nanotubes and their composites: a review *Composites Science and Technology* **61** 1899-1912

[109] Gojny F H, Wichmann M, Köpke U, Fiedler B, Schulte K 2004 Carbon nanotube-reinforced epoxy-composites: enhanced stiffness and fracture toughness at low nanotube content *Composites Science and Technology* **64** 2363-2371

[110] Malik S, Rosner H, Hennrich F, Bottcher A, Kappes M M, Beck T, Auhorn M 2004 Failure mechanism of free standing single-walled carbon nanotube thin films under tensile load *Physical Chemistry Chemical Physics* **6** 3540-3544

[111] Song X, Liu S, Gan Z, Lv Q, Cao H, Yan H 2009 Controllable fabrication of carbon nanotube-polymer hybrid thin film for strain sensing *Microelectronic Engineering* **86** 2330-2333

[112] Kim S W, Kim T, Kim Y S, Choi H S, Lim H J, Yang S J, Park C R 2012 Surface modifications for the effective dispersion of carbon nanotubes in solvents and polymers *Carbon* **50** 3-33

[113] Tian H, Shu Y, Cui Y-L, Mi W-T, Yang Y, Xie D, Ren T-L 2014 Scalable fabrication of high-performance and flexible graphene strain sensors *Nanoscale* **6** 699-705

[114] Westervelt R M 2008 Graphene Nanoelectronics *Science* **320** 324-325

[115] Wei W, Qu X 2012 Extraordinary physical properties of functionalized graphene *small* **8** 2138-2151

[116] Lee Y-H, Zhang X-Q, Zhang W, Chang M-T, Lin C-T, Chang K-D, Yu Y-C, Wang J T-W, Chang C-S, Li L-J, Lin T-W 2012 Synthesis of Large-Area MoS2 Atomic Layers with Chemical Vapor Deposition *Advanced Materials* **24** 2320-2325

[117] Luo B, Liu S, Zhi L 2012 Chemical Approaches toward Graphene-Based Nanomaterials and their Applications in Energy-Related Areas *Small* **8** 630-646

[118] Liu C-J, Tai S-Y, Chou S-W, Yu Y-C, Chang K-D, Wang S, Chien F S-S, Lin J-Y, Lin T-W 2012 Facile synthesis of MoS2/graphene nanocomposite with high catalytic activity toward triiodide reduction in dye-sensitized solar cells *Journal of Materials Chemistry* **22** 21057-21064

[119] Park J J, Hyun W J, Mun S C, Park Y T, Park O O 2015 Highly stretchable and wearable graphene strain sensors with controllable sensitivity for human motion monitoring *ACS Applied Materials & Interfaces* **7** 6317-6324

[120] Long W, Kenneth J L, Wei-Hung C, Kausik M 2018 Micro-patterned graphene-based sensing skins for human physiological monitoring *Nanotechnology* **29** 105503

[121] Ranjbartoreh A R, Wang B, Shen X, Wang G 2011 Advanced mechanical properties of graphene paper *Journal of Applied Physics* **109** 014306

[122] Novoselov K S, Jiang D, Schedin F, Booth T J, Khotkevich V V, Morozov S V, Geim A K 2005 Two-dimensional atomic crystals *Proceedings of the National Academy of Sciences of the United States of America* **102** 10451-10453

[123] Reina A, Jia X, Ho J, Nezich D, Son H, Bulovic V, Dresselhaus M S, Kong J 2009 Large Area, Few-Layer Graphene Films on Arbitrary Substrates by Chemical Vapor Deposition *Nano Letters* **9** 30-35

[124] Li D, Kaner R B 2008 Graphene-Based Materials *Science* **320** 1170-1171

[125] Hernandez Y 2008 High-yield production of graphene by liquid-phase exfoliation of graphite *Nat. Nanotech.* **3** 563–568

[126] Hu K, Tolentino L S, Kulkarni D D, Ye C, Kumar S, Tsukruk V V 2013 Written-in Conductive Patterns on Robust Graphene Oxide Biopaper by Electrochemical Microstamping *Angewandte Chemie International Edition* **52** 13784-13788

[127] Niu L, Coleman J N, Zhang H, Shin H, Chhowalla M, Zheng Z 2016 Production of Two-Dimensional Nanomaterials via Liquid-Based Direct Exfoliation *Small* **12** 272-293

[128] Manna K, Hsieh C-Y, Lo S-C, Li Y-S, Huang H-N, Chiang W-H 2016 Graphene and graphene-analogue nanosheets produced by efficient water-assisted liquid exfoliation of layered materials *Carbon* **105** 551-555

[129] Coleman J N 2013 Liquid Exfoliation of Defect-Free Graphene *Accounts of Chemical Research* **46** 14-22

[130] Halim U, Zheng C R, Chen Y, Lin Z, Jiang S, Cheng R, Huang Y, Duan X 2013 A rational design of cosolvent exfoliation of layered materials by directly probing liquid–solid interaction *Nat Commun* **4** 2213

[131] Lee C, Yan H, Brus L E, Heinz T F, Hone J, Ryu S 2010 Anomalous lattice vibrations of single-and few-layer MoS2 *ACS nano* **4** 2695-2700

[132] Eckmann A, Felten A, Mishchenko A, Britnell L, Krupke R, Novoselov K S, Casiraghi C 2012 Probing the nature of defects in graphene by Raman spectroscopy *Nano Letters* **12** 3925-3930

[133] Manna K, Huang H-N, Li W-T, Ho Y-H, Chiang W-H 2016 Toward Understanding the Efficient Exfoliation of Layered Materials by Water-Assisted Cosolvent Liquid-Phase Exfoliation *Chemistry of materials* **28** 7586-7593

[134] Yu T, Ni Z, Du C, You Y, Wang Y, Shen Z 2008 Raman Mapping Investigation of Graphene on Transparent Flexible Substrate: The Strain Effect *The Journal of Physical Chemistry C* **112** 12602-12605

[135] Larson B J, Gillmor S D, Lagally M G 2004 Controlled deposition of picoliter amounts of fluid using an ultrasonically driven micropipette *Review of Scientific Instruments* **75** 832-836

[136] Bracamonte M, Lacconi G, Urreta S, Foa Torres L 2014 On the nature of defects in liquid-phase exfoliated graphene *The Journal of Physical Chemistry C* **118** 15455-15459

[137] Hernandez Y, Nicolosi V, Lotya M, Blighe F M, Sun Z, De S, McGovern I, Holland B, Byrne M, Gun'Ko Y K 2008 High-yield production of graphene by liquid-phase exfoliation of graphite *Nature nanotechnology* **3** 563-568

[138] Smith A, Niklaus F, Paussa A, Vaziri S, Fischer A C, Sterner M, Forsberg F, Delin A, Esseni D, Palestri P 2013 Electromechanical piezoresistive sensing in suspended graphene membranes *Nano Letters* **13** 3237-3242

[139] Zhu S-E, Krishna Ghatkesar M, Zhang C, Janssen G 2013 Graphene based piezoresistive pressure sensor *Applied Physics Letters* **102** 161904

[140] Lee B M, Loh K J, Yang Y-S 2017 Carbon nanotube thin film strain sensor models assembled using nano- and micro-scale imaging *Computational Mechanics* **60** 39-49

[141] Wang L, Loh K J, Brely L, Bosia F, Pugno N M 2016 An experimental and numerical study on the mechanical properties of carbon nanotube-latex thin films *Journal of the European Ceramic Society* **36** 2255-2262

[142] Yeo W H, Kim Y S, Lee J, Ameen A, Shi L, Li M, Wang S, Ma R, Jin S H, Kang Z 2013 Multifunctional epidermal electronics printed directly onto the skin *Advanced materials* **25** 2773-2778

[143] Kim J, Lee M, Shim H J, Ghaffari R, Cho H R, Son D, Jung Y H, Soh M, Choi C, Jung S 2014 Stretchable silicon nanoribbon electronics for skin prosthesis *Nature communications* **5** 5747

[144] Choi M K, Park I, Kim D C, Joh E, Park O K, Kim J, Kim M, Choi C, Yang J, Cho K W 2015 Thermally controlled, patterned graphene transfer printing for transparent and wearable electronic/optoelectronic system *Advanced Functional Materials* **25** 7109-7118

[145] Amjadi M, Kyung K U, Park I, Sitti M 2016 Stretchable, Skin-Mountable, and Wearable Strain Sensors and Their Potential Applications: A Review *Advanced Functional Materials* **26** 1678-1698

[146] Bae S-H, Lee Y, Sharma B K, Lee H-J, Kim J-H, Ahn J-H 2013 Graphene-based transparent strain sensor *Carbon* **51** 236-242

[147] Li X, Zhang R, Yu W, Wang K, Wei J, Wu D, Cao A, Li Z, Cheng Y, Zheng Q 2012 Stretchable and highly sensitive graphene-on-polymer strain sensors *Scientific reports* **2** 870

[148] Wu C T 1962 Transverse sensitivity of bonded strain gages *Experimental Mechanics* **2** 338-344

[149] Machin K E, Hassan Y E 1976 Transverse-sensitivity errors in strain-gage measurement *Experimental Mechanics* **16** 38-40

[150] Gelinck G H, Huitema H E A, Van Veenendaal E, Cantatore E, Schrijnemakers L, Van Der Putten J B, Geuns T C, Beenhakkers M, Giesbers J B, Huisman B-H 2004 Flexible active-matrix displays and shift registers based on solution-processed organic transistors *Nature materials* **3** 106

[151] Forrest S R 2004 The path to ubiquitous and low-cost organic electronic appliances on plastic *Nature* **428** 911

[152] Hammock M L, Chortos A, Tee B C-K, Tok J B-H, Bao Z 2013 25th Anniversary Article: The Evolution of Electronic Skin (E-Skin): A Brief History, Design Considerations, and Recent Progress *Advanced materials* **25** 5997-6038

[153] Mohammad Haniff M A S, Muhammad Hafiz S, Wahid K A A, Endut Z, Wah Lee H, Bien D C S, Abdul Azid I, Abdullah M Z, Ming Huang N, Abdul Rahman S 2015 Piezoresistive effects in controllable defective HFTCVD graphene-based flexible pressure sensor *Scientific reports* **5** 14751

[154] Zhu C, Chortos A, Wang Y, Pfattner R, Lei T, Hinckley A C, Pochorovski I, Yan X, To J W F, Oh J Y, Tok J B H, Bao Z, Murmann B 2018 Stretchable temperature-sensing circuits with strain suppression based on carbon nanotube transistors *Nature Electronics* **1** 183-190

[155] Wu S, Ladani R B, Zhang J, Ghorbani K, Zhang X, Mouritz A P, Kinloch A J, Wang C H 2016 Strain sensors with adjustable sensitivity by tailoring the microstructure of graphene aerogel/PDMS nanocomposites *ACS Applied Materials & Interfaces* **8** 24853-24861

[156] Aguilar Ventura I, Zhou J, Lubineau G 2015 Drastic modification of the piezoresistive behavior of polymer nanocomposites by using conductive polymer coatings *Composites Science and Technology* **117** 342-350

[157] Zhao J, Wang G, Yang R, Lu X, Cheng M, He C, Xie G, Meng J, Shi D, Zhang G 2015 Tunable piezoresistivity of nanographene films for strain sensing *ACS nano* **9** 1622-1629

[158] Yao S, Zhu Y 2015 Nanomaterial-enabled stretchable conductors: strategies, materials and devices *Advanced materials* **27** 1480-1511

[159] Tang Y, Yin J 2017 Design of cut unit geometry in hierarchical kirigami-based auxetic metamaterials for high stretchability and compressibility *Extreme Mechanics Letters* **12** 77-85

[160] Barlian A A, Park W-T, Mallon J R, Rastegar A J, Pruitt B L 2009 Semiconductor piezoresistance for microsystems *Proceedings of the IEEE* **97** 513-552

[161] Kuo H-H, Shapiro M C, Riggs S C, Fisher I R 2013 Measurement of the elastoresistivity coefficients of the underdoped iron arsenide Ba (Fe 0.975 Co 0.025) 2 As 2 *Physical Review B* **88** 085113

[162] Johns G K, Howell L L, Jensen B D, McLain T W 2008 A Model for Predicting the Piezoresistive Effect in Microflexures Experiencing Bending and Tension Loads *Journal of Microelectromechanical Systems* **17** 226-235

[163] Bjorn S. (2017). *How to Generate Randomized Inhomogeneous Material Data*. Available: https://www.comsol.com/blogs/how-to-generate-randomized-inhomogeneous-material-data/

[164] Bjorn S. (2017). *How to Generate Random Surfaces in COMSOL Multiphysics®*. Available: https://www.comsol.com/blogs/how-to-generate-random-surfaces-in-comsol-multiphysics/

[165] Heinz-Otto P, Dietmar S, Eds., *The Science of Fractal Images*. Springer-Verlag New York, Inc., 1988, p.^pp. Pages.

[166] Pechprasarn T, Pongnumkul S 2013 *Estimation of respiratory rate from smartphone's acceleration data* 2013 10th International Conference on Electrical Engineering/Electronics, Computer, Telecommunications and Information Technology

[167] E. M G 1969 *Schaum's Outline of Continuum Mechanics*McGraw-Hill

[168] Gong S, Lai D T, Wang Y, Yap L W, Si K J, Shi Q, Jason N N, Sridhar T, Uddin H, Cheng W 2015 Tattoolike polyaniline microparticle-doped gold nanowire patches as highly durable wearable sensors *ACS Applied Materials & Interfaces* **7** 19700-19708

[169] Lee J, Kim S, Lee J, Yang D, Park B C, Ryu S, Park I 2014 A stretchable strain sensor based on a metal nanoparticle thin film for human motion detection *Nanoscale* **6** 11932-11939

[170] Majerus S, Gill-Thwaites H, Andrews K, Laureys S 2005 Behavioral evaluation of consciousness in severe brain damage *Progress in brain research* **150** 397-413

[171] León-Carrión J, Eeckhout P v, Domínguez-Morales M d R 2002 Review of subject: the locked-in syndrome: a syndrome looking for a therapy *Brain injury* **16** 555-569

[172] Richard I, Pereon Y, Guiheneu P, Nogues B 1995 Persistence of distal motor control in the locked in syndrome. Review of 11 patients I Richard!, Y Pereon2, P Guiheneu2, B Nogues2, B Perrouin-Verbe1 and JF Mathe1 *Paraplegia* **33** 640-646

[173] Avolio A P, Butlin M, Walsh A 2009 Arterial blood pressure measurement and pulse wave analysis—their role in enhancing cardiovascular assessment *Physiological Measurement* **31** R1

[174] Elgendi M 2012 On the analysis of fingertip photoplethysmogram signals *Current cardiology reviews* **8** 14-25

[175] Fan Z, Zhang G, Liao S 2009 *Clinical analysis for cardiovascular disease by calculating Stiffness Index, Cardiac Output from pulse wave* Electrical and Computer Engineering, 2009. CCECE'09. Canadian Conference on

[176] Moon S-H, Moon J-C, Heo D-H, Lim Y-H, Choi J-H, Kim S-Y, Kim K-S, Joo S-J 2015 Increased pulse wave velocity and augmentation index after isometric handgrip exercise in patients with coronary artery disease *Clinical hypertension* **21** 5

[177] Ansari F 2005 *Sensing issues in civil structural health monitoring*Springer

[178] Caffrey J, Govindan R, Johnson E, Krishnamachari B, Masri S, Sukhatme G, Chintalapudi K, Dantu K, Rangwala S, Sridharan A 2004 *Networked sensing for structural health monitoring* Proceedings of the 4th International Workshop on Structural Control

[179] Wang L, Gupta S, Loh K J, Koo H S 2016 *Nanocomposite Fabric Sensors for Monitoring Inflatable and Deployable Space Structures* ASME 2016 Conference on Smart Materials, Adaptive Structures and Intelligent Systems

[180] Holder D S 2004 *Electrical impedance tomography: methods, history and applications*CRC Press

[181] Gehre M, Kluth T, Lipponen A, Jin B, Seppänen A, Kaipio J P, Maass P 2012 Sparsity reconstruction in electrical impedance tomography: an experimental evaluation *Journal of Computational and Applied Mathematics* **236** 2126-2136

[182] Liliana B 2002 Electrical impedance tomography *Inverse Problems* **18** R99

[183] Hyvönen N 2004 Complete electrode model of electrical impedance tomography: Approximation properties and characterization of inclusions *SIAM Journal on Applied Mathematics* **64** 902-931

[184] Cheney M, Isaacson D, Newell J C 1999 Electrical impedance tomography *SIAM review* **41** 85-101

[185] Vauhkonen P J, Vauhkonen M, Savolainen T, Kaipio J P 1999 Three-dimensional electrical impedance tomography based on the complete electrode model *IEEE Transactions on Biomedical Engineering* **46** 1150-1160

[186] Wang J, Ma J, Han B, Li Q 2012 Split Bregman iterative algorithm for sparse reconstruction of electrical impedance tomography *Signal Processing* **92** 2952-2961

[187] Vauhkonen M, Lionheart W R, Heikkinen L M, Vauhkonen P J, Kaipio J P 2001 A MATLAB package for the EIDORS project to reconstruct two-dimensional EIT images *Physiological Measurement* **22** 107

[188] Tehrani J N, Jin C, McEwan A, van Schaik A 2010 *A comparison between compressed sensing algorithms in electrical impedance tomography* 2010 Annual International Conference of the IEEE Engineering in Medicine and Biology

[189] Candès E J, Tao T 2009 The power of convex relaxation: Near-optimal matrix completion *arXiv preprint arXiv:0903.1476*

[190] Candes E J, Romberg J K, Tao T 2006 Stable signal recovery from incomplete and inaccurate measurements *Communications on Pure and Applied Mathematics: A Journal Issued by the Courant Institute of Mathematical Sciences* **59** 1207-1223

[191] Baraniuk R G 2007 Compressive sensing *IEEE signal processing magazine* **24**

[192] Donoho D L 2006 Compressed sensing *IEEE Transactions on information theory* **52** 1289-1306

[193] Eldar Y C, Kutyniok G 2012 *Compressed sensing: theory and applications*Cambridge university press

[194] Bioucas-Dias J M, Figueiredo M A T 2007 A New TwIST: Two-Step Iterative Shrinkage/Thresholding Algorithms for Image Restoration *IEEE Transactions on Image processing* **16** 2992-3004

[195] Graham B, Adler A 2006 Objective selection of hyperparameter for EIT *Physiological Measurement* **27** S65

[196] Adler A, Guardo R 1996 Electrical impedance tomography: regularized imaging and contrast detection *IEEE transactions on medical imaging* **15** 170-179

[197] Colombo I S, Main I, Forde M 2003 Assessing damage of reinforced concrete beam using "b-value" analysis of acoustic emission signals *Journal of materials in civil engineering* **15** 280-286

[198] Hidalgo P A, Ledezma C A, Jordan R M 2002 Seismic behavior of squat reinforced concrete shear walls *Earthquake Spectra* **18** 287-308

[199] Su R, Wong S 2007 Seismic behaviour of slender reinforced concrete shear walls under high axial load ratio *Engineering Structures* **29** 1957-1965

[200] Staszewski W, Tomlinson G, Boller C, Tomlinson G 2004 *Health monitoring of aerospace structures*Wiley Online Library

[201] Ohtsu M, Uchida M, Okamoto T, Yuyama S 2002 Damage assessment of reinforced concrete beams qualified by acoustic emission *Structural Journal* **99** 411-417

[202] Villalba S, Casas J R 2013 Application of optical fiber distributed sensing to health monitoring of concrete structures *Mechanical Systems and Signal Processing* **39** 441-451

[203] Yan S, Sun W, Song G, Gu H, Huo L-S, Liu B, Zhang Y-G 2009 Health monitoring of reinforced concrete shear walls using smart aggregates *Smart Materials and Structures* **18** 047001

[204] Song G, Gu H, Mo Y-L 2008 Smart aggregates: multi-functional sensors for concrete structures—a tutorial and a review *Smart Materials and Structures* **17** 033001

[205] Saafi M 2009 Wireless and embedded carbon nanotube networks for damage detection in concrete structures *Nanotechnology* **20** 395502

[206] Konsta-Gdoutos M S, Aza C A 2014 Self sensing carbon nanotube (CNT) and nanofiber (CNF) cementitious composites for real time damage assessment in smart structures *Cement and Concrete Composites* **53** 162-169

[207] Materazzi A L, Ubertini F, D'Alessandro A 2013 Carbon nanotube cement-based transducers for dynamic sensing of strain *Cement and Concrete Composites* **37** 2-11

[208] Faraone G, Hutchinson T C, Piccinin R, Silva J 2019 Cyclic Lateral Load Response of Full-Scale Flexure-Dominated Shear Wall *ACI Structural Journal*

[209] Bouten D B C, Oomens D C C 2005 Pressure Ulcer Research

[210] Dillingham T R, Pezzin L E, MacKenzie E J 2002 Limb amputation and limb deficiency: epidemiology and recent trends in the United States *Southern medical journal* **95** 875-884

[211] Feinglass J, Brown J L, LoSasso A, Sohn M-W, Manheim L M, Shah S J, Pearce W H 1999 Rates of lower-extremity amputation and arterial reconstruction in the United States, 1979 to 1996 *American Journal of Public Health* **89** 1222-1227

[212] Pirouzi G, Abu Osman N A, Eshraghi A, Ali S, Gholizadeh H, Wan Abas W A B 2014 Review of the Socket Design and Interface Pressure Measurement for Transtibial Prosthesis *The Scientific World Journal* **2014** 9

[213] Al-Fakih E A, Abu Osman N A, Mahmad Adikan F R 2016 Techniques for Interface Stress Measurements within Prosthetic Sockets of Transtibial Amputees: A Review of the Past 50 Years of Research *Sensors* **16** 1119

[214] Jia X, Zhang M, Lee W C 2004 Load transfer mechanics between trans-tibial prosthetic socket and residual limb—dynamic effects *Journal of biomechanics* **37** 1371-1377

[215] Ali S, Abu Osman N A, Eshraghi A, Gholizadeh H, Abd razak N A b, Wan Abas W A B B 2013 Interface pressure in transtibial socket during ascent and descent on stairs and its effect on patient satisfaction *Clinical Biomechanics* **28** 994-999

[216] Lyder C H 2003 Pressure ulcer prevention and management *Jama* **289** 223-226

[217] Daniel R K, Priest D L, Wheatley D C 1981 Etiologic factors in pressure sores: an experimental model *Archives of physical medicine and rehabilitation* **62** 492-498

[218] Scales J, "Pathogenesis of pressure sores," in *Pressure Sores-Clinical Practice and Scientific Approach*, ed: Springer, 1990, pp. 15-26.

[219] Polliack A, Craig D, Sieh R, Landsberger S, McNeal D 2002 Laboratory and clinical tests of a prototype pressure sensor for clinical assessment of prosthetic socket fit *Prosthetics and orthotics international* **26** 23-34

[220] Sanders J E 1995 Interface mechanics in external prosthetics: review of interface stress measurement techniques *Medical and Biological Engineering and Computing* **33** 509-516

[221] Holloway G A, Daly C H, Kennedy D, Chimoskey J 1976 Effects of external pressure loading on human skin blood flow measured by 133Xe clearance *Journal of Applied Physiology* **40** 597-600

[222] Dyson M, Moodley S, Verjee L, Verling W, Weinman J, Wilson P 2003 Wound healing assessment using 20 MHz ultrasound and photography *Skin Research and Technology* **9** 116-121